The Millimeter Transient Sky: Detecting and characterizing astrophysical transients in data from the Atacama Cosmology Telescope

by

Emily Biermann

B. Sc., Stony Brook University, 2019

M. Sc., University of Pittsburgh, 2022

Submitted to the Graduate Faculty of

the Dietrich School of Arts and Sciences in partial fulfillment

of the requirements for the degree of

Doctor of Philosophy

University of Pittsburgh

2024

UNIVERSITY OF PITTSBURGH

DIETRICH SCHOOL OF ARTS AND SCIENCES

This dissertation was presented

by

Emily Biermann

It was defended on

July 8th 2024

and approved by

Arthur Kosowsky, Dept. of Physics and Astronomy, University of Pittsburgh

Carlos Badenes, Dept. of Physics and Astronomy, University of Pittsburgh

John Hillier, Dept. of Physics and Astronomy, University of Pittsburgh

Adam Hincks, Dept. of Astronomy and Astrophysics/St. Michael's College, University of Toronto

Donna Naples, Dept. of Physics and Astronomy, University of Pittsburgh

The Millimeter Transient Sky: Detecting and characterizing astrophysical transients in data from the Atacama Cosmology Telescope

Emily Biermann, PhD

University of Pittsburgh, 2024

The heavens have a flair for the dramatic. Stars are born then die, galaxies churn, and the very fabric of the universe rapidly expands. Few objects remain steady for our telescopes. Instead, the transient sky dominates. "Transients" are a broad category of astrophysical events defined as anything that displays a sudden change in brightness. As is often the case in astrophysics, we can learn about different aspects of these events by studying the different kinds of light, or wavelengths, they emit. Although transient phenomena in optical, in-fared, and radio wavelengths are relatively well-studied, millimeter wavelengths present a gap in our knowledge. These wavelengths are particularly challenging because millimeter-sensitive instrumentation is expensive and complex. Unlike the radio regime, millimeter waves are greatly affected by the atmosphere. Large-scale cosmic microwave background, or CMB, surveys were once reserved for studying the static imprint of our early universe. However, these surveys now have the sensitivity required to join the hunt for transients, allowing us to fill the gap in time domain astrophysics.

Wide-field CMB surveys are uniquely suited to searching for transients because they observe large areas of the sky at increasingly lower noise levels. These telescopes are expected to see a variety of events occurring outside our galaxy, such as stars exploding or being ripped apart by black holes, as well as events within the Milky Way such as flaring stars. Transients are already being detected in CMB surveys like The Atacama Cosmology Telescope, known as ACT ([62] and [47]), and The South Pole Telescope ([97] and [30]). Future surveys, such as The Simons Observatory Large Aperture Telescope, or SO-LAT [105], and CMB-S4 [2], are expected to detect at least an order of magnitude more millimeter transient events than current surveys [24]. To get the most out of this science, we must start exploring this parameter space and building the means to detect millimeter transients in real-time. This dissertation provides the necessary background knowledge of this subject, explores my

work on astrophysical transient detection using data from the Atacama Cosmology Telescope (ACT), and comments on the future of millimeter transient astronomy.

Table of Contents

Preface . . . xvii

1.0 Introduction . . . 1

1.1 The Millimeter Transient Sky . . . 1

1.2 Synchrotron Emission . . . 3

1.2.1 Average Power . . . 3

1.2.2 Spectrum and Spectral Index . . . 4

1.3 Astrophysical Transients . . . 6

1.3.1 Gamma Ray Bursts . . . 6

1.3.2 Classical Novae . . . 8

1.3.3 Stellar Flares . . . 9

1.3.4 Fast Radio Bursts . . . 12

1.4 The Atacama Cosmology Telescope . . . 14

1.4.1 Data Taking . . . 14

1.4.2 Maximum Likelihood Map Making . . . 16

1.4.3 ACT as a Transient Detector . . . 17

2.0 Systematic Transient Search of 3 Day Maps . . . 19

2.1 Introduction . . . 19

2.2 Data . . . 19

2.3 Methodology . . . 21

2.3.1 Initial Detection and Spurious Candidate Cuts . . . 21

2.3.2 Candidate Verification . . . 23

2.4 Results . . . 25

2.4.1 Transient Surface Density . . . 25

2.4.2 Characterization . . . 28

2.4.3 Counterparts . . . 32

2.5 Discussion and Conclusions . . . 33

3.0 Systematic Transient Search of Single Observation Maps 41
3.1 Introduction 41
3.2 Data 42
3.3 Methodology 42
3.3.1 Detection Pipeline 42
3.3.2 Candidate Verification 46
3.4 Results 48
3.4.1 Light Curves 51
3.5 Discussion and Conclusions 53
3.5.1 Stellar Flares 53
3.5.2 Other Transients 55
4.0 Conclusions 66
Bibliography 69

List of Tables

1 The band and observation time for each detector array in AdvACT. In 2020, pa7 replaced pa6 in the third optics tube, but pa7's data are not considered in this paper. 14

2 This table summarizes the three geometric data cuts applied to each 3-day map after the requirement that a candidate appear in at least two frequency or array combinations is applied. The first column quotes the number of candidates remaining after that cut, the second gives the fraction of all candidates that do not pass these cuts, and the last column gives the fraction of the total number of pixels masked by each cut. Note that these cuts are done in tandem and are independent from each other. The neighbor cut removes candidates with neighbors in the same map within 20 arcminutes, the zero inverse variance contour (ZiVC) cut masks candidates within five pixels of zero inverse variance contours, and the edge cut masks candidates within five pixels of the edge. 24

3 Transient surface density for each frequency split between day and night data. These values represent the surface density for the highest sensitivity required to detect one of our transients. We split this measurement between frequencies and day and night data since the sensitivity thresholds of these maps are very different. The average transient surface density across all frequencies and arrays is $7.06 \times 10^{-6}[\mathrm{deg}]^{-2}$ 29

4 Eight events associated with asteroids. 30

5 Properties of the transient events. The candidates are listed in the order of the detection time (or the detection of the first event for the repeating candidates). Three single detections labeled as "N" are the redetections of the transients published in [62]. It is difficult to fit for rise and fall time using light curves due to uneven scanning cadence. Instead, we examine if the scan right before and after the scans with the peak flux density has a $> 5\sigma$ detection, and calculate the time interval in between the scans. The rise time of Event 4a is left empty because the time gap between the peak scan and the scan right before is longer than 50 days. Spectral index is evaluated as described in text, using array-wise flux density values, except for candidate 13. This transient event completed the rise and fall process within the time the sky took to drift across the array. We therefore evaluate the spectral index using flux values taken by only one quarter of detectors in each array, to capture the peak flux. 36

6 Possible counterparts for each transient event from the SIMBAD database. If known, the spectral type is given next to the object type. The chance of a false association is calculated using the density of Gaia sources with the same magnitude or brighter of the counterpart. If the Gaia object is not found in the SIMBAD database, then the Gaia identification number is listed. All separations are calculated using the Gaia coordinates. This table also includes counterparts associated with the three previously published ACT transients from [62]. When two stars from the same system are resolved, as is the case with events 7 and 12, we quote the average separation weighted by one minus the chance association and we list the lowest of the two chance associations. 39

7 We mask sources in the depth-1 maps which are greater than one sigma in each map. We use this flux limit rather than masking all sources so that we will detect transients from known sources which are nominally not detected in a depth-1 map. In this table we give the typical detection level and the flux limit of masked sources for each frequency. 44

8 The percent of pixels of all depth-1 maps cut by each type of mask. The Galaxy mask masks the Galactic plane, the edge cut masks pixels within 10 pixels of the edge. The source cut masks all pixels within 5 arcminute of any source above our flux limit in the ACT source catalog. The planets mask cuts pixels within 50 arcminutes of Venus. Mars, Jupiter, Saturn, Uranus, or Neptune. The blazar cut masks sources within 30 arcminutes of the bright blazar 3C 454.3 which is not in the ACT source catalog. We also provide the percentage of pixels cut by all the masks combined. Note that there may be some overlap between masks. 44

9 Summary of candidate cuts. We quote the total number of candidates detected in all the depth-1 maps, the number of candidates that are cut at each step, and the number of remaining candidates. Init. and Rem. refer to the initial and remaining candidates respectively. MF, CM, AS, PS, and MA refer to the number of candidates cut by the matched filter, array crossmatching, asteroid crossmatching, post point source cutting, and manual cutting respectively.The post point source cut removes constant sources which are flagged as transients due to pointing errors within the map. 50

10 This table summarizes the results of testing the transient pipeline by analyzing sources with an S/N greater than ten. We present the number of such sources found in all the depth-1 maps (N Sources), the percentage that are cut by applying a matched filter and requiring a S/N greater than 5 (MF), and by crossmatching across arrays (CM). We also give the combined number of detections cut by either step (Total). 50

11 Catalog of the transients. Each different number occurs at a different position. Transients marked with a letter have multiple events at the same position in the sky. Each event's position error is evaluated as the variance of the coordinates observed by different array-frequency combinations. 52

12 Properties for all transients. We provide the peak and mean fluxes of each frequency. If a source is detected by more than one array in a given frequency band, we cite a weighted average. The peak time is defined as the time of the maximum flux in the f090 frequency band. The mean flux is calculated from the weighted average flux over all observations. The rise and fall times are evaluated from the candidates' light curves and subarray light curves. The "$\gg$" sign of the candidate's rise and fall time means that we do not see a minute-wise flux density change within the peak scan but there is a >5 day time gap between the peak scan and the adjacent scan. The spectral index α is evaluated by fitting a power law $S_\nu \propto \nu^\alpha$ of frequency ν using flux density data S_ν taken by pa4 and pa5 because these two array observed the candidates at the same time. 56

13 Transient counterparts from the SIMBAD Database. For repeating events, we take the lower position error to calculate the chance of a random association. For each independent transient position we cite the most likely counterpart from SIMBAD. In the case of binary objects, we cite the object with the lower chance of random association with the transient candidate. The separations are calculated using Gaia positions for all but event 26 where we use the position from SIMBAD. For all events except Event 7 we calculate a density of Gaia stars with the magnitude of the candidate or brighter to determine the chance of a random association (p-value). For Event 7 this is calculated using a 6 degree radius due to a low density of stars with this magnitude or brighter. We also include the spectral type, if known, in the 'type' column. 60

List of Figures

1 Figure 1a from [40] showing the t_{90} distribution of 222 BATSE GRBs. The solid line shows the raw data and the dotted lines are error-convolved histograms. 7

2 Schematic of the evolution and light curve of a classical novae. Image taken from Figure 1 of [19]. 9

3 Relationship between the fractional X-ray luminosity, a magnetic field tracer, and Rossby number. The data presented in this figure is from a sample of 824 solar and late-type stars [100]. Image taken from [41]. . . 11

4 Figure 1 from [72] showing the cumulative number of FRB detections. These detections skyrocket after CHIME begins observations in 2018 and CHIME's FRB catalog dominates the sample. 13

5 An example of a partial TOD from one detector taken on a good observing night at 148 GHz. Atmospheric brightness causes a slow drift in intensity. Image taken from [23]. 15

6 An example of a transient detected in sequential depth-1 maps. These maps are 0.5 deg^2 cutouts of the depth-1 signal to noise ratio maps. They are filtered on small scales to boost signals with the shape of the beam. The three rows are example depth-1 maps from each frequency band (90 GHz, 150 GHz, and 220 GHz). The x-axis is the time, in days, from the first observation of the flare. From left to right, we show the same location in each subsequent map. No source is seen before the flare, but then a transient appears before fading again. The transient appears as a red dot in the center of the map. 18

7 Process of the initial detection, with each plot showing a 0.3 deg by 0.3 deg map. The first step is to make a mask (middle) on S/N map (left) selecting pixels that have $S/N > 5$. The mask is then applied to the flux map (right), and the candidate position, shown as the red cross mark, is evaluated as the center of mass weighted by the flux values within the selected pixels. 21

8 ***Left:*** A histogram of the distance to each detection's nearest neighbor with a binsize of 5 arcminutes. The peak close to zero indicates there are clusters of spurious detections in many of the maps so we cut any candidate with a nearest neighbor of 20 arcminutes or less. ***Center:*** A histogram of each candidate's distance from the nearest zero inverse variance contour, defined to be an inverse variance of less than $1.5 \times 10^{-5} K$, with a bin size of 3 pixels. There is a large peak of candidates near zero inverse variance contours which drops after 3 pixels. We mask out to 5 pixels, cutting 74% of all sources. ***Right:*** A histogram of each candidate's distance from the map edge in pixel units with a bin size of 3 pixels. As expected, there is an excess number of candidates near the edge of the map as the map edges are noisy and so appear variable when sampled every three days. At a mask size of 5 pixels, we cut off the peak of candidates near the edge. 22

9 10 arcminutes x 10 arcminutes 3-day thumbnail maps for each transient. The upper row is the intensity map with ± 5000 μK color range. The bottom row is the S/N map after applying a matched filter, with ± 5 color range. Due to the conjugate gradient iteration used to solve the maximum-likelihood map-making equation only being run for 10 steps, these maps are effectively mildly highpass filtered. The affected scales have negligible weight in the matched filter. Events 2, 9, 10, 13 at the bottom of the table are the four events that are difficult to determine if they are real transients. 26

10 Surface density of transients for each frequency split between day and night data. The surface density is found by counting the number of transients we are able to detect given the sensitivity level divided by the map area at that sensitivity or lower. 27

11 ***Left:*** The three transient events consistent with Hygiea observations. ***Right:*** The five transient events consistent with Davida observations. All of the plotted positions and observation times are consistent with the asteroids' paths. The position errors are on the order of 0.1 arcminutes. 31

12 Light curves for 18 detected transient events on day time scales from the peak. Each frequency is denoted by a different color. We see that in most cases the peak is correlated with all frequencies. 37

13 High-resolution light curves for transient events on minute time scales. Events 1, 2, 5, 6, 7, 8, 9, 10, 13, 14 and 15 show strong signal variation within a space of four minutes. 38

14 Combined ACT data from 2007–2019 overlayed with the transient positions. Images from DSS at each location, indicated by a in the center of each image, are also shown with a one arcminute contour plotted for scale. The majority of the transient events have bright stellar counterparts seen in the optical. 40

15 Example S/N maps before and after renormalization, plotted in linear color scale from -5 to +5. There are false signals showing as high-S/N patches on the original matched filtered maps due to imprecise noise modelling. We cut the maps into tiles and apply a renomalization factor so that the mean of each tile's S/N square is corrected to unity. 43

16 Example of a 20'x20' map of an artifact that passes all cuts and is manually cut from the analysis. This is a signal to noise plot made from a portion of a depth-1 map from array pa4 of a frequency of 150 GHz. For comparison, the dashed circle on the upper right corner shows the 150 GHz beam size. If these sources are real transients, this would mean two point sources separated by several arcminutes on the sky have a large rise in flux at the same time. The much more likely scenario is these are artifacts and not real transients. 47

17 Event (RA: 9.063 ± 6, DEC: -41.870 ± 6) detected by our transient pipeline but cut from the analysis since it is clearly a variable source rather than a transient event. This figure shows the light curve of this event. The grey vertical lines indicate where this source is detected by the pipeline. Note the y-axis is zoomed in for clarity and there are many flux upper limits from f220 which are above the plots y-axis limit. . . . 49

18 Continued on the next page 57

18 Continued on the next page 58

18 Three color, 10 arcminute by 10 arcminute images of candidates from depth-1 maps about one month before and after detection. Red, blue, and green correspond to f090, f150, and f220 respectively. Note the thumbnails are chronological but have inconsistent spacing in time. These plots are included for illustration rather than quantitative analysis. . . . 59

19 Flux light curves from the depth-1 maps. The flux is measured by detecting a source with a S/N of at least three and within at least two arcminutes of the candidate's position. The data are binned in 0.5 day bins for clarity. Points with errorbars indicate a detection of $SNR > 3$ and points without errorbars show upper flux limits for each frequency. The time of detection from the pipeline is marked by the grey vertical lines. Note the light curves for events 22 and 26 are shown in Figure 21 because they are not associated with stellar flares. 61

20 Subarray light curves from forced photometry measurements. Each array is separated into four sections and we evaluate the flux per section as the transient event drift across the whole arrays. 62

21 Depth-1 lightcurves for non-stellar-flare events. The x-axis measures the time since the first detection by ACT. The detections from the transient pipeline are marked with grey vertical lines. We present lightcurves from three frequency bands, 90, 150, and 220 GHz shown in blue, yellow, and green respectively. The data are binned into 0.5 day bins for clarity. Points with errorbars indicate a detection of S/N$>$ 3 and points without errorbars show upper flux limits for each frequency. **Left**: Event 22 is coincident with the classical nova YZ Ret. It is detected by ACT about sixty days after initial detection in X-Ray and optical bands [87]. **Right:** Event 26 is associated with the LINER-type AGN 2MASX J19495127-363523. This AGN appears to brighten above baseline variability. . . . 63

22 Histogram of the galactic latitude of stellar flares at unique locations. This histogram hints at an over-density close the the galactic plane, however the number of flares is too small to make a broad generalization. . 64

23 **Left:** Characteristic luminosity in each frequency band for stellar flare events. The luminosity is calculated using the distance to the flare's counterpart listed in Table 13. We include other millimeter flares for comparison from the Atacama Large Millimeter/submillimeter Array (ALMA: [52, 50]), the Owens Valley Millimeter Array (OVMA: [12]), the Berkely-Illinois-Maryland Association (BIMA: [10]), the Nobeyama 45 m telescope (EFF: [92]), the Plateau de Bure Interferometer (PDBI: [57]), and the JCMT Transient Survey (SCUBA2: [53]). **Right:** Histogram of spectral indices for stellar flares from this paper (ACT) and [89] (SPT). We also give the combined distribution. The means of the ACT, SPT, and combined distributions are $\alpha = -0.19, 0.18$, and 0.092 respectively. 65

Preface

Like anything worth doing, I could not have done this alone. There are so many people who supported me through my graduate school experience and I will cherish the memories we made along the way. First, I would like to thank my Advisor, Arthur Kosowsky. He has been an excellent and honest career consultant, research collaborator, and friend.

Thank you to my committee who went above and beyond our yearly meetings to ensure my success. I was blessed to have such a supportive community within the Astronomy department as a whole. Every member, from faculty to graduate student strived to create a friendly and productive environment. I am so grateful for all your hard work.

The ACT and SO community were both instrumental to my success. Again, I was extremely lucky to work with such kind and brilliant people. Thank you especially to Yaqiong Li, my academic partner in crime.

I met many incredible friends over the past five years. We had a little more fun than we should and I wouldn't have it any other way. A special thanks to Amy and Melanie who supported me almost literally every day of my PhD.

Above all, thank you to my family. My sisters, Haley and Natalie, were always only a phone call away and I had to joy of watching them both marry their husbands during my graduate career. My parents encouraged me to follow my passion since I told them I wanted to be an astronomer when I was eight years old. Without their support, I would not have had the courage to leave home and pursue my dream.

Lastly, thank you to Josh who showed me that not all who wander are lost. Here's to our next adventure.

1.0 Introduction

This introduction serves as a review of transient astronomy, particularly in millimeter wavelengths, as well as cosmic microwave background surveys. The topics presented here are not original works but provide the reader a comprehensive background of original research in subsequent chapters. In the first section, I provide context for millimeter transient studies, presenting past work done on the subject. Next, I discuss synchrotron emission, a key mechanism for many millimeter transients. Then, I focus on specific types of astrophysical transients we detect in millimeter bands. Lastly, I discuss the Atacama Cosmology Telescope, the main source of data in the subsequent chapters.

1.1 The Millimeter Transient Sky

Multiwavelength studies of transient events are vital to understanding their underlying physical mechanisms. Transients are a broad class of astrophysical events that are defined as point sources which are nominally not detectable but temporarily produce enough emission to become visible. A true transient will occur either one time only or in an unpredictable rather than variable pattern. Until recently, millimeter transient detections were limited to targeted follow-up observations. This gap is quickly being filled by harnessing the cosmic microwave background (CMB) surveys to perform blind transient searches in millimeter wavelengths [97, 62, 30, 47, 89]. Observations in the millimeter and radio allow us to probe non-thermal emission from shocks and jets [15, 16] or magnetic recombination of nearby magnetically active stars [51]. Eftekhari et al. 2022 [24] predicted event rates of extragalactic synchrotron transients emitting in the millimeter for CMB surveys such as CMB-S4 [1], Simons Observatory [4], ACT [25, 91], and the South Pole Telescope (SPT) [13]. In particular, they found CMB surveys will serve as an unbiased probe of the prevalence of reverse shocks (RS) within long gamma ray bursts (LGRBs), a phenomenon that occurs when two shock waves collide after the burst [24].

The list of high energy extragalactic transient detections within millimeter wavebands is rapidly growing. Kuno et al. 2004 [43] observed the afterglow of GRB 030329 in radio and millimeter frequencies, Laskar et al. 2019 [45] observed polarized reverse shock emission in GRB 190114C using ALMA observations at 97.5 GHz, and MUSTANG-2 detected the decaying emission of the tidal disruption event (TDE) AT2022cmc [102]. High-sensitivity wide-field CMB surveys are expected to add to this list. Eftekhari et al. 2022 [24] predict ACT could have observed two to ten reverse shock emission events from GRBs and that Simons Observatory may observe dozens. The millimeter band is particularly suited to reverse shock observation as the emission peaks only a couple hours after the trigger [11, 83]. They also predict a small chance of detecting tidal disruption events that have also been observed in targeted millimeter wavelength campaigns [103]. Additionally, we may see emission from events similar to the extragalactic transient AT2018cow [75], an unprecedented millimeter transient [36] that may have been a supernova or tidal disruption event [77, 71, 55].

With a zoo of transients to search for, wide-field millimeter surveys designed for mapping the CMB are increasingly being used for transient detection. Whitehorn et al. 2016 [97], using data from SPT, published the first blind transient search of CMB survey data and reported an event broadly consistent with a GRB afterglow with a peak flux of 16.5 ± 2.4mJy at 150 GHz but with a low statistical significance. Guns et al. 2021 [30] used a single year of SPT-3G (an upgraded version of SPT) data to find 13 stellar flares and 2 events consistent with flares from active galactic nuclei. Recently, Tandoi et al. 2024 [89] found 111 stellar flares from 66 stars over 4 years and 1500 square degrees of observations also using data from SPT-3G. ACT published three previous papers relating to transient phenomena. Using 3-day coadded maps made for a Planet 9 search ACT serendipitously discovered three bright transients consistent with flares from magnetically active stars [62]. Those detections inspired a systematic transient search of the 3-day maps, yielding 17 transient detections, including the serendipitous detections, mostly consistent with stellar flares. This analysis is discussed in detail in Chapter 2. Lastly, a targeted search of ACT data published upper flux limits on known tidal disruption events, supernovae and gamma ray bursts [34].

1.2 Synchrotron Emission

Gyrosynchrotron and synchrotron emission all occur from particles radiating when accelerated by a magnetic field, B and is often the driver of millimeter astrophysical transients. The following derivations are a summary of Chapter 6 of [79] and Chapter 5 of [20].

1.2.1 Average Power

Gyrosynchrotron emission is the name given to particles at nonrelativistic speeds ($v \ll c$) and synchrotron emission occurs for ultra-relativistic particles with high kinetic energies ($KE \gg m_e c^2$). For the non-relativistic case, the orbital frequency is exactly equal to the gyro frequency,

$$\omega_G = \frac{qB}{mc}, \tag{1}$$

where q is the charge of the particle, B is the magnitude of the magnetic field, m is the particle mass, and c is the speed of light. In the case of electrons, q is the charge of the electron, e, and m is the mass of the electron, m_e. For ultra-relativistic electrons, this expression is velocity dependent;

$$\omega_B = \frac{eB}{(\gamma m_e)\, c} = \frac{\omega_G}{\gamma} \tag{2}$$

where,

$$\gamma \equiv \left(1 - \beta^2\right)^{-1/2} \tag{3}$$

and,

$$\beta \equiv v/c. \tag{4}$$

The power of synchrotron radiation from a single electron is derived from Larmor's equation,

$$P = \frac{2}{3}\frac{e^2 \mathbf{a^2}}{c^3}, \tag{5}$$

where a is the electron's acceleration. This equation tells us particles radiate when accelerated and that power is a relativistic invariant quantity. In the case of synchrotron radiation, the particles experience acceleration perpendicular to the magnetic field in the rest frame,

$a_\perp = \omega_B v_\perp = \omega_B \sin\alpha$. The pitch angle, α is defined as the angle between the particle's velocity and the magnetic field. Plugging in equation 1 for ω_B gives,

$$a_\perp = \frac{eBv\sin\alpha}{\gamma m_e c}. \tag{6}$$

In the observer's frame, $a'_\perp = \gamma^2 a_\perp$. Putting this all together we find the power radiated by one electron to be,

$$P = 2\sigma_T \beta^2 \gamma^2 c U_B \sin^2\alpha, \tag{7}$$

where,

$$\sigma_T \equiv \frac{8\pi}{3}\left(\frac{e^2}{m_e c^2}\right)^2, \tag{8}$$

is the Thomson cross section of an electron,

$$U_B = \frac{B^2}{8\pi} \tag{9}$$

is the magnetic energy density. Averaging over all pitch angles, we find the average synchrotron power per electron is

$$\langle P\rangle = \frac{4}{3}\sigma_T \beta^2 \gamma^2 c U_B. \tag{10}$$

In the case of gyrosynchrotron radiation, $\gamma^2 = 1$.

1.2.2 Spectrum and Spectral Index

In the non-relativistic regime, the observer sees pulses at a frequency approximately equal to ω_B. However, for relativistic synchrotron radiation, the radiation beams along the direction of motion resulting in a pulse time difference, Δt, much shorter than $2\pi/\omega_B$ and a spectrum much broader than $\omega_B/2\pi$, as the spectrum cuts off at frequencies around $1/\Delta t$. Using geometric principles and approximating $1-\beta \approx (1/2)\gamma^2$ for $\gamma \gg 1$ one can find

$$\Delta t \approx \frac{1}{\gamma^3 \omega_B \sin\alpha}. \tag{11}$$

We expect the spectrum to cut off at the critical frequency, defined as

$$v_c = \frac{3}{4\pi}\gamma^3 \omega_B \sin\alpha. \tag{12}$$

See [67] for the full derivation.

Next, we want to find the spectral index of synchrotron emission, which tells us how the energy radiated changes with frequency,

$$\alpha \equiv \frac{\mathrm{d}\log P_\nu}{\mathrm{d}\log \nu}, \tag{13}$$

where P_ν is the radiative flux density. α can also be written in terms of the source function, S_ν,

$$\alpha = \frac{\ln S_\nu}{d\nu}, \tag{14}$$

which is directly proportional to the emission coefficient, j_ν. The emission coefficient (see Chapter 2 of [20]) is given by,

$$j_\nu d\nu = -\frac{dE}{dt} n(E) dE. \tag{15}$$

The energy distribution of synchrotron sources often follow a power law. Assuming an optically thin source with a power law distribution of electrons we can write,

$$n(E)dE \propto E^{-\delta} dE. \tag{16}$$

Given Equation 2, the energy of a synchrotron source is,

$$E = \gamma m_e c^2 \equiv \left(\frac{\nu}{\nu_G}\right)^{1/2} m_e c^2. \tag{17}$$

Next, we assume each electron radiates all of its average power (Equation 10) close to the critical frequency to find

$$dE \approx \frac{m_e c^2 \nu^{-1/2}}{2\nu_G^{1/2}} d\nu, \tag{18}$$

where $\nu_G = qB/2\pi mc$.

Now, we can calculate the emission coefficient (Equation 15),

$$j_\nu d\nu \propto B^{(\delta+1)/2} \nu^{(1-\delta)/2}. \tag{19}$$

This leads to the spectral index which is only dependent on δ,

$$\alpha = \frac{d\ln S}{d\ln \nu} = \frac{1-\delta}{2}. \tag{20}$$

1.3 Astrophysical Transients

This section serves as a broad introduction to astrophysical transients. This thesis presents a large portion of millimeter transient observations made to-date by harnessing the large data volume of CMB surveys to perform blind transient surveys. Much of this work is informed by predictions in [24] of transient event rates for CMB surveys. In that analysis, the authors predict CMB surveys will observe synchrotron emission from several types of extragalactic transient events such as gamma ray bursts (GRBs). The events explored here either have been found or are expected to be observed by CMB surveys. I pay special attention to GRBs, classical novae, and stellar flares, as these events will be explored in greater detail in subsequent chapters. I also provide a brief overview of fast radio bursts. Although we do not expect to detect this type of transient in the analyses describes in Chapters 2 and 3, they are a remarkable and mysterious class of radio transients which showcase the importance of searching unexplored regimes for transient phenomena.

1.3.1 Gamma Ray Bursts

A gamma ray burst is a transient event which produces high energy gamma rays from powerful jets and then radiates in all frequency bands in what is called the "afterglow". These events exist in two categories, short bursts, which last for 2 seconds or less, and long bursts, which can last anywhere from a few seconds to many hours [40]. Short bursts are theorized to occur from binary compact object mergers and produce hard (more energetic) photons [7]. Long bursts emerge from the collapse of a massive star and produce soft (less energetic) photons [98]. The origins of the long bursts are confirmed by coincident supernovae observations. The exact categorization and differences of short and long GRBs is a current topic of research. By convention, the time of the total burst duration is measured using the value t_{90}, or the time it takes to observe 90% of the total background subtracted counts. An analysis of the Burst and Transient Source Experiment (BATSE) catalog revealed a bimodal distribution of this quantity giving rise to the long and short classification of GRBs [40]. Figure 1 showcases these results.

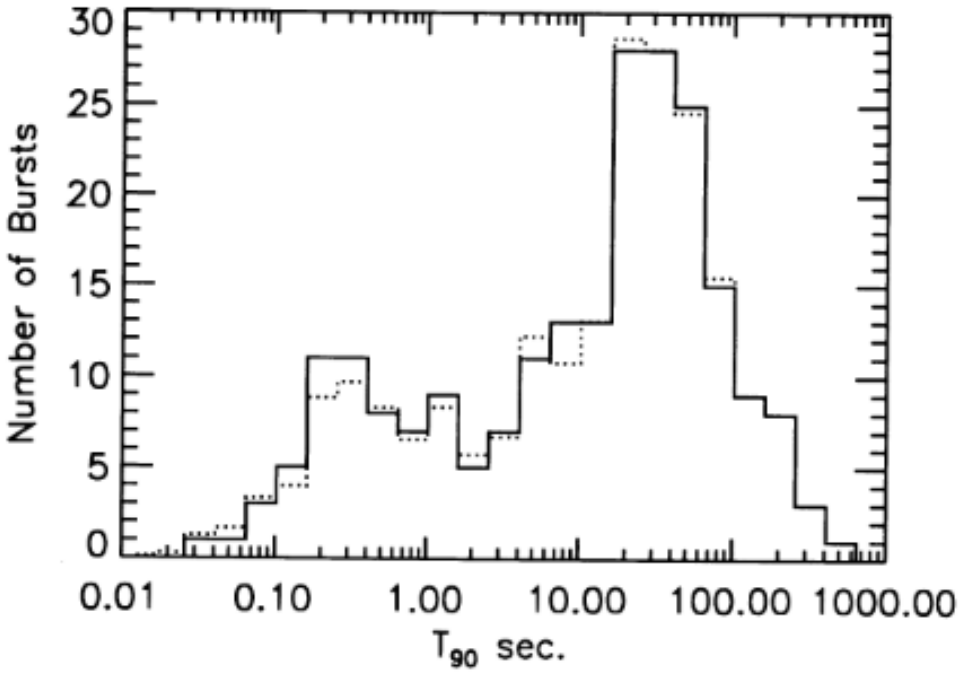

Figure 1: Figure 1a from [40] showing the t_{90} distribution of 222 BATSE GRBs. The solid line shows the raw data and the dotted lines are error-convolved histograms.

It is largely accepted that both long and short GRBs contain a black hole (BH) as a central engine. However, there is much debate on the exact mechanisms behind these events. GRBs are often described by the Fireball Model [73]. The model approximates GRBs as a pure radiation fireball where most of the initial energy from the BH formation is converted to photons There are two main phases of emission; the prompt emission from the formation of jets, and the afterglow from the interaction of these jets with the surrounding circumburst medium (CBM). The prompt emission occurs from the dissapation of kinetic energy of a relativistic flow and produces the GRB's namesake gamma rays. The kinetic energy is dissipated by both internal and external shocks. GRBs are characterized by the bulk Lorentz, Γ_0, of the outflow. The afterglow occurs from the jets slowing down due to external shock interactions causing emission from X-Ray to radio wavelengths.

The spectra of GRBs are largely dependent on the opening angle of the jet, θ. At early stages, the jets are narrowly beamed ($\Gamma^{-1} < \theta$), but as the ejecta lose energy, the beam

becomes larger and more of the emission is observable [49]. As the ejectum continues to decelerate, eventually the entire surface becomes observable, corresponding to a jet break in the light curve in all wavelengths [68, 82]. The jet-break occurs when the opening angle of the jet widens such that the jet is indistinguishable from the afterglow emission. This presents as a break in the power-law spectrum of the GRB. Observers off-axis from the jet do not observe prompt emission or the jet break. Such events are difficult to observe but have recently been seen in millimeter wavelengths, solidifying current understanding of GRB jets [46, 54].

The jets contain two shock fronts. These shock fronts can collide to create a reverse shock, dividing the jet into four sections; the ambient medium, the shocked ambient medium which the forward shock has passed through, the shocked shell which the reverse shock has passed through, and the unshocked shell [73]. Although the exact fraction of GRBs that exhibit reverse shocks is unknown, this may be a ubiquitous feature. CMB surveys are expected to observe many transients from reverse shock emission and will provide an unbiased statistical probe of this phenomenon [24]. See Section 2.1 for a more detailed discussion on millimeter emission from GRBs. For a comprehensive review of GRBs, see [49].

1.3.2 Classical Novae

A classical nova occurs when an accreting white dwarf (WD) in a binary system with a main sequence star undergoes thermonuclear runaway (TNR)[28]. Thermonuclear runaway occurs when gravitational pressure causes electron degeneracy. Once this happens, the material does not expand even as temperature rises due to compression. The result is a rapid temperature increase causing the accretion envelope to expand and become ejected [88]. Typically, the white dwarf accretes hydrogen, although in rare cases it may accrete helium. This process is similar to a supernovae explosion but only the outer layer is ejected. After the explosion, the white dwarf will begin accreting material again and the process will repeat itself. Novae that have more than one recorded eruption are known as recurrent novae [19].

Figure 2 from [19] illustrates the typical evolution and corresponding light curve of a classical nova. Before the outburst, the white dwarf accretes material until it experiences

TNR, emitting thermal radiation which peaks in the X-ray band. This is called the X-ray flash phase which was recently observed for the first time from the nova YZ Ret [44, 87]. Next, the shell expands, corresponding to a rapidly rising optical lightcurve with a slow decay driven by thermal emission [70]. As the shell expands and the optical depth increases, thermal radio emission becomes observable from nuclear burning on the surface of the white dwarf. This is known as the "supersoft X-ray phase" [39]. In Section 3.5 I discuss millimeter observations of the nova YZ Ret from this phase. In some cases, there may be hard X-ray and radio synchrotron emission from shocks similar to those discussed in Section 1.3.1 [19]. For a full review of classical novae, see [19].

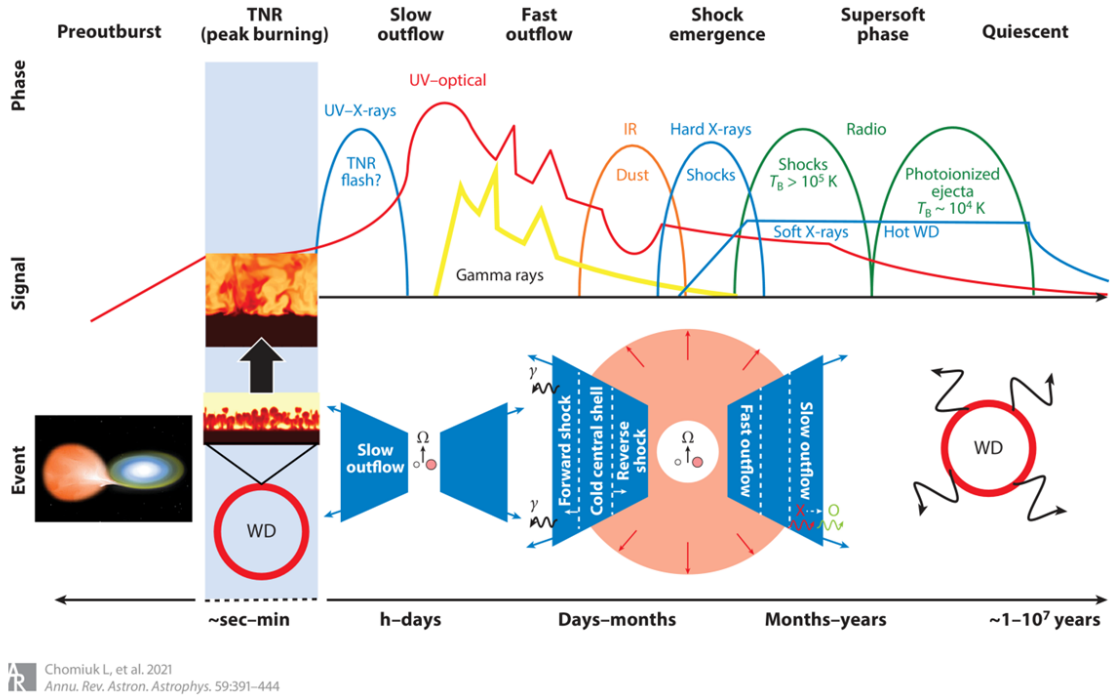

Figure 2: Schematic of the evolution and light curve of a classical novae. Image taken from Figure 1 of [19].

1.3.3 Stellar Flares

Stellar flares occur from magnetic fields reconnecting and heating the atmosphere. These events result in emission across the electromagnetic spectrum in the form of both thermal

and nonthermal radiation and last anywhere from seconds to days. The thermal emission is seen in optical and near-ultraviolet (NUV) frequencies from the lower atmosphere. The nonthermal gyrosynchrotron emission emerges from particles accelerated by the magnetic fields and emits in radio and microwave frequencies [41]. Ion collisions also cause radio emission via bremsstrahlung radiation [22].

Typically, stellar flares occur in stars with magnetically active coronas and with rapid rotation. The Rossby number is often used as a tracer of stellar rotation and is defined as

$$R_0 = \frac{P_{rot}}{\tau_c}, \tag{21}$$

where P_{rot} is the rotational period of the star and τ_c is the convective turnover time [64]. Used in conjunction with the fractional X-ray luminosity, $R_x = L_x/L_{bol}$ where L_x is the star's x-ray luminosity and L_{bol} is the star's bolometric luminosity, a tracer for magnetic activity, we can find a relationship between magnetic activity and rotational period. Stars with low Rossby numbers ($R_0 < 0.1$) are typically quiescent and are said to be in the "saturated regime" [64, 74]. These stars have a maximum X-ray luminosity, $L_x/L_{bol} \approx 10^{-3}$ [93, 94]. Stars outside of this regime follow a power-law, as illustrated in Figure 3, which is taken from Figure 4 in [41] who adapted the figure from [100].

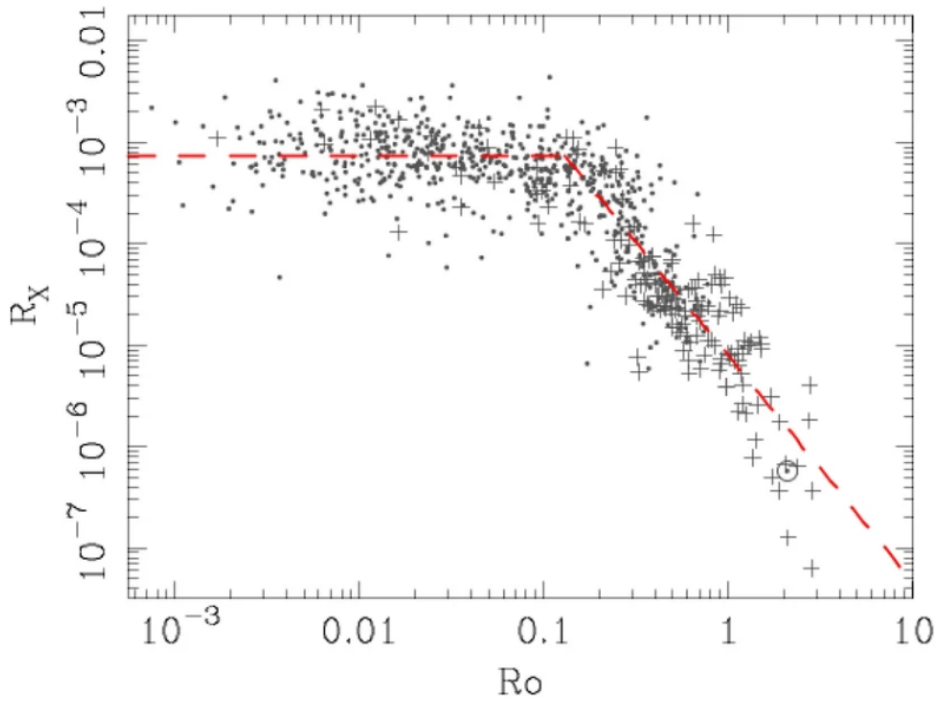

Figure 3: Relationship between the fractional X-ray luminosity, a magnetic field tracer, and Rossby number. The data presented in this figure is from a sample of 824 solar and late-type stars [100]. Image taken from [41].

There are several types of magnetically active stars which exhibit flaring behavior. Below, I outline three common categories of flaring stars discussed in Chapter 3. For a full review of stellar flares, see [41].

M Dwarfs: M dwarfs are the most common stars in our galaxy, making up 70% of galactic stars by number [9]. They are cool, small in size, and faint main sequence stars. Early types (M0 – M5) contain a radiative core while later types are fully convective [100] and are therefore highly magnetically active. These stars are known to host rocky planets within the habitable zone, making them prime candidates for exoplanet studies [84].

RS CVn Variables: RS CVn variables are tidally locked binary systems. They consist of an early-type main sequence star and a cool G or K giant. Although these stars on their own would not have heightened flare rates, the tidal locking causes rapid rotation, causing the system to flare [41]. These systems produce extremely energetic flares in X-ray and UV

wavelengths and can be up to five orders of magnitude more luminous than solar flares [42]. RS CVn binaries are also known to flare in millimeter and radio wavelengths due to optically thick gyrosynchrotron emission [12].

BY Draconis: BY Draconis, or BY Dra variables are formally defined as stars with magnetically active starspots causing causing periodic dips in their optical light curves [81, 41]. However, this term usually describes low-mass main sequence binary systems that are detached but orbit closely together. The stars often have synchronous or near synchronous rotation [41].

1.3.4 Fast Radio Bursts

An archival data search from observations taken by the Parkes Telescope in Australia revealed the first fast radio burst (FRB) discovery [48]. The burst was incredibly bright at 30 mJy but lasted less than five milliseconds. The search for these strange and powerful events unexpectedly took off with the completion of CHIME, a radio experiment located in Canada. The main science goal of CHIME is to map hydrogen in the Universe to understand cosmological structure. However, when CHIME saw first light it proved to also be an unprecedented FRB detector. Since CHIME began observations in 2018, it observed over 600 FRBs and continues to detect FRBs at an increasing rate [72], as shown in Figure 4.

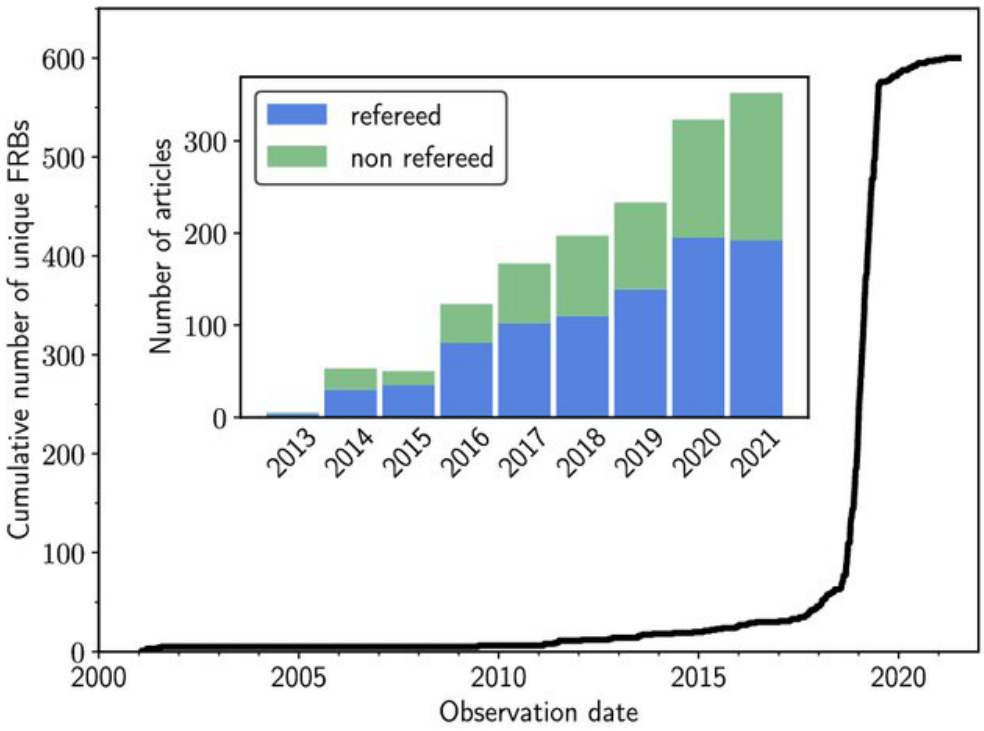

Figure 4: Figure 1 from [72] showing the cumulative number of FRB detections. These detections skyrocket after CHIME begins observations in 2018 and CHIME's FRB catalog dominates the sample.

The origin of FRBs are unknown, but redshift measurements of host galaxy candidates as well as interglactic medium models indicate they have cosmological origins [90]. One FRB is associated with a magnetar [17]. There are most likely several populations of FRBs because they showcase a range of properties such as repeaters vs non-repeaters. No matter the origin, it is clear FRBs may be used as cosmological probes. Since these events occur at extragalactic redshfits and are evenly distributed on the sky, the dispersion measure, or the measure of the time delay between different frequency detections, of each event can be used to create a map of matter in the Universe [76]. For a brief but useful review of FRBs, see [63].

1.4 The Atacama Cosmology Telescope

Most of the data presented in this dissertation was taken by The Atacama Cosmology Telescope (ACT) [25, 91]. ACT was a 6-meter off-axis Gregorian telescope located in the Chilean Desert. The telescope is primarily used for studies of the cosmic microwave background. However, this dissertation is centered on its use as an astrophysical transient detector.

1.4.1 Data Taking

This dissertation makes use of data taken from 2017–2022 by the third generation of ACT, AdvACT [33], the third generation ACT instrument. It simultaneously housed three optics tubes with a total field of view (FOV) spanning $\sim$1.5°[91], each containing a set of lenses, low-pass filters, and a single AdvACT detector array [37, 18]. The ACT dataset considered here covers the three bandpasses f090 (77–112 GHz), f150 (124–172 GHz) and f220 (182–277 GHz) using the three dichroic polarization-sensitive transition edge sensor (TES) bolometer arrays PA4 (f150+f220), PA5 (f090+f150) and PA6 (f090+f150). The beams' full-width-half-maximum (FWHM) are approximately 2.0 arcminutes, 1.4 arcminutes and 1 arcminute respectively for band f090, f150 and f220 but these numbers vary slightly between optics tubes. Details of the arrays are described in Table 1.

array	frequency band	observation time
pa4	f220 & f150	2016 Aug – 2022 Oct
pa5	f150 & f090	2017 Apr – 2022 Oct
pa6	f150 & f090	2017 Apr – 2020 Jan
pa7	f040 & f030	2020 Feb – 2022 Oct

Table 1: The band and observation time for each detector array in AdvACT. In 2020, pa7 replaced pa6 in the third optics tube, but pa7's data are not considered in this paper.

During observations, the telescope scanned the sky in azimuth at a fixed elevation at a

scan speed of ∼1.5 deg per second. When the sky was rising, it took ∼6 minutes for a point on the sky to be gradually swept across by the detectors in PA4 and PA5. Then, after ∼3 minutes this process would repeat for the detectors in PA6. This order was reversed when the sky was setting. The bolometer signals, i.e. measured optical power fluctuations, were stored in time-ordered data (TOD) files, each containing a roughly 10 minute time series for all detectors in a single array. Figure 5 shows an example TOD from Figure 1 of [23]. A selection process was applied to TOD data to cut off defective detectors or dark detectors that were not optically coupled to the sky signal. The data were then calibrated to sky temperature fluctuations using calibration observations on planets with known temperature models, such as Saturn and Uranus. The time ordered data was then ready to be made into maps with pointing functions that associate time stamps to location on the sky. Detailed data selection and calibration process is described in [5].

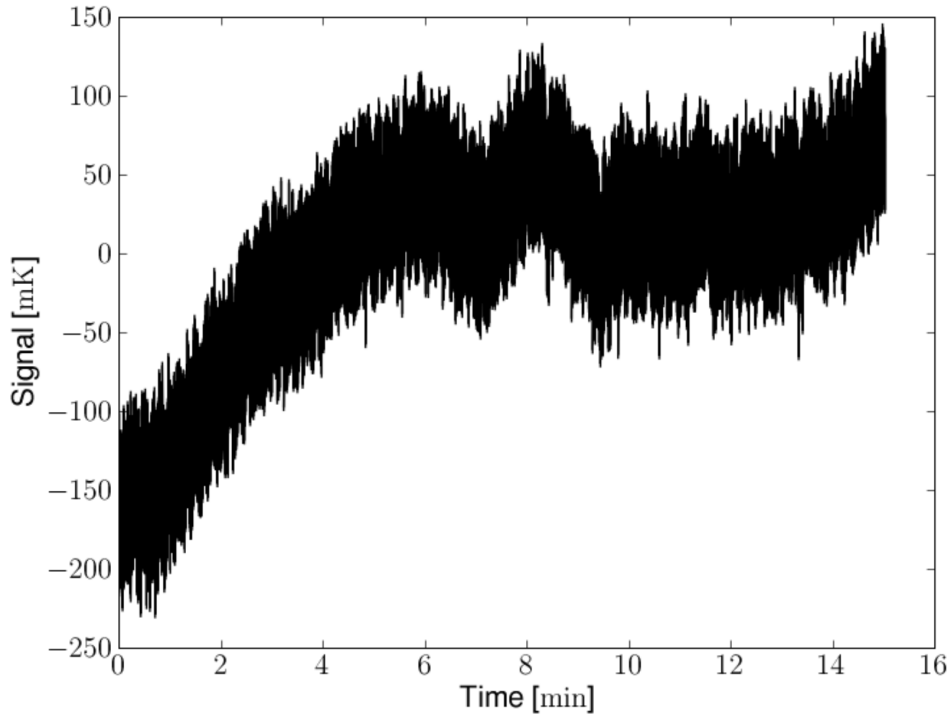

Figure 5: An example of a partial TOD from one detector taken on a good observing night at 148 GHz. Atmospheric brightness causes a slow drift in intensity. Image taken from [23].

1.4.2 Maximum Likelihood Map Making

The full maximum likelihood map making process is described in [23] but I summarize the method here. The TODs are converted to maps of the sky by maximizing the likelihood given the noise and the data model,

$$\mathbf{d} = \mathbf{M} + \mathbf{xn}. \tag{22}$$

In this case, $\mathbf{d}$ is the data, $\mathbf{M}$ is the pointing matrix, $\mathbf{n}$ is the noise model, and x is a vector containing the sky map pixels we are solving for. The goal is to find the model, $\mathbf{x}$ which maximizes the likelihood,

$$\mathcal{L} \propto \exp\left[-\frac{1}{2}\left(\mathbf{d}-\mathbf{Mx}\right)^T \mathbf{N}^{-1}\left(\mathbf{d}-\mathbf{Mx}\right)\right], \tag{23}$$

where $\mathbf{N}$ is the noise covariance,

$$\mathbf{N} \equiv \left\langle \mathbf{n}\mathbf{n}^T \right\rangle. \tag{24}$$

The least squares solution is

$$\mathbf{M}^T\mathbf{N}^{-1}\mathbf{Mx} = \mathbf{M}^T\mathbf{Nd}. \tag{25}$$

Since matrix $\mathbf{M}^T\mathbf{N}^{-1}\mathbf{Mx}$ is too large to invert, the preconditioned conjugate gradient (PCG) method is used to iteratively solve for the equation [23, 99].

For transient detection, the data are divided into time binned maps. In Chapter 2 we use approximately 3-day bins and in Chapter 3 we use single observation, or "depth-1" maps where each pixel corresponds to one observation. The maps are made using the maximum likelihood method described above. Next, a matched filter is applied to boost point source signals. This process is described in Sections 2.2 and 3.2 for the 3-day maps and depth-1 maps respectively.

1.4.3 ACT as a Transient Detector

In this section I summarize the transient detection process using depth-1 maps. The process is similar to the 3-day map analysis. Since the depth-1 analysis is an improvement on the 3-day pipeline, I present the depth-1 analysis here.

The pipeline begins with renormalizing the maps on one degree scales suitable for transient detection because the original maps are made for working with larger scales. Next we search for transients by finding any cluster of pixels with a signal to noise ratio of five or greater. Because we expect real events to be point sources, they should be the same shape as the instrument's beam. Each candidate is filtered in Fourier space to boost the signal of beam-shaped objects and degrade signals that are not beam shaped. Fluctuations not following this pattern are likely noise and are removed from the sample. This is called a matched filter. The filter functions by looking for point sources and gives and estimation of flux density F and S/N at each pixel as

$$F = \frac{\rho}{\kappa} = \frac{B^T U^{-1} \hat{m}}{\mathrm{diag}(B^T U^{-1} B)} \tag{26}$$

$$S/N = \frac{\rho}{\sqrt{\kappa}} = \frac{B^T U^{-1} \hat{m}}{\sqrt{\mathrm{diag}(B^T U^{-1} B)}} \tag{27}$$

where κ and ρ are respectively the inverse variance and inverse variance weighted flux density. B is the response matrix that takes a single pixel in flux density unit to beam-convolved structures in CMB temperature unit. U is the covariance matrix of noise u in $\hat{m}$. u is measured from the map itself and includes anything that is not a point source, including instrumental and atmospheric noise, clusters and CMB signals.

The subsequent chapters are dedicated to describing two transient detection pipelines for ACT. An example of a real transient detection is given in Figure 6, which shows cutouts of the signal to noise depth-1 maps before, during, and after a flare. The Depth-1 transient pipeline which is discussed in Chapter 3, yields 32 transient detections, including 19 new discoveries– almost doubling the number of flares discovered in ACT data from previous studies. The following chapters describe in detail the methods used to discover these transients and discuss the origins of each event.

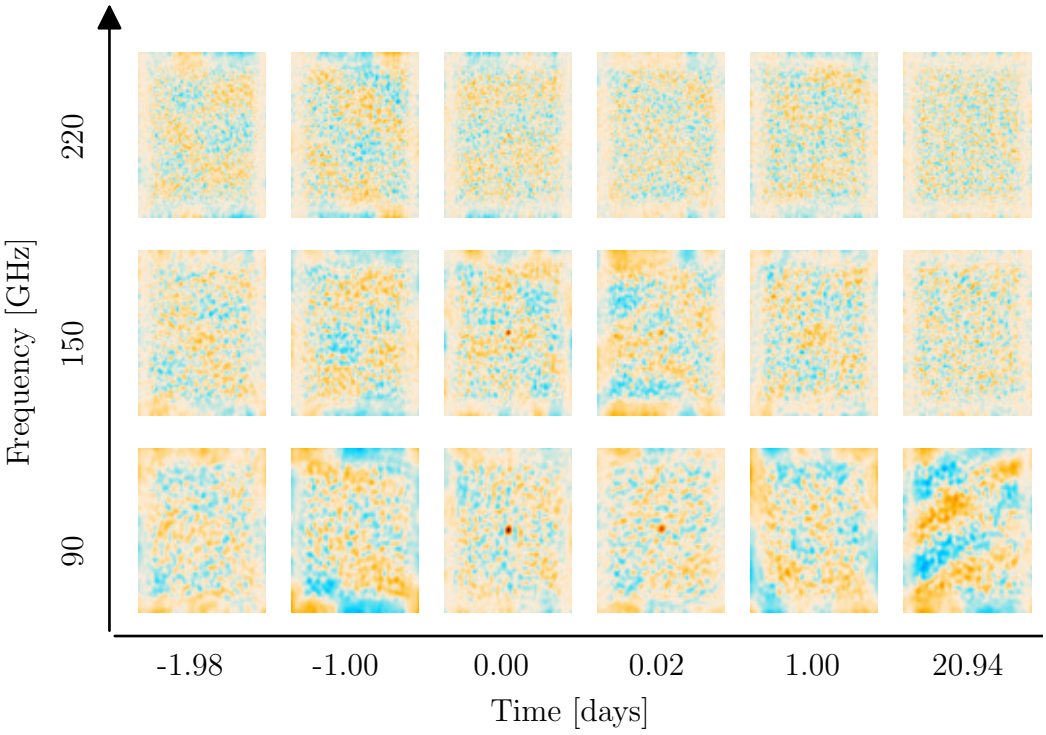

Figure 6: An example of a transient detected in sequential depth-1 maps. These maps are 0.5 deg^2 cutouts of the depth-1 signal to noise ratio maps. They are filtered on small scales to boost signals with the shape of the beam. The three rows are example depth-1 maps from each frequency band (90 GHz, 150 GHz, and 220 GHz). The x-axis is the time, in days, from the first observation of the flare. From left to right, we show the same location in each subsequent map. No source is seen before the flare, but then a transient appears before fading again. The transient appears as a red dot in the center of the map.

2.0 Systematic Transient Search of 3 Day Maps

This chapter presents an astrophysical transient search of three day coadded maps from the Atacama Cosmology Telescope. This chapter is based on a publication in The Astrophysical Journal lead by myself, Yaqiong Li, Sigurd Naess, and The ACT Collaboration. I am the second author on this publication but the first author, Yaqiong Li and I share equal contributions.

2.1 Introduction

In this work, we complete a systematic search for transient events with three years' of ACT data using spatial maps each containing about three days worth of time integrated data. In Section 2.2, we introduce the ACT survey and the maps used for this analysis. In Section 2.3, we describe how the transient events are detected and how data cuts applied to the sample. In Section 2.4, we present our findings and possible counterparts for each transient. After all cuts are applied we are left with 29 events which we then analyze in the time domain to further constrain the timescale of each event. Three of these events are redetections from [62], eight appear to be from asteroids that were not masked in the 3-day maps, and four occur in areas with poor noise models and cannot be confirmed as real transients. This leaves 14 new transient detections at 11 unique positions on the sky. Most of the events have clear stellar associations. In Section 2.5, we summarize the nature of these counterparts.

2.2 Data

We search for transient events using 3-day maps and filtering strategies originally created to search for Planet 9 [61]. The search covered $18000\,\mathrm{deg}^2$ of the sky using ACT data taken

from 2017 to 2019. Although these maps were not designed for a systematic transient search, their short timescale is well suited for this purpose. Since the beam and pointing of the daytime (UTC 11-23) observations are more affected by the Sun, the maps are made separately by the TODs spanning for approximately three days taken during daytime and nighttime by each of the three detector array at each of the two frequency bands. Therefore, there are twelve maps (day and night time data within three arrays with two bands) for each 3-day period.

For each 3-day map, a mean sky subtraction at the corresponding frequency band is implemented so only the time-varying signal remains. Regions within 0.8 degree of the planets (according to [5], a typical distance between sidelobes and planets is approximately 47 arcminutes) and within 3 arcminutes (three times of the largest beam FWHM) of the bright asteroids are masked to avoid contamination from planet sidelobes and false transient detection from known moving astronomical objects. The map is then matched filtered to look for point sources. Detailed methods and noise models for 3-day maps are described in [61].

Since the 3-day maps were made as part of a search for Planet 9, some tradeoffs are made that are suitable when performing large stacks of maps, but at times not ideal when analyzing maps in isolation. In particular the maps' matched filter numerator was computed directly in time domain while the denominator was computed in map-space. This approach is fast, but only accurate if the time-domain noise model and map-space noise model are consistent. In practice this is an approximation which introduces a bias in areas where the map hit-density changes rapidly from pixel to pixel. This does not happen when performing large stacks like in the Planet 9 search, but it is quite common when looking for objects in the individual 3-day maps, resulting in many spurious detections (see Section 2.3.1). Furthermore, the matched filtered 3-day maps are stored at 1 arcminute resolution, which was an acceptable performance tradeoff for the Planet 9 search (where this was a minor contribution to the overall smoothing budget), but is sub-optimal for blind transient detection. The ways in which the position uncertainty introduced by the selected resolution are handled is detailed in Section 2.4.2. These deficiencies are resolved in a subsequent paper (see Chapter 3) using maps tailored for transient detection.

2.3 Methodology

2.3.1 Initial Detection and Spurious Candidate Cuts

Any pixel or group of pixels with $S/N > 5$ in the 3-day sky-subtracted maps is considered a transient candidate. For each set of 3-day S/N and flux density maps, we first mask pixels with $S/N < 5$, then apply this mask to the corresponding flux density map (Figure 7). The positions of candidates are evaluated to be the flux-weighted centroids. We then cross match each candidate between detector arrays with a matching distance of 1.5 arcminutes, which is 1.5 times the resolution of the 3-day maps . We only keep candidates that appear in at least two frequency and array combinations. This cuts 76% of the initial detections.

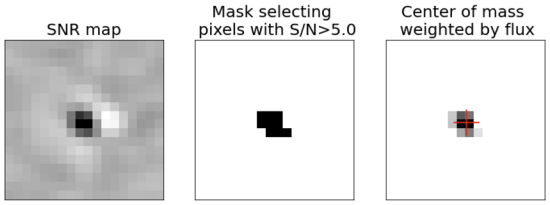

Figure 7: Process of the initial detection, with each plot showing a 0.3 deg by 0.3 deg map. The first step is to make a mask (middle) on S/N map (left) selecting pixels that have $S/N > 5$. The mask is then applied to the flux map (right), and the candidate position, shown as the red cross mark, is evaluated as the center of mass weighted by the flux values within the selected pixels.

Even with this cut applied, there are still many spurious detections grouped in clusters and along map edges. Given that 7.8 billion pixels are searched for each combination of array and frequency band, we expect to find around 28 thousand false detections in total assuming a Gaussian distribution with the 5σ detection threshold (0.00006%). The probability will be squared to have a false detection at the same or adjacent pixels on different maps. In ideal situations, the false detection would be negligible after cross matching catalogs from different arrays in the same 3-day period. However, due to the bias and estimation in the mapmaking and filtering process described in Section 2.2, this initial detection finds 332,333 candidate

events, which is a magnitude higher than expected. We perform three additional geometric cuts, requiring a candidate to be cut in all detected frequency and array combinations to exclude it from the analysis. The results of these cuts are summarized in Table 2.[1] We apply these cuts in tandem to the frequency and array requirement, thus the following statistics include all candidates.

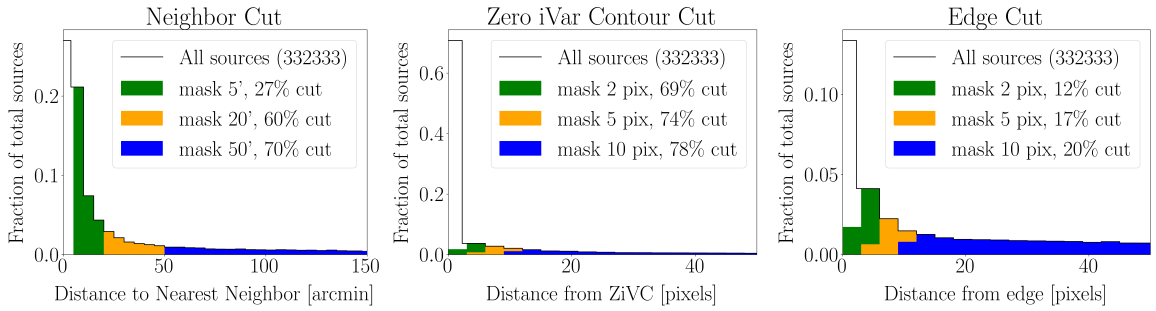

Figure 8: ***Left:*** A histogram of the distance to each detection's nearest neighbor with a binsize of 5 arcminutes. The peak close to zero indicates there are clusters of spurious detections in many of the maps so we cut any candidate with a nearest neighbor of 20 arcminutes or less. ***Center:*** A histogram of each candidate's distance from the nearest zero inverse variance contour, defined to be an inverse variance of less than $1.5 \times 10^{-5} K$, with a bin size of 3 pixels. There is a large peak of candidates near zero inverse variance contours which drops after 3 pixels. We mask out to 5 pixels, cutting 74% of all sources. ***Right:*** A histogram of each candidate's distance from the map edge in pixel units with a bin size of 3 pixels. As expected, there is an excess number of candidates near the edge of the map as the map edges are noisy and so appear variable when sampled every three days. At a mask size of 5 pixels, we cut off the peak of candidates near the edge.

The first geometric cut is motivated by the observation that many of the 3-day maps exhibit a stripy pattern of spurious detections along the scanning direction. These false detections are caused by a systematic underestimation of the inverse variance (i.e. the κ maps mentioned in section 2.2) when the coverage is uneven due to low hit counts. The stripy regions are reliably identified by searching for detections with nearby neighbours within

[1]Note that a candidate might be cut by more than one criteria

the same 3-day day map. This approach is motivated by the lefthand plot in Figure 8 which shows a histogram of each candidate's nearest neighbour: there is a clear excess of detections with neighbours within $\sim$1 deg, which would not be expected for real detections since extragalactic transients should be spatially uncorrelated. Based on this histogram, we cut any candidates with a neighbor within 20 arcminutes as there is an overdensity of detections with a closest neighbor within this range. This cut removes 60% of all candidates.

We see a similar stripy pattern along zero inverse variance contours. During the map making process, some approximations result in streaks of spurious detections with vanishing inverse variance and therefore a high S/N. In the center plot in Figure 8 we plot a histogram of the candidates' distances from a zero inverse variance region and cut any candidate within 5 pixels of these features (about 74% of all candidates).

Lastly, we cut any candidate near a map edge. Map edges are especially noisy and appear to be variable when sampled every three days. In the right-hand plot in Figure 8 we plot a histogram of the pixel distance of each candidate from the edges of the map. We see a spike in candidates within five pixels from the map edge and so we mask this region. This cuts applies to 17% of all candidates.

After these cuts are applied an internal cross match is performed to find repeating events. Candidates with positions within one arcminute of each other are considered the same object. This leaves us with 667 independent candidates.

2.3.2 Candidate Verification

For each of the 667 candidates, we calculate the mean flux by applying a matched filter to the mean sky map using data from 2017 to 2021, and mask candidates with mean fluxes of > 50 mJy or < -50 mJy. The high-mean-flux candidates are likely variable point sources such as AGN or dusty star forming galaxies (DSFG). These high-mean-flux candidates are already detected in our standard point source catalogs, and there are dedicated studies in preparation on the light curves of these candidates. In this paper we will concentrate on candidates that are not detectable in the mean sky maps. The candidates with negative mean fluxes are located close to bright point sources. The flux density around this region is

	Remaining Candidates	Fraction Cut	Fraction of map masked
frequency and array cut	78,367	0.76	–
neighbor cut	133,119	0.60	0.005
ZiVC cut	88,936	0.74	0.030
edge cut	278,044	0.17	0.010
all cuts	5,020	0.94	0.045

Table 2: This table summarizes the three geometric data cuts applied to each 3-day map after the requirement that a candidate appear in at least two frequency or array combinations is applied. The first column quotes the number of candidates remaining after that cut, the second gives the fraction of all candidates that do not pass these cuts, and the last column gives the fraction of the total number of pixels masked by each cut. Note that these cuts are done in tandem and are independent from each other. The neighbor cut removes candidates with neighbors in the same map within 20 arcminutes, the zero inverse variance contour (ZiVC) cut masks candidates within five pixels of zero inverse variance contours, and the edge cut masks candidates within five pixels of the edge.

negative due to the effect of the matched filter that acts as high pass filter, and will increase when the flux of the corresponding point source decreases, resulting in a false detection. There are 82 candidates left after applying the cut on mean flux. We then make light curves to confirm these detections, requiring a $S/N > 3.5$ in at least two arrays or in one array at both frequency bands. These light curves are made from forced photometry, which gives a per-detector flux and flux error, and then evaluating a weighted mean flux as the array-wise result at each frequency band for each scan. This analysis further cuts 41 candidates.

For the rest of the candidates, we made 2° by 2° intensity maps (shown in Figure 9) from TODs covering a three day period (or shorter if the scanning cadence is especially high) centered on each event. These maps, referred as "thumbnail maps," have 0.25-arcminute resolution and are centered at the candidate positions. We visually inspected these maps

both before and after matched filtering[2] and remove candidates with an extended or irregular shape, since we expect all our transients to be point sources. This issue may be caused by poor data quality causing arcminute scale fluctuations. This step is done manually since the amount of candidates left are small, but a future effort will be dedicated into developing an automatic process of point-source classification. For some of the remaining candidates, we observed that the raw and filtered maps appear discrepant with each other, e.g. a supposedly strong detection having no visible counterpart in the maps before filtering; or there was an overdensity of $> 3\sigma$ peaks near the event in the filtered maps, which should not happen if the noise model is correct. Different from other confirmed false candidates, switching to different noise modeling methods would improve the overdensity issue and the candidates' shape at the expense of decreasing the S/N in signal. Therefore, we do not discard these events, but classify them as low quality candidates.

2.4 Results

After all cuts are applied, we are left with 29 transient detections. Eight of these events are due to asteroids (see section 2.4.2), three were previously detected, and four are low quality candidates. In this section we use this event rate to calculate the transient surface density of ACT 2.4.1, characterize the properties of each event, 2.4.2, and look for counterparts by crossmatching the positions with other surveys 2.4.3.

2.4.1 Transient Surface Density

We estimate the surface density of transients in ACT's field of view following the method outlined in [78]. Note that for the following calculations we only include 14 strong transient candidates. We calculate the sky area in each frequency band and array by dividing maps with the edge and zero inverse variance contour cuts applied into 0.5 by 0.5 degree tiles. The

[2]This is pure map-space matched filtering, which should be more accurate than the mixed TOD-level/map-space matched filtering used in the main 3-day maps used for the initial search, but still depend on an accurate noise model.

Figure 9: 10 arcminutes x 10 arcminutes 3-day thumbnail maps for each transient. The upper row is the intensity map with ± 5000 μK color range. The bottom row is the S/N map after applying a matched filter, with ± 5 color range. Due to the conjugate gradient iteration used to solve the maximum-likelihood map-making equation only being run for 10 steps, these maps are effectively mildly highpass filtered. The affected scales have negligible weight in the matched filter. Events 2, 9, 10, 13 at the bottom of the table are the four events that are difficult to determine if they are real transients.

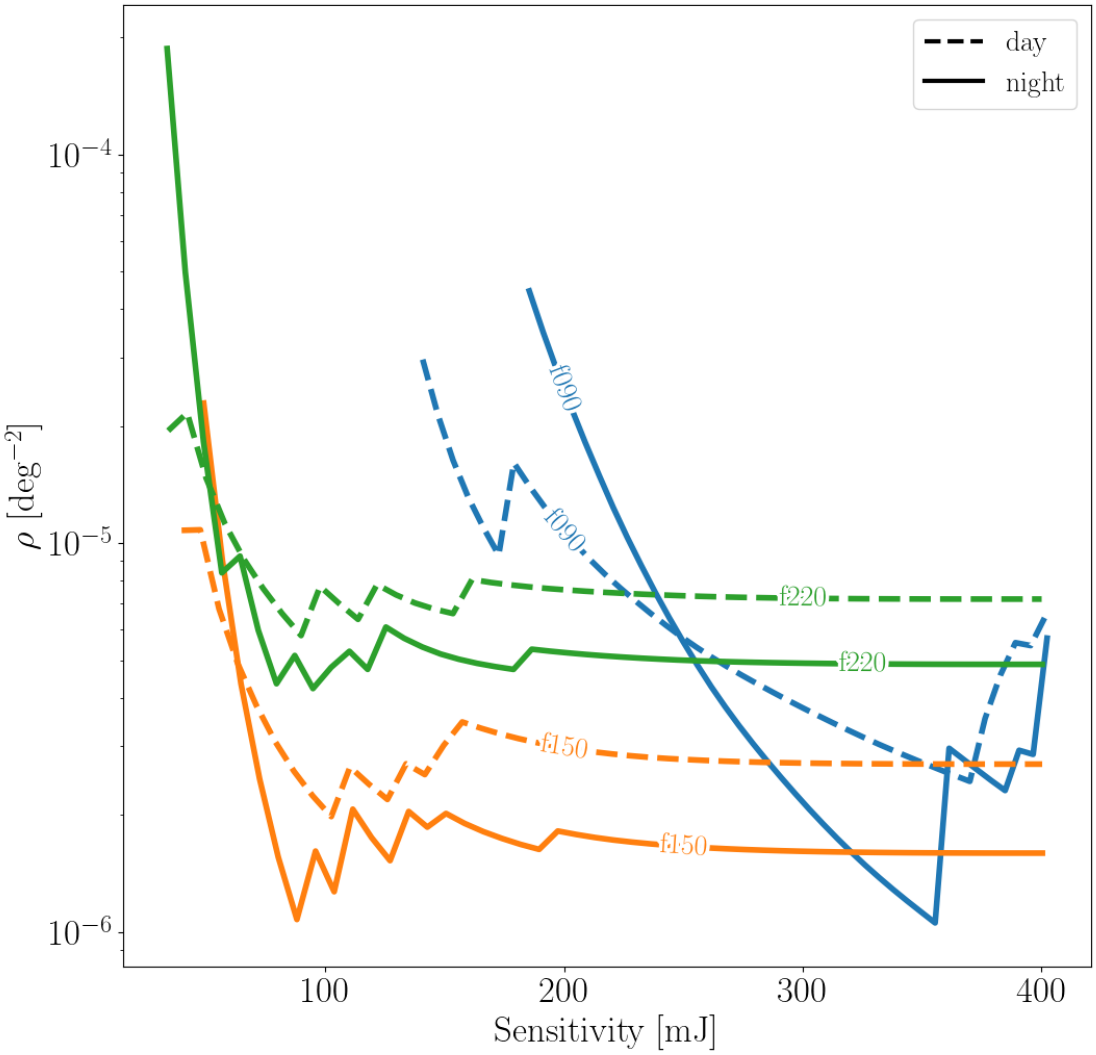

Figure 10: Surface density of transients for each frequency split between day and night data. The surface density is found by counting the number of transients we are able to detect given the sensitivity level divided by the map area at that sensitivity or lower.

surface density, ρ is then $T/(0.25 \text{ deg}^2 N)$ where T is the number of transients we observe and N is the average number of tiles across all frequency and array combinations. We find

the transient surface density for this analysis to be $7.06 \times 10^{-6}[\text{deg}]^{-2}$.

We also provide the surface density as a function of sensitivity using the method described in [78]. First, we split the maps by frequency and day/night data as the variance in each of these maps differs significantly. We find the root mean square (rms) noise in each 0.5 deg tile and split the values into 50 bins. The sensitivity of each bin is simply the noise multiplied by our 5σ detection threshold. The surface density is calculated by finding the cumulative area of each bin and the cumulative number of transients detectable at each sensitivity level. The results are shown in figure 10 and are summarized in table 3. The table quotes the surface density of the highest sensitivity bins. Note that most of these values are lower than the total surface density quoted above as these calculations only include transients found during the day or night of each frequency band.

We can most directly compare ACT's transient surface density to the transient survey conducted by SPT-3G [30] since ACT and SPT observe in similar wavebands. SPT observes a 1500 square degree footprint of the sky every 16 hours. The transient search yielded 15 events over 3500 hours of observations. Therefore, the transient surface density of SPT-3G is roughly $4.57 \times 10^{-5}[\text{deg}]^{-2}$, over an order of magnitude higher than ACT. This difference can be explained in a few ways. The SPT-3G transient search has noise levels on the order of 5mJy which is much lower than the noise levels for this survey (around 15mJy). In addition, we expect to overcut many real transients due to the map approximations causing false detections at low hit counts. Finally, ACT surveys a much larger sky area with a less regular cadence than SPT which also results in missing stellar flare events. Whereas SPT will re-observe the same location once every day, ACT's cadence varies from less than one day to two weeks. We are therefore most sensitive to transients with flare durations on the order of days. We indeed find that most of our detected transients flare on this timescale.

2.4.2 Characterization

Two groups of our transient events appeared to be close in time and space to each other (see Table 4). Using the IAU Minor Planet Center NEOChecker webtool,[3] we found three

[3]See https://minorplanetcenter.net/cgi-bin/checkneo.cgi

frequency	ρ [deg^{-2}] Day	ρ [deg^{-2}] Night
f090	6.52e-06	5.69e-06
f150	2.70e-06	1.59e-06
f220	7.18e-06	4.88e-06

Table 3: Transient surface density for each frequency split between day and night data. These values represent the surface density for the highest sensitivity required to detect one of our transients. We split this measurement between frequencies and day and night data since the sensitivity thresholds of these maps are very different. The average transient surface density across all frequencies and arrays is 7.06×10^{-6}[deg]$^{-2}$

.

events to be coincident with asteroid 10 Hygiea and five events to be coincident with asteroid 511 Davida. In Figure 11, we plot the paths of these asteroids with our events overlayed. All eight events appear consistent in space and time with the asteroid observations which were not masked in our maps. For future blind transient searches we must be prepared for the possibility of detections from moving objects such as asteroids. This will become especially important for real-time follow-up observations. Furthermore, measurements of mm fluxes of asteroids are of scientific interest for characterising their regoliths, which the ACT collaboration did in [66].

The properties of the remaining 21 transient events are shown in Table 5. Three single detections labeled as "N" were previously published in [62]. Among the newly detected events, 12 are single events and three repeat twice, with time intervals ranging from one month to one year. The low (1 arcminute) resolution of the 3-day maps potentially increases the candidates' position error, so we re-estimate the candidate positions using a method similar to the one used in the initial detection on the higher-resolution thumbnail maps described in Section 2.3.2. We first subtract the corresponding f220/f150/f090 mean sky map and apply a matched filter. The final position for each candidate is the inverse-variance-weighted average among individual positions, using the ratio between half maximum of the

Name	RA °	Dec °	Pos.	Peak Flux (mJy)			Mean Flux (mJy)			Peak	α
			Acc.″	f220	f150	f090	f220	f150	f090	Time (UTC)	
Hygiea(a)	285.1166	−23.9962	14	334 ±71	199 ±21	104 ±20	1.4 ±4.0	1.3 ±1.5	0.8 ±2.6	2017-05-21 04:27	1.4 ±0.3
Hygiea(b)	274.0251	−23.4008	5	369 ±42	218 ±18	92 ±20	19.1 ±6.7	3.0 ±2.6	0.5 ±4.6	2017-07-24 05:50	1.5 ±0.2
Hygiea(c)	273.7942	−22.6426	10	351 ±52	144 ±20	65 ±19	18.5 ±7.3	8.5 ±2.8	−0.2 ±5.0	2017-09-09 02:54	2.1 ±0.4
Davida(a)	117.7733	16.5879	8	206 ±34	114 ±15	53 ±14	4.0 ±2.1	1.9 ±0.8	−1.9 ±1.4	2019-10-24 09:01	1.6 ±0.3
Davida(b)	122.6793	18.2278	5	277 ±32	155 ±13	57 ±12	−0.8 ± 2.1	0.2 ±0.8	4.0 ±1.4	2019-11-30 07:12	1.8 ±0.2
Davida(c)	122.6946	18.3167	8	192 ±39	118 ±16	57 ±13	−2.2 ±2.0	0.3 ±0.8	3.1 ±1.3	2019-12-01 08:57	1.6 ±0.4
Davida(d)	122.4329	19.3231	2	343 ±27	162 ±14	86 ±10	5.1 ±2.0	1.1 ±0.7	3.3 ±1.3	2019-12-11 06:45	1.7 ±0.2
Davida(e)	122.0468	19.9151	6	313 ±44	174 ±16	62 ±15	−5.1 ±1.9	0.8 ±0.8	1.8 ±1.4	2019-12-16 05:10	1.8 ±0.3

Table 4: Eight events associated with asteroids.

beam and the appropriate S/N as weights. The position accuracy is evaluated by the square root of the variance of weighted mean. As mentioned in Section 2.3.2, four out of the 12 single events are difficult to determine if they are real transients due to unusual noise patterns on the intensity maps. We present these events at the bottom of the table without assigning a formal name.

Flux densities for each scan are evaluated at the refined positions and used to generate light curves (Figure 12) using the same method described in Section 2.3.2. Higher-resolution light curves (Figure 13) are made by dividing detectors in each array into four groups by the order of observation time to study the minute by minute change in flux density. When the flux density values are available in both bands of PA4 and PA5, the spectral index α is

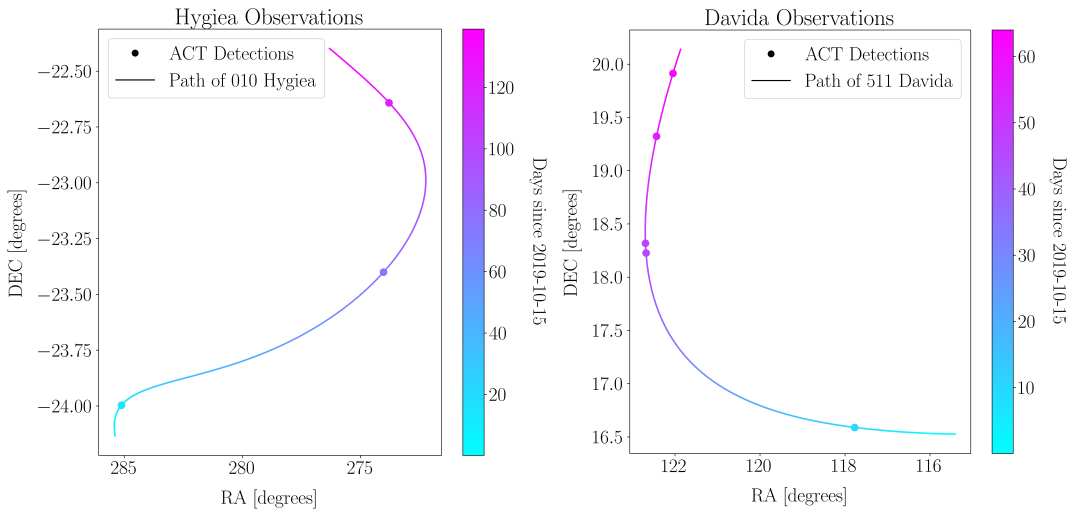

Figure 11: ***Left:*** The three transient events consistent with Hygiea observations. ***Right:*** The five transient events consistent with Davida observations. All of the plotted positions and observation times are consistent with the asteroids' paths. The position errors are on the order of 0.1 arcminutes.

evaluated by the best-fit of a power law $S_\nu \propto \nu^\alpha$ of frequency ν to the flux measurement S_ν at the three different bands, taking into account the variance of each band flux. Under this circumstance, PA6 is omitted because it scans across the candidates approximately 10 minutes earlier (or later when the sky is rising) than PA4 and PA5. Events 2 and 15 do not have f220 measurements, so α is directly calculated by

$$\alpha = \frac{\log(S_{\nu_1}) - \log(S_{\nu_2})}{\log(\nu_1) - \log(\nu_2)} \tag{28}$$

using the f150 and f090 flux measured by PA5 or PA6, depending on which array measures the peak flux.

2.4.3 Counterparts

We searched for counterparts for each transient event in the SIMBAD[4] [96] database. The results of this search are summarized in Table 6. We searched for any Gaia objects [27] within one arcminute of each event and list the SIMBAD identification. We calculate the probability of a chance association given the density of Gaia stars [27] with the counterpart's magnitude or lower within the counterpart's separation of the transient's position. We exclude any counterparts with a chance association probability greater than ten percent. We also searched for counterparts of the transients found in [62] that are recovered in this analysis. The associations agree with the original findings.

In addition to the Gaia source catalog, we search for galactic objects in the Gaia extra-galactic catalog [27] using the VizieR [65]. Only events 10 and 14 have associations from this catalog. Event 10 is coincident with an AGN with a 1.1 percent chance of a false association (see Table 6). Event 14 is coincident with a RR Lyrae star with a 2.4 percent chance of a false association. This association is not listed because there is a much more obvious Gaia star associated with event 14.

In Figure 14 we plot the positions of the transients overlayed on combined ACT data from 2007–2019. This plot includes color images in the optical from the Digitized Sky Surveys (DSS)[5][6] that show there are bright stellar counterparts for most of the events.

[4]https://simbad.cds.unistra.fr/simbad/

[5]https://archive.stsci.edu/cgi-bin/dss_form

[6]These images were acquired using the online tool Aladin Lite. See [8].

2.5 Discussion and Conclusions

We have demonstrated a pipeline of transient detection and characterization using ACT data, and presented a catalog of 21 millimeter transients from 3-day maps, including three of which that were previously detected, and four events that cannot be confirmed as real transients. After assessing the spectral indices and counterpart associations of these events, two classes of objects emerge: flares associated with stars with flat or falling spectra, indicating radiation from sychrotron emission, and stellar flares with rising spectra, indicating thermal emission. Performing a statistical analysis on such a small sample size is difficult, but in the future as we discover more millimeter stellar transients, we will be able to better characterize them. For example, we will be able to determine whether these events reside near the galactic plane or scattered across the sky, or whether two classes of transients, rising versus falling spectra, really exist or if there is simply a wide distribution of spectral indices. Tests of these statistics with our small number of events are inconclusive.

Events 3, 4a, 4b, 5a, 5b, 11, 12a, 12b, and 15 are associated with rotating variable stars. These stars have large dark spots on their surface from magnetic activity in their chromospheres. These spots cause intrinsic variability in flux in optical and IR wavelengths but also cause flares in radio wavelengths from synchrotron radiation [35]. Events 4, 11, 12, and 15 are coincident with a special type of rotating variable stars called RS Canum Venaticorum variables (RSCVn). These are binary systems that also exhibit variability due to dark spots (See [32], [104]). Similar events were seen in the millimeter systematic transient search from SPT-3G [30].

Event 1 is also associated with a binary system. Although it is not classified as rotationally variable, it most likely flares in the microwave with a similar mechanism. This association is similar to ACT-T J200758+160954 (N3) which was previously published in [62].

Events 7, 8, and 15 are all coincident with cool G, K, and M type stars. Event 14 is associated with a Gaia star but its spectral type is unknown. Since all of these events also have negative spectral indices, these flares are most likely from magnetic activity producing synchrotron radiation. This is consistent with findings from [30] who reported microwave

flares from M and K dwarfs. These cool stars have convective envelopes which cause increased magnetic activity but do not exhibit the same dark spots found in rotationally variable stars [101].

Events 6, N1, and N2 all have rising spectra which are associated with thermal emission. In these cases, some mechanism other than synchrotron radiation is driving the flares. N1 and N2 are associated with cool M and K stars respectively but the spectral types of the star associations for 6 and 9 are unknown. [30] also observed two events with M-dwarf counterparts with rising spectra indicating this is a common class of millimeter transients.

Although we cannot be certain events 2, 9, 10, and 13 are real transients, we still present possible counterparts for them in Table 6. There is a six percent chance that the Gaia counterpart for Event 2 is a chance association. If the association is correct this transient is likely due to synchrotron radiation from stellar magnetic fields. The field around Event 10 is too dense to pinpoint a stellar counterpart. However, there is a small chance this event is associated with an AGN. [24] predicts ACT will see on the order of ten gamma ray bursts but this event is not associated with any known GRB flares listed in the Fermi All-sky Variability Analysis [3]. The associations for Events 9 and 13, are also unclear. Both events have rising spectra so they would most likely be similar to events 6, N1, and N2. The Zwicky Transient Facility (ZTF; [56]) detected a flare with the same Gaia counterpart associated with event 13 twelve days after and 23 arcseconds away from the ACT detection. ZTF also detects repeating flares that are 34 arcseconds away from Event 9, although they did not occur close in time to the ACT detection.[8].

This sample likely only represents a fraction of microwave transient events present in the ACT data. The 3-day maps were not made for a systematic transient search. Recently, single observation maps that span more seasons than the 3-day maps have been made for the purpose of ACT time domain study. Major advantages of the single observation maps include the relative consistency in noise performance in each map, thus decreasing the likelihood of over-cutting our initial transient detections, and the freedom of stacking single scan maps for different periods of time. We will perform a similar analysis to search for transient events within those maps to gain a more accurate event rate for ACT. This will inform current

[8]This cross detection was done using software developed by [58]

and future large sky-area millimeter surveys such as The South Pole Telescope [13], Simons Observatory [4], CCAT-prime [14] and CMB-S4 [2] on how to best detect and study these events. In particular, the SO (and Advanced SO) large aperture telescope, or SO LAT, will be outfitted with ten (twenty) times the number of detectors as ACT, increasing the sensitivity to be a factor of $\sqrt{10}$ better than ACT maps. SO LAT will also have a larger field of view and a more regular cadence than ACT further improving its ability as a transient detector.

Ind	Name (ACT-T)	RA °	Dec °	Pos. Acc.″	Peak Flux (mJy)			Mean Flux (mJy)			Time			α
					f220	f150	f090	f220	f150	f090	Peak (UTC)	Rise	Fall	
1	J060702 +174157	91.7603	17.6993	22	36 ±35	78 ±13	64 ±14	−1.2 ±2.3	−2.3 ±0.9	−4.6 ±1.6	2017-09-05 05:35	< 43 min	< 25 h	0.0 ±0.5
3	J224500 -331532	341.2510	−33.2589	14	192 ±41	253 ±20	255 ±12	5.5 ±2.3	4.4 ±0.8	8.8 ±1.4	2017-10-08 18:17	< 1 d	> 23 min	−0.6 ±0.2
4a	J225302 +165027	343.2597	16.8408	8	1036 ±122	1154 ±52	801 ±34	4.7 ±3.2	7.8 ±1.1	18.7 ±2.0	2018-09-10 21:55		< 2 d	0.5 ±0.1
4b					−15 ±58	141 ±20	148 ±18				2019-06-06 04:18	< 2 d	< 3 d	−0.6 ±0.4
5a	J192831 -350757	292.1328	−35.1327	3	2496 ±177	2383 ±40	1525 ±27	4.7 ±3.7	11.7 ±1.4	37.2 ±2.7	2018-10-04 02:22	< 1 d	< 20 d	0.9 ±0.05
5b					545 ±69	645 ±23	490 ±20				2019-08-10 23:10	< 3 d	> 1 d	0.4 ±0.1
6	J190222 -53610	285.5938	−5.6028	10	926 ±87	717 ±34	350 ±29	12.7 ±5.6	5.3 ±2.1	7.7 ±3.9	2018-10-20 20:32	< 1 d	< 1 d	1.2 ±0.1
7	J085813 +194546	134.5579	19.7630	4	103 ±31	197 ±9	269 ±9	3.0 ±1.9	0.1 ±0.8	2.4 ±1.5	2018-11-15 05:18	< 5 d	< 22 h	−0.8 ±0.1
8	J142555 +141207	216.4831	14.2020	8	446 ±61	563 ±17	562 ±14	−0.5 ±1.9	1.7 ±0.6	5.6 ±1.1	2018-11-21 08:07	< 20 h	> 23 h	−0.1 ±0.1
11	J060757 -542626	91.9890	−54.4408	20	108 ±65	113 ±21	113 ±15	-3.6 ±2.6	0.8 ±1.0	2.6 ±2.1	2019-08-09 12:18	< 24 h	< 18 h	0.0 ±1.6
12a	J033647 +03511	54.1961	0.5865	5	108 ±66	302 ±26	448 ±25	11.7 ±4.0	11.9 ±1.5	30.1 ±2.8	2019-08-10 13:35	< 30 h	> 23 h	−1.1 ±0.2
12b					356 ±67	487 ±23	580 ±21				2019-09-28 10:23	> 2 d	< 2 d	−0.5 ±0.1
14	J125045 +113338	192.6887	11.5607	14	76 ±114	202 ±29	218 ±21	−1.8 ±1.8	1.8 ±0.6	5.4 ±1.2	2019-09-17 11:34	< 1 d	< 49 d	−0.3 ±0.4
15	J180723 +194222	271.8483	19.7063	14	NA	82 ±24	153 ±19	0.5 ±2.2	2.8 ±0.8	5.5 ±1.6	2019-11-13 13:01	< 6 d	< 12 d	−1.4 ±0.7
N1	J181515 -492746	273.8166	−49.4627	5	NA	555 ±28	282 ±18	−2.5 ±5.7	6.4 ±2.2	16.0 ±4.7	2019-11-08 17:22	> 8 min	> 4 min	1.3 ±0.2
N2	J070038 -111436	105.1588	−11.2458	10	NA	344 ±30	152 ±21	−1.8 ±7.2	5.5 ±2.7	4.5 ±5.2	2019-12-14 21:30	< 8 d	> 8 min	1.9 ±0.5
N3	J200758 +160954	301.9965	16.1642	7	222 ±53	300 ±26	346 ±18	-2.2 ±3.0	2.7 ±1.1	15.4 ±2.1	2018-09-11 19:36	< 1 d	> 3 d	-0.4 ±0.2
2		316.0950	−13.6699	20	NA	1050 ±56	1311 ±30	0.9 ±4.5	−2.7 ±1.6	−2.0 ±3.0	2017-09-27 00:21	< 6 min	< 1 d	−0.5 ±0.1
9		196.7753	16.6089	21	168 ±52	117 ±19	12 ±16	0.6 ±1.7	0.0 ±0.6	1.2 ±1.1	2019-07-19 19:23	< 3 h	> 22 h	2.1 ±0.6
10		208.4267	6.7745	23	293 ±57	200 ±21	110 ±19	−1.5 ±2.0	0.2 ±0.7	0.3 ±1.3	2019-08-05 14:40	< 19 h	< 1 d	1.2 ±0.3
13		60.9932	14.0094	26	920 ±103	542 ±52	603 ±44	−2.1 ±3.3	1.7 ±1.2	1.2 ±2.3	2019-08-14 09:27	< 5 min	< 2 min	1.6 ±0.2

Table 5: Properties of the transient events. The candidates are listed in the order of the detection time (or the detection of the first event for the repeating candidates). Three single detections labeled as "N" are the redetections of the transients published in [62]. It is difficult to fit for rise and fall time using light curves due to uneven scanning cadence. Instead, we examine if the scan right before and after the scans with the peak flux density has a $> 5\sigma$ detection, and calculate the time interval in between the scans. The rise time of Event 4a is left empty because the time gap between the peak scan and the scan right before is longer than 50 days. Spectral index is evaluated as described in text, using array-wise flux density values, except for candidate 13. This transient event completed the rise and fall process within the time the sky took to drift across the array. We therefore evaluate the spectral index using flux values taken by only one quarter of detectors in each array, to capture the peak flux.

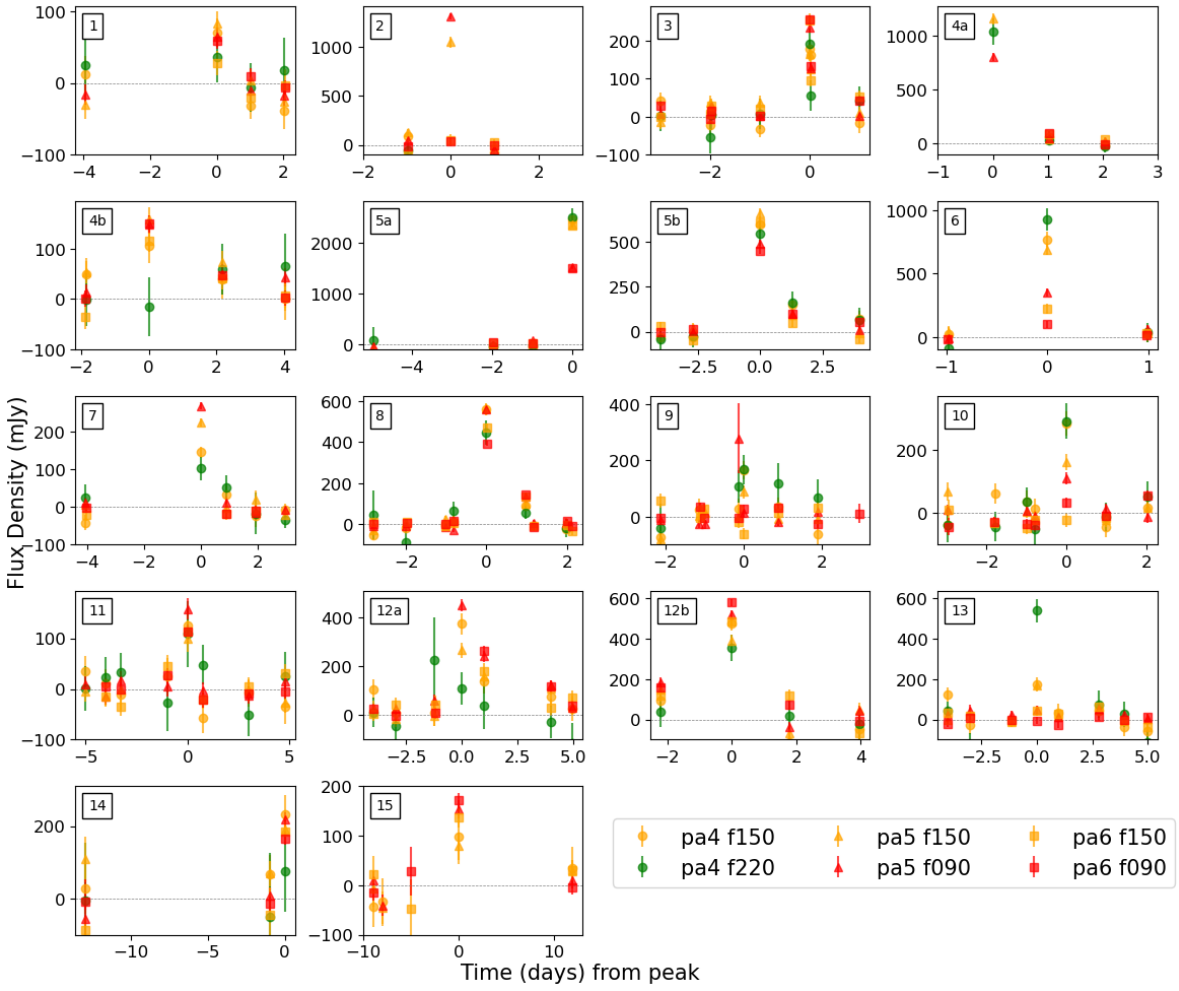

Figure 12: Light curves for 18 detected transient events on day time scales from the peak. Each frequency is denoted by a different color. We see that in most cases the peak is correlated with all frequencies.

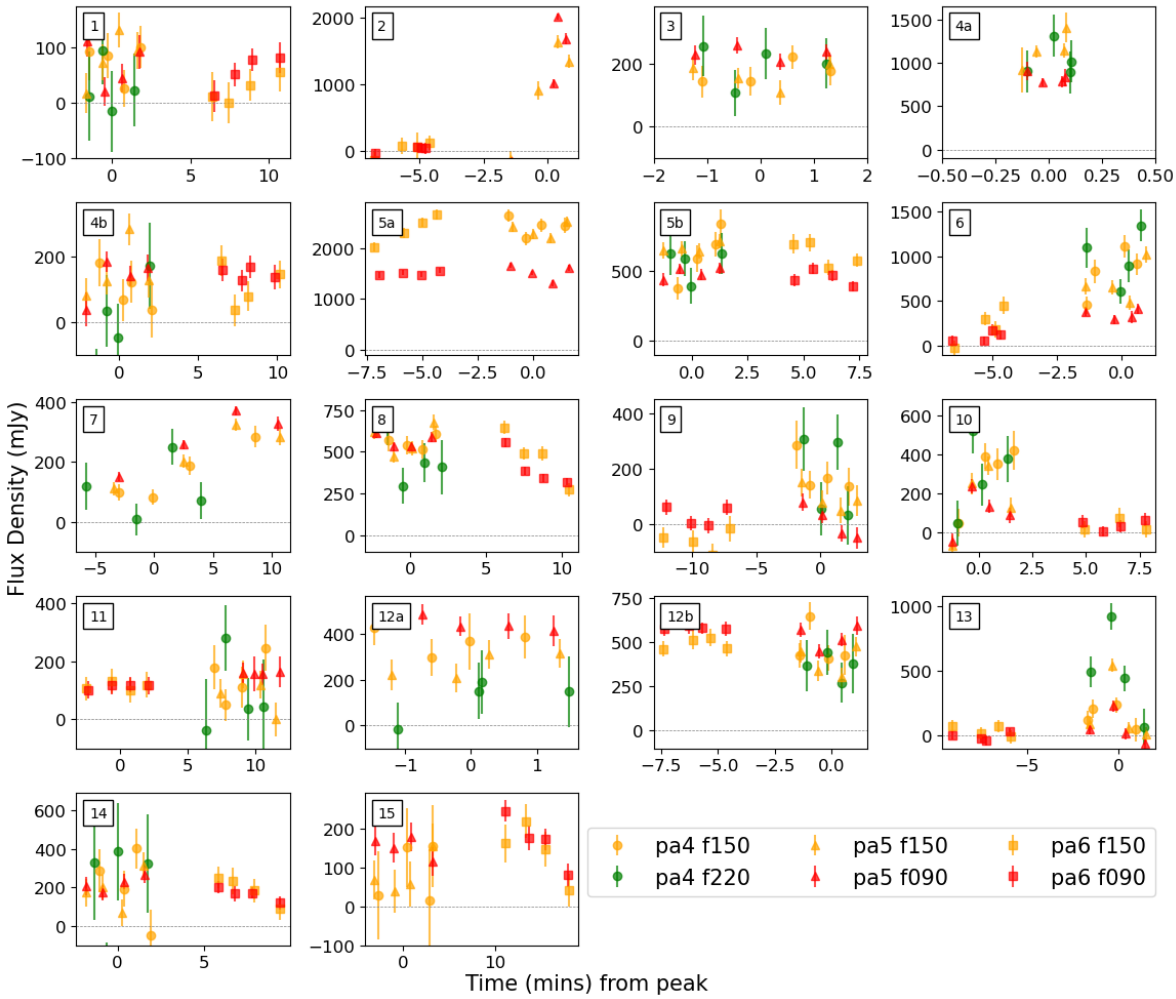

Figure 13: High-resolution light curves for transient events on minute time scales. Events 1, 2, 5, 6, 7, 8, 9, 10, 13, 14 and 15 show strong signal variation within a space of four minutes.

Name	ID	Object Type	Magnitude	Pos Err (")	Sep (")	Chance
1	V* CP Ori	Eclipsing Binary, G0	10.52	22	8.60	5.66e-04
3	V* TX PsA	Eruptive Variable, M5IVe	11.84	14	4.24	1.21e-04
4a/b	V* IM Peg	RS CVn Variable, K2III	5.66	8	1.48	4.23e-08
5a/b	HD 182928	Rotating Variable, G8IIIe	9.37	3	2.15	5.79e-06
6	** SKF 1810A	Young Stellar Object Candidate	12.73	10	7.00	5.05e-03
7	G 9-38	High Proper Motion Binary, M7V/M8Ve	12.49/11.97	4	4.03	1.56e-04
8	StKM 1-1155	Low-mass Star, M0.0Ve	10.91	8	2.71	1.78e-05
11	V* TY Pic	RS CVn Variable, G8/K0III+F	7.29	20	6.80	9.82e-06
12a/b	HD 22468	RS CVn Variable, K2:Vnk/K4	5.60/8.51	5	4.10	2.59e-07
14	Gaia DR2 3927810990205301504	Star	12.43	14	2.88	5.96e-05
15	HD 347929	Rotating Variable, K0	9.04	14	7.66	8.04e-05
N1	2MASS J18151564-4927472	High Proper Motion Star, M3	11.72	5	4.25	5.47e-04
N2	HD 52385	Star, K0/1III	8.11	10	7.46	5.15e-05
N3	HD 191179	Spectroscopic Binary, G5	7.96	7	7.05	4.41e-05
2	Gaia DR2 6885400713762009216	Star	16.74	20	13.02	5.96e-02
9	Gaia DR2 3936693910286240000	Star	13.87	21	33.51	2.11e-02
10^7	1636148068921376768	AGN	–	23	17.40	1.20e-02
13	Gaia DR2 38908044312695424	Star	14.34	26	23.58	2.51e-02

Table 6: Possible counterparts for each transient event from the SIMBAD database. If known, the spectral type is given next to the object type. The chance of a false association is calculated using the density of Gaia sources with the same magnitude or brighter of the counterpart. If the Gaia object is not found in the SIMBAD database, then the Gaia identification number is listed. All separations are calculated using the Gaia coordinates. This table also includes counterparts associated with the three previously published ACT transients from [62]. When two stars from the same system are resolved, as is the case with events 7 and 12, we quote the average separation weighted by one minus the chance association and we list the lowest of the two chance associations.

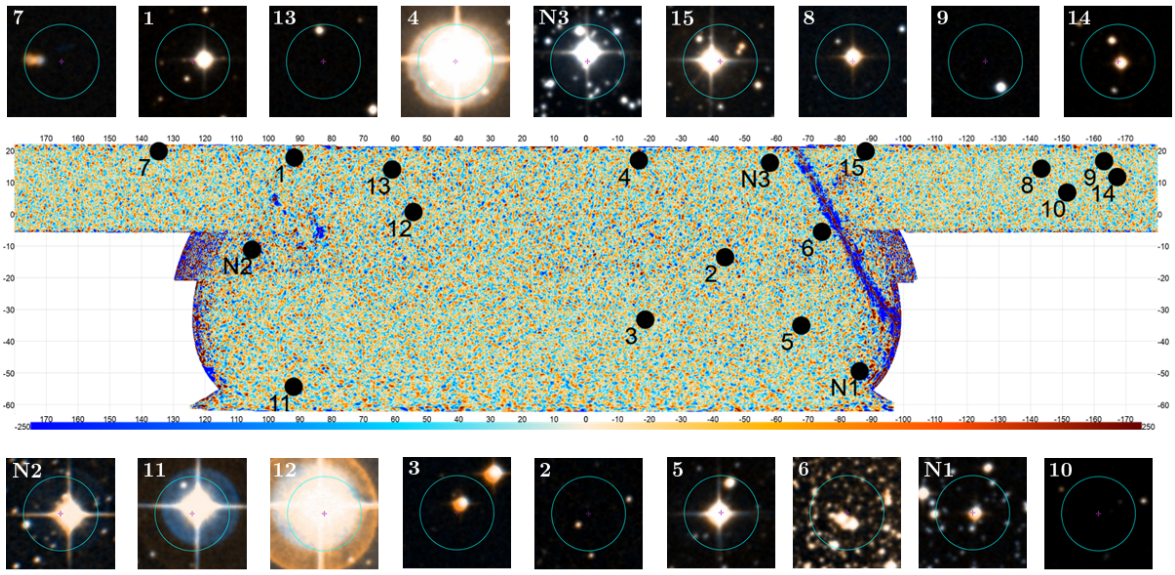

Figure 14: Combined ACT data from 2007–2019 overlayed with the transient positions. Images from DSS at each location, indicated by a in the center of each image, are also shown with a one arcminute contour plotted for scale. The majority of the transient events have bright stellar counterparts seen in the optical.

3.0 Systematic Transient Search of Single Observation Maps

This chapter explores a search for millimeter transients using single observation, or "depth-1" maps from the Atacama Cosmology Telescope. We recover some sources from the three day search and discover many more new transient events, including unprecedented observations of a classical nova. This chapter is based on a publication in preparation for The Astrophysical Journal lead by myself, Yaqiong Li, Sigurd Naess, and the ACT Collaboration. I am the first author on this paper but Yaqiong Li and I share equal contributions.

3.1 Introduction

In this paper we expand upon [47] (see Chapter 2) with newly processed data using an improved pipeline on single-observation, "depth-1 maps" (defined more fully in Section 3.2) rather than 3-day maps. This pipeline searches for "bona fide transients", or objects that nominally do not appear in the map rather than variable sources. The maps used in this analysis will be released publicly in ACT's Data Release 6. The techniques described here will serve as a prototype for a real time transient pipeline for the Simons Observatory Large Aperture Telescope (SO-LAT; [69, 105]), a CMB telescope being built in the Atacama Desert [4]. The SO-LAT will produce daily maps for transient searches [85]. The paper is organized as follows. In Section 3.2 we describe the Atacama Cosmology Telescope and the maps used for the analysis. In Section 3.3 we outline the transient detection pipeline itself. Then, in Section 3.4, we summarize the results and performance of the pipeline. Finally, in Section 3.5 we present conclusions of our findings.

3.2 Data

As part of ACT's Data Release 6 (DR6), we mapped each constant elevation scan into a separate 0.5-arcminute-resolution map, which we call "depth-1 maps", since each pixel has been observed only once by the telescope, in contrast to typical cosmology maps which consist of coadditions of many days' observations. These vary greatly in size, but 1500 square degrees is typical. These maps will be described in detail in a future paper on DR6, but to summarize, they are maximum-likelihood maps using a standard nearest-neighbor pointing matrix. To save computing resources we stopped the conjugate gradients solution process after 100 iterations, which suppresses power on scales $\gtrsim 10'$, or, in spherical harmonic space, on multipoles $\ell \lesssim 1000$. These scales are irrelevant for the point source-like events we consider in this study.

The maps are then matched filtered to optimize point source detection. Each depth-1 map is also accompanied by a co-sampled time map containing information about when each sky pixel was observed by the array.

3.3 Methodology

3.3.1 Detection Pipeline

Before analyzing each map, we mask the Galactic plane and areas of the map within ten pixels (about 5 arcminutes) of the edge. The edge of the map is where the telescope changes direction in the scan which can cause noise fluctuations in map space. We place a 5 arcminute radius mask around ACT sources with average fluxes[1] greater than one sigma (see Table 7). These are typically AGN and dusty star-forming galaxies. We also mask map areas within 50 arcminutes of planets and map areas within 0.5 deg of blazar 3C 454.3. These bright sources have ringing effects associated with them so large areas of the map around them must be masked. The masks used for this paper are summarized in Table 8.

[1]Calculated from night data taken from 2008 to 2022.

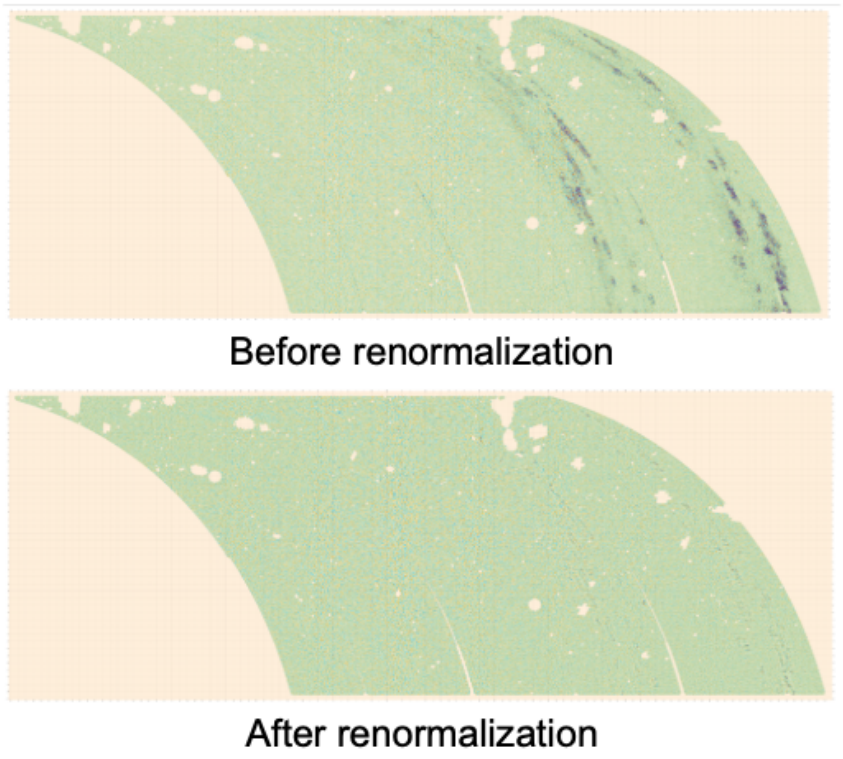

Figure 15: Example S/N maps before and after renormalization, plotted in linear color scale from -5 to +5. There are false signals showing as high-S/N patches on the original matched filtered maps due to imprecise noise modelling. We cut the maps into tiles and apply a renomalization factor so that the mean of each tile's S/N square is corrected to unity.

frequency	typical detection level [mJy]	flux limit [mJy]
f090	143	30
f150	269	50
f220	443	90

Table 7: We mask sources in the depth-1 maps which are greater than one sigma in each map. We use this flux limit rather than masking all sources so that we will detect transients from known sources which are nominally not detected in a depth-1 map. In this table we give the typical detection level and the flux limit of masked sources for each frequency.

mask	radius	percent of pixels cut
Galaxy	–	6.7
edge	10 pixels	1.6
source catalog	5 arcminutes	0.34
planets	50 arcminutes	0.004
blazar 3C 454.3	30 arcminutes	0.003
combined	–	8.4

Table 8: The percent of pixels of all depth-1 maps cut by each type of mask. The Galaxy mask masks the Galactic plane, the edge cut masks pixels within 10 pixels of the edge. The source cut masks all pixels within 5 arcminute of any source above our flux limit in the ACT source catalog. The planets mask cuts pixels within 50 arcminutes of Venus. Mars, Jupiter, Saturn, Uranus, or Neptune. The blazar cut masks sources within 30 arcminutes of the bright blazar 3C 454.3 which is not in the ACT source catalog. We also provide the percentage of pixels cut by all the masks combined. Note that there may be some overlap between masks.

After masking the data, we run a matched filter designed to optimize signal-to-noise on point sources in the map. It is therefore necessary to provide an accurate estimation of the noise level and to filter out other signals that are not point sources. In ideal situations, after applying a matched filter, the map's S/N is approximately a normal distribution (i.e. the square of S/N is expected to be one) when point sources are not dominating. However, noise models for the existing matched filtered depth-1 maps described in Section 3.2 are meant for analysis on larger spatial scales rather than beam-sized sources and some maps show localized enhanced noise along the scanning direction. On these maps, the mean of S/N square for the entire map is still approximately one but there are localized high or low S/N patterns with size of a few arcminues. Possible causes for these effects include uneven scan coverage due to low hit counts and temporary failure of calibration [47]. These problems arise because the original method of modelling U based on the entire map is no longer precise since it underestimates the S/N in high quality regions and overestimate S/N in poor data quality regions. Therefore, before we perform source detection, we apply a renormalization step on the matched filtered S/N maps to work with small scales to compensate the difference in noise behavior across the map (shown in Figure 15). Each S/N map is split into approximately 0.5° by 0.5° tiles along the scanning direction of the telescope and corrected such that the mean of each tile is unity. The tile size is chosen to be small enough to be representative of small scales (10 to 20 times of the beam sizes), but large enough so that the computation can be done quickly. To avoid including the signals from transients or other point sources, we calculate the normalization factor by dividing the median of S/N square in each tile by the median value of the square of a normal distribution value with $\sigma = 1$.

Once the maps are renormalized, we perform our point source detection in a similar way to [47]. First, we find any pixels with S/N greater than 5 and then use the center of mass evaluated by the flux of these pixels to obtain a position measurement.

Even after S/N renormalization, there are still many spurious detections since the original noise model of the matched filter failed to capture the localized noise pattern. We re-apply a matched filter around each candidate to correct for this. First, we cut a 1° by 1° thumbnail from the corresponding depth-1 unfiltered temperature map centered around the candidate's position. We then mask off the center area and any existing point source in the thumbnail,

and re-apply a matched filter, using the power spectrum of the masked thumbnail's signal to model the noise. After that, we repeat the source detection process on the matched filtered thumbnail. Detections which still have a S/N$>$ 5 survive this cut.

Finally, when matching candidate sources in two or more maps, we require the candidate source positions to agree to better than 1.5 arcminutes. We choose this radius to be a little larger than the beamsize as many some of the depth-1 maps contain inconsistent pointing information. Objects that appear in only one detector array are likely to be artifacts from glitches, so we require each candidate to appear in at least two arrays. We use a large crossmatching radius because some of the depth-1 maps have poor pointing and sources may be shifted.

Even with all of these cuts applied, we still detect many data artifacts from a single depth-1 map in pa5-f150. The origin of these artifacts is unknown but since the data represent one night of observations it is likely due to poor observing conditions. We cut this map from our analysis because it represents a small fraction of our data. For example, this is one out of 5474 maps from pa5-f150, or 0.06% of the cumulative area of maps from this band. We only detect transients in 29 depth-1 pa5-f150 maps, so there is about a 0.5% chance this cut map contains a real transient. With this map not included in the sample, there are 524 candidate detections across the entire dataset.

3.3.2 Candidate Verification

We implement an additional cut on the remaining transients that requires the candidate not be within 3 arcminutes of a known bright source. These candidates survived the initial source masking as the pointing is shifted in some of the depth-1 maps. Some bright point sources may have a ringing effect giving rise to false detections. This step cuts 112 out of the 524 detections.

Many of the remaining candidates are coincident with asteroids. These objects are treated in [66] so we cut them here using Astroquery's Skybot package [29]. Any candidate within 1.5 arcminutes of asteroids with a maximum V-band magnitude of 15 are cut. This cuts 358 out of the remaining 412 candidates.

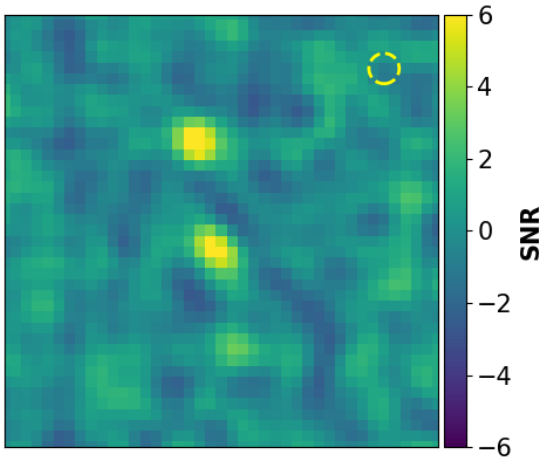

Figure 16: Example of a 20'x20' map of an artifact that passes all cuts and is manually cut from the analysis. This is a signal to noise plot made from a portion of a depth-1 map from array pa4 of a frequency of 150 GHz. For comparison, the dashed circle on the upper right corner shows the 150 GHz beam size. If these sources are real transients, this would mean two point sources separated by several arcminutes on the sky have a large rise in flux at the same time. The much more likely scenario is these are artifacts and not real transients.

The remaining transients are confirmed visually using a diagnostic plot in which maps from each band are plotted sequentially. A transient will not typically appear in the maps and will look like a point source when detected by the pipeline. We find six artifacts that are cut from the transient list using this method. Examples of these artifacts are shown in Figure 16. In this instance, there are two point sources separated by several arcminutes appearing to brighten at the same time, a phenomenon much more likely to be caused by an artifact in the data than a real transient event. The source of these artifacts is unknown but they may be caused by glitches in the time stream due to cosmic rays or atmospheric variations. We also cut a detection which is clearly a variable source at RA 9.603 ± 6 and DEC -41.870 ± 6. This object is a part of the ACT source flux catalog (ACT-S J0038.4-4152, RA: 9.60656 DEC: -41.87096) but the mean flux was low enough to not be cut by the source masking step. Figure 17 shows the light curve of the event, confirming this is a variable source and not a transient. There are no obvious counterparts to this source but the closest match from NED is WISEA J003825.68-415218.8 which is 3.72 arcseconds away. Curiously, the average flux at this location is measured to be higher in the depth-1 maps than in the ACT source catalog which uses the coadded maps to measure the flux. For instance, the average flux in f090 is 64.6 ± 42mJy whereas in the source catalog it is 25.75 ± 0.85mJy. The source appears to be much more variable in the depth-1 maps. After this final cut, there are 45 remaining detections corresponding to 34 independent events.

Each step in the pipeline is summarized in Table 9. We also count how many ACT sources with a measured signal-to-noise ratio within each depth-1 map larger than ten are cut from the matched filter step and the crossmatching step in Table 10. This test is an indicator of how many real transients survive each cut as they are expected to look like point sources in our maps.

3.4 Results

After all cuts are applied there are 45 detections at 27 unique locations. Of the 45 detections there are 34 unique transient events. The events are summarized in Table 11 and

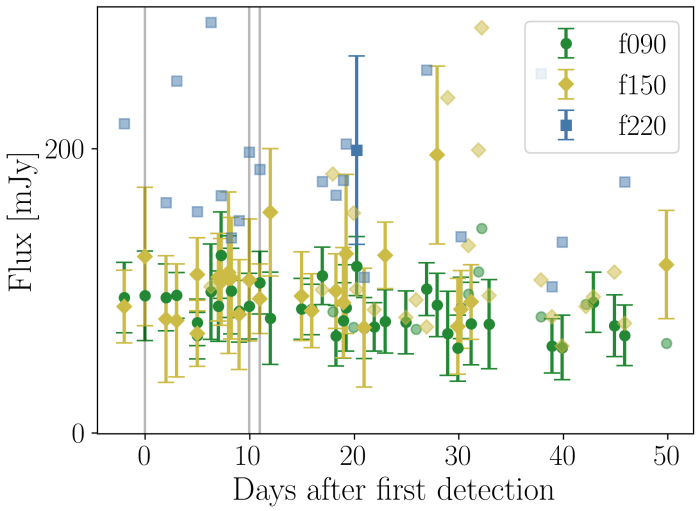

Figure 17: Event (RA: 9.063 ± 6, DEC: -41.870 ± 6) detected by our transient pipeline but cut from the analysis since it is clearly a variable source rather than a transient event. This figure shows the light curve of this event. The grey vertical lines indicate where this source is detected by the pipeline. Note the y-axis is zoomed in for clarity and there are many flux upper limits from f220 which are above the plots y-axis limit.

	Init.	MF	CM	AS	PS	MA	Rem.
pa4-f220	201682	150115	51290	265	0	3	9
pa4-f150	113611	95025	18268	240	52	3	23
pa5-f150	71963	58266	13249	339	77	3	29
pa5-f090	84046	75314	8454	206	23	7	42
pa6-f150	38723	33918	4574	161	53	1	16
pa6-f090	59375	56107	3123	94	26	2	23

Table 9: Summary of candidate cuts. We quote the total number of candidates detected in all the depth-1 maps, the number of candidates that are cut at each step, and the number of remaining candidates. Init. and Rem. refer to the initial and remaining candidates respectively. MF, CM, AS, PS, and MA refer to the number of candidates cut by the matched filter, array crossmatching, asteroid crossmatching, post point source cutting, and manual cutting respectively.The post point source cut removes constant sources which are flagged as transients due to pointing errors within the map.

	N Sources	MF	CM	Total
pa4-f220	10349	1.0%	2.3%	3.2%
pa4-f150	40892	2.5%	2.0%	4.5%
pa5-f150	71457	0.7%	7.1%	7.7%
pa5-f090	146357	1.0%	19.7%	20.7%
pa6-f150	45193	8.3%	4.6%	12.9%
pa6-f090	95223	9.0%	7.2%	16.2%

Table 10: This table summarizes the results of testing the transient pipeline by analyzing sources with an S/N greater than ten. We present the number of such sources found in all the depth-1 maps (N Sources), the percentage that are cut by applying a matched filter and requiring a S/N greater than 5 (MF), and by crossmatching across arrays (CM). We also give the combined number of detections cut by either step (Total).

Table 12. We also include 10 arcminute by 10 arcminute cutouts from sequential depth-1 maps centered on each event to further illustrate the transient nature of these objects. Each object is clearly missing from the map before detection and then either remains, disappears for the rest of observations, or disappears and then reappears again at a later time. It is worth noting that in many cases the transients do not appear to flare in the f220 band. This is most likely because this band is nosier compared to f150 and f090 due to the atmosphere and thus the flare has a lower signal at this frequency.

We recover 12 out of 21 detections from [47]. We do not find any of the four detections that did not look like real transients (events 2, 9, 10, and 13), indicating that they are indeed false detections. Three of the events from [47], J060702+174157, J190222-53610, and J070038-111436, were masked in the depth-1 analysis as a different Galactic dust mask was used. One event, J060757-542626 is too dim to be detected in the depth-1 maps. Although we detect J225302+165027 b, J225302+165027 a is only seen in one array within the depth-1 maps (array 5), so it is cut from the analysis.

We search for counterparts for each transient using the SIMBAD[2] database [96]. Since the SIMBAD database mostly includes nearby bright stars, we calculate the probability of a chance association (p-value) by finding the local density of Gaia stars [26] with the counterpart's magnitude or lower. For the events with Gaia counterparts (all but Event 26), we use the Gaia position to calculate the separation between the candidate and the counterpart. The results are summarized in Table 13.

3.4.1 Light Curves

We present light curves from the depth-1 maps in Figure 19 and Figure 21. A calibration factor and uncertainty from *Planck* point sources is applied to these fluxes in all but the f150-pa4 band due to subtle cross-correlation issues, as outlined in [5]. Although the calibration factor is not yet published for f220 the calculation is the same. The depth-1 light curve plots show measured detections with a signal to noise ratio of at least three and give upper limits to all other data points. The upper limits are calculated by finding the 95% confidence

[2] `https://simbad.cds.unistra.fr/simbad/`

Ind	Name (ACT−T)	RA (deg)	Dec (deg)	Pos. Acc. (arcsec)
1	J175954+104418	-90.025	10.739	13
2a	J142555+141202	-143.520	14.201	4
2b	J142555+141210	-143.517	14.203	15
3	J203622+121537	-50.908	12.261	11
4	J224459−331530	-18.751	-33.259	9
5a	J225302+165022	-16.740	16.840	4
5b	J225302+165011	-16.739	16.837	20
6a	J051921−72035	79.842	-7.343	8
6b	J051921−72040	79.838	-7.345	15
7	J011636−22950	19.151	-2.497	21
8	J200759+160955	-58.003	16.165	9
9a	J192832−350756	-67.867	-35.132	6
9b	J192832−350756	-67.866	-35.132	7
10	J130046+122233	-164.808	12.376	11
11	J050047−571534	75.199	-57.260	16
12	J085813+194546	134.558	19.763	3
13	J101935+195217	154.898	19.872	14
14a	J130529+124935	-163.626	12.827	7
14b	J130529+124937	-163.628	12.827	13
15a	J033646+03512	54.195	0.587	8
15b	J033647+03522	54.200	0.589	18
15c	J033646+03509	54.195	0.586	16
16	J125045+113329	-167.311	11.558	14
17	J174146+22841	-94.555	2.478	31
18	J181515−492747	-86.184	-49.463	7
19	J180723+194222	-88.152	19.706	16
20	J040941−75325	62.425	-7.890	11
21	J193938−60343	-65.089	-6.062	10
22	J035830−544637	59.628	-54.777	17
23	J165122+05005	-107.158	-0.835	8
24	J173353+165508	-96.529	16.919	25
25	J204746−363544	-48.055	-36.596	17
26	J194951−363519	-62.535	-36.589	6
27	J001309+53532	3.288	5.592	16

Table 11: Catalog of the transients. Each different number occurs at a different position. Transients marked with a letter have multiple events at the same position in the sky. Each event's position error is evaluated as the variance of the coordinates observed by different array-frequency combinations.

interval for the positive part of the Gaussian distribution defined by the measured flux and the error on the flux.

All events except for 22 and 26 are within 2.5 times the position error of flaring stars.

The light curves from the depth-1 maps of these events are shown in Figure 19. Most of these events last less than a day and only include one detection from the depth-1 maps. In addition to these light curves we provide high resolution light curves made by binning detectors in each array into four groups allowing us to study minute-scale flux deviations (Figure 20).

In addition to the stellar flares, we detect two transients which cannot be reasonably associated with Gaia stars (Events 22 and 26). Their light curves are shown in Figure 21. Event 22 is coincident with the classical nova YZ Ret, an optically-bright and well observed nova within our Galaxy. These observations are only the second millimeter observations of a classical nova. This event is discussed in Section 3.5 and will be further analyzed in a future paper. Event 26 is associated the LINER-type AGN 2MASX J19495127-3635239.

3.5 Discussion and Conclusions

3.5.1 Stellar Flares

The transients presented in this paper contribute to a growing list of radio and millimeter stellar flares. There are now several examples of millimeter and radio stellar flares from M-dwarfs [52, 51], RS CVn variables [6, 12], T Tauri stars [10, 57, 80, 53] and more [62, 30, 47, 89]. In Figure 23 (left) we provide a comparison of the luminosities of these events. The events exhibit a wide range of characteristics, indicating there is a large parameter space of millimeter stellar flares. We notably do not detect any T Tauri stars as seen in [10], [57], [80], and [53] which are expected to flare due to interactions with an accretion disk. All other papers listed present flares from K or M stars, but we also detect flares from 6 G-type stars and one ApSi star which are not found in millimeter stellar flare literature.

Since there are many events from [89], we compare the distribution of spectral indices rather than luminosity in Figure 23 (right). The distributions are similar but ACT sees events with a slightly more negative spectral index. The combined distribution hints at a Gaussian centered just above zero indicating that the ACT and SPT stellar flare events are

driven by similar mechanisms. Most of the events have a flat or falling spectrum which is often associated with synchrotron or gyrosynchrotron radiation. Two of the stellar flares, however, have rising spectra (Events 2a and 18). In the case of 2a, the spectrum flattens with time. It is possible that this is an indicator of different classes of stellar flares in M-type stars but given the single peak in Figure 23, it is more likely these are similar events with a wide distribution in intrinsic properties.

Further analysis of these events must be done to uncover the mechanism behind these flares which is beyond the scope of this paper. All of the stellar counterparts to the transient events we observe correspond to known magnetically active stellar types and may have similar emission mechanisms. Flares from non-thermal electrons typically occur due to optically thin gyrosynchrotron emission [12, 51]. It has been proposed that bright stellar flares such as these could be driven by "elementary eruptive phenomenon" (EEP) which involve the combination of energy from many heated flare loops [59, 51].

We also note that many of the stellar flares are located close to the galactic plane, as shown in Figure 22. This figure shows a histogram of the galactic latitude of each stellar flare at a unique location. Although the number of stellar flares is too small to make definitive conclusions regarding this statistic, there appears to be a small over-density of flares close to the galactic plane ($l = 0$), indicating there is a subset of flares that may be bright and far away on average.

In [89] they detect a factor of ten more transients in their search of SPT data. As described in [47], SPT is more efficient at transient detection than ACT as the map noise levels are much lower at $\sim 8mJy$. Also, due to SPT's smaller survey area, each location in the sky is viewed with a more regular cadence. However, the pipeline presented in this paper has a similar efficiency to [89]. For instance, the SPT pipeline observes simulated 24-hour transients with an efficiency of $\sim 80\%$. In its best performing band, pa4-f220, the ACT pipeline detects sources with a signal to noise of 5 or greater with an efficiency of 89%. The biggest advantage to the ACT pipeline compared to the SPT pipeline is its automation. Whereas many of the transients are filtered "by-eye" in [89], only nine detections are cut this way in this analysis.

3.5.2 Other Transients

There are very few submillimeter and millimeter observations of classical novae. [38] observed Nova Cygni 1992 in wavelengths ranging from 0.42–2mm at 66, 104, 224, 234, 357 and 358 days after the outburst, finding their data to be consistent with free-free emission from an optically thick nova but inconsistent with canonical radio models. The remnant of Nova V5668 Sgr (2015) was observed in millimeter frequencies by ALMA [21]. These observations resolved the structure of the nova but were taken years after the actual explosion. The observations from Event 22 presented in this paper associated with YZ Ret are therefore only the second millimeter observations of a classical novae taken during the outburst.

The classical nova YZ Ret is a well studied object with several X-ray and optical observations. The nova was first discovered on 2020 July 15.590 UT [95]. This discovery is particularly notable because it is the first nova in which the X-ray flash phase is observed before it was detected in the optical [44]. Our observations are coincident with X-ray observations which occur about sixty days after the X-ray flash [86, 87]. These observations are associated with the supersoft X-ray source (SSS) phase in which optically thick winds stop and X-ray emission is allowed to escape [31]. This emission is expected to follow a blackbody [87] and although we indeed measure a spectral index value consistent with thermal emission at the peak of the event, the spectrum of our millimeter observations flatten over time. We are preparing a paper to explore this discrepancy in more detail.

Event 26, which is associated with an AGN, is reminiscent of the two extragalactic events found by SPT in [30]. Those events were also longer in duration [60] than a stellar flare and are consistent with bright flares from AGN. Curiously, these events have positive spectra that flatten over time (consistent with a newly formed jet) whereas we measure a falling spectrum throughout the flare.

Ind	Peak Flux (mJy)			Mean Flux (mJy)			Time			α
	f220	f150	f090	f220	f150	f090	Peak (UTC)	Rise	Fall	
1	274±86	186±56	145±21	5±3	1±1	6±2	2017-08-05 03:26:35	<1 day	<2 day	0.9±0.3
2a	-	476±100	312±39	-2±2	2±1	6±1	2017-09-17 16:54:14	>19 hour	>1 day	1.0±0.6
2b	424±81	499±47	545±25	0±2	2±1	5±1	2018-11-21 13:09:28	≫5 min	>1 day	-0.4±0.1
3	-	143±62	181±36	-1±3	3±1	5±2	2017-10-08 02:26:16	≫4 min	>1 day	-0.3±0.7
4	207±52	182±40	240±22	5±2	4±1	9±1	2017-10-08 22:19:15	≫4 min	>23 hour	-0.7±0.2
5a	-	139±69	218±29	5±3	8±1	19±2	2017-11-15 0:47:40	≫5 min	≫5 min	-1.6±0.7
5b	-	161±57	222±31	4±3	7±1	21±2	2019-06-06 08:22:39	∼5 min	≫5 min	-0.9±0.4
6a	-	172±51	198±40	8±4	4±2	13±3	2017-11-24 02:53:11	>5 day	<2 day	-0.9±0.7
6b	-	181±55	231±42	8±4	4±2	14±3	2018-10-21 10:48:30	>3 min	<8 day	-1.6±0.6
7	-	159±40	178±42	0±5	0±2	-2±3	2018-05-31 10:37:35	<2 day	≫4 min	-0.7±0.7
8	208±64	300±38	381±30	-3±3	3±1	15±2	2018-09-11 23:43:42	≫6 min	>1 day	-0.6±0.2
9a	2307±222	2228±109	1741±48	5±4	20±1	38±3	2018-10-04 02:19:22	>1 day	≫4 min	0.5±0.1
9b	545±79	604±69	523±35	5±4	12±1	38±3	2019-08-10 23:21:59	≫4 min	>1 day	0.2±0.1
10	-	104±23	115±25	-1±2	0±5	1±1	2018-10-25 12:50:17	∼5 min	<19 hour	-0.7±0.6
11	-	148±50	145±31	0±3	2±1	0±2	2018-11-08 09:06:50	∼5 min	>10 min	0.3±0.4
12	-	206±23	301±11	3±2	0±1	2±1	2018-11-15 10:21:42	∼5 min	≫6 min	-1.0±0.1
13	144±40	176±31	198±13	0±2	0(1)	4±1	2018-12-21 09:19:05	>1 day	>21 hour	-0.3±0.2
14a	-	187±37	129±29	5±2	1±1	6±1	2019-03-13 08:38:52	<2 day	>6 day	0.3±0.5
14b	-	126±34	122±28	4±2	1±1	6±1	2019-08-02 19:18:16	>5 min	>5 day	-0.3±0.5
15a	-	262±62	498±29	11±4	12±1	32±3	2019-08-10 13:35:32	<2 day	>4 day	-1.5±0.3
15b	-	124±51	174±40	10±4	11±1	30±3	2019-09-26 05:11:56	>2 day	≫4 min	-1.6±0.7
15c	-	304±61	599±27	12±4	12±1	32±3	2021-09-29 10:19:17	≫4 min	>5 day	-1.6±0.2
16	-	184±60	223±43	-3±2	2±1	5±1	2019-09-17 15:39:05	>4 min	>4 min	-0.9±0.5
17	-	139±41	151±34	-1±4	2±1	5±3	2019-10-26 16:57:32	<23 hour	<23 hour	-0.6±0.5
18	-	699±47	435±32	-2±6	6±2	16±5	2019-11-08 22:27:58	∼10 min	≫4 min	1.1±0.1
19	-	104±32	159±35	0±2	3±1	5±2	2019-11-13 18:12:29	<5 day	<12 day	-2.7±1.4
20	-	136±61	183±43	3±4	4±2	18±3	2019-12-07 00:41:54	≫4 min	≫4 min	-0.8±0.6
21	709±93	597±83	340±30	17±6	3±2	9±4	2020-06-18 09:20:21	<5 day	<5 day	1.0±0.2
22	195±62	210±46	128±22	13±3	12±1	18±2	2020-09-05 05:55:29	>10 day	∼25 day	0.7±0.3
23	346±60	637±52	680±25	-1±3	2±1	11±2	2020-09-06 19:44:50	<18 hour	>23 hour	-0.4±0.1
24	676±93	1005±52	956±22	-1±2	1±1	0±2	2020-10-17 18:47:17	∼6 min	>3 hour	0±0.1
25	-	401±87	-	2±4	3±1	5±3	2020-11-13 17:59:00	<1 day	<3 day	-0.2±1.1
26	-	201±57	215±25	13±4	22±1	50±3	2021-05-19 05:09:51	∼20 day	-	-0.3±0.4
27	-	205±68	151±28	2±4	0±1	-2±3	2022-05-21 10:00:08	<4 day	<3 day	0.5±0.4

Table 12: Properties for all transients. We provide the peak and mean fluxes of each frequency. If a source is detected by more than one array in a given frequency band, we cite a weighted average. The peak time is defined as the time of the maximum flux in the f090 frequency band. The mean flux is calculated from the weighted average flux over all observations. The rise and fall times are evaluated from the candidates' light curves and subarray light curves. The "≫" sign of the candidate's rise and fall time means that we do not see a minute-wise flux density change within the peak scan but there is a >5 day time gap between the peak scan and the adjacent scan. The spectral index α is evaluated by fitting a power law $S_\nu \propto \nu^\alpha$ of frequency ν using flux density data S_ν taken by pa4 and pa5 because these two array observed the candidates at the same time.

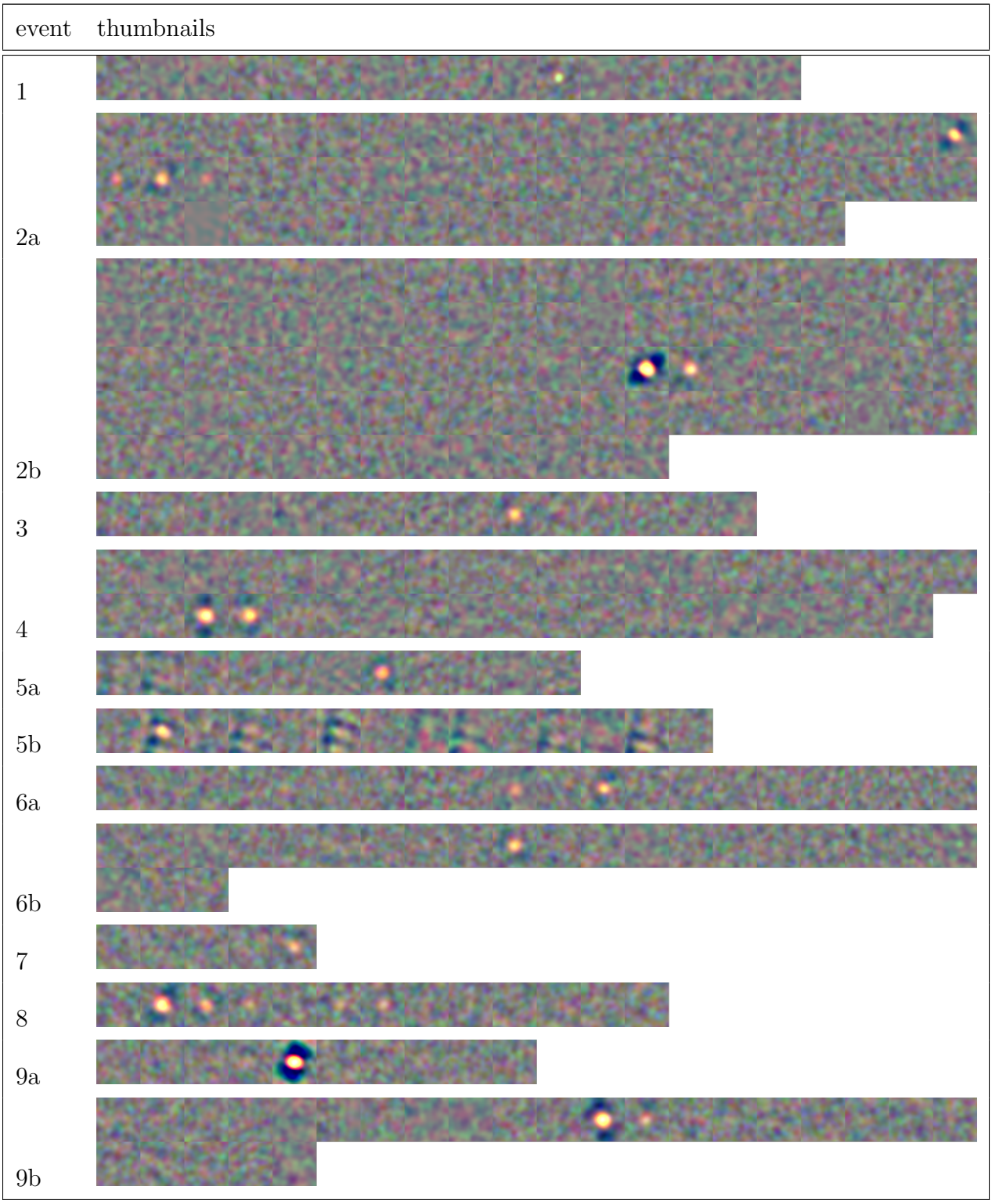

Figure 18: Continued on the next page

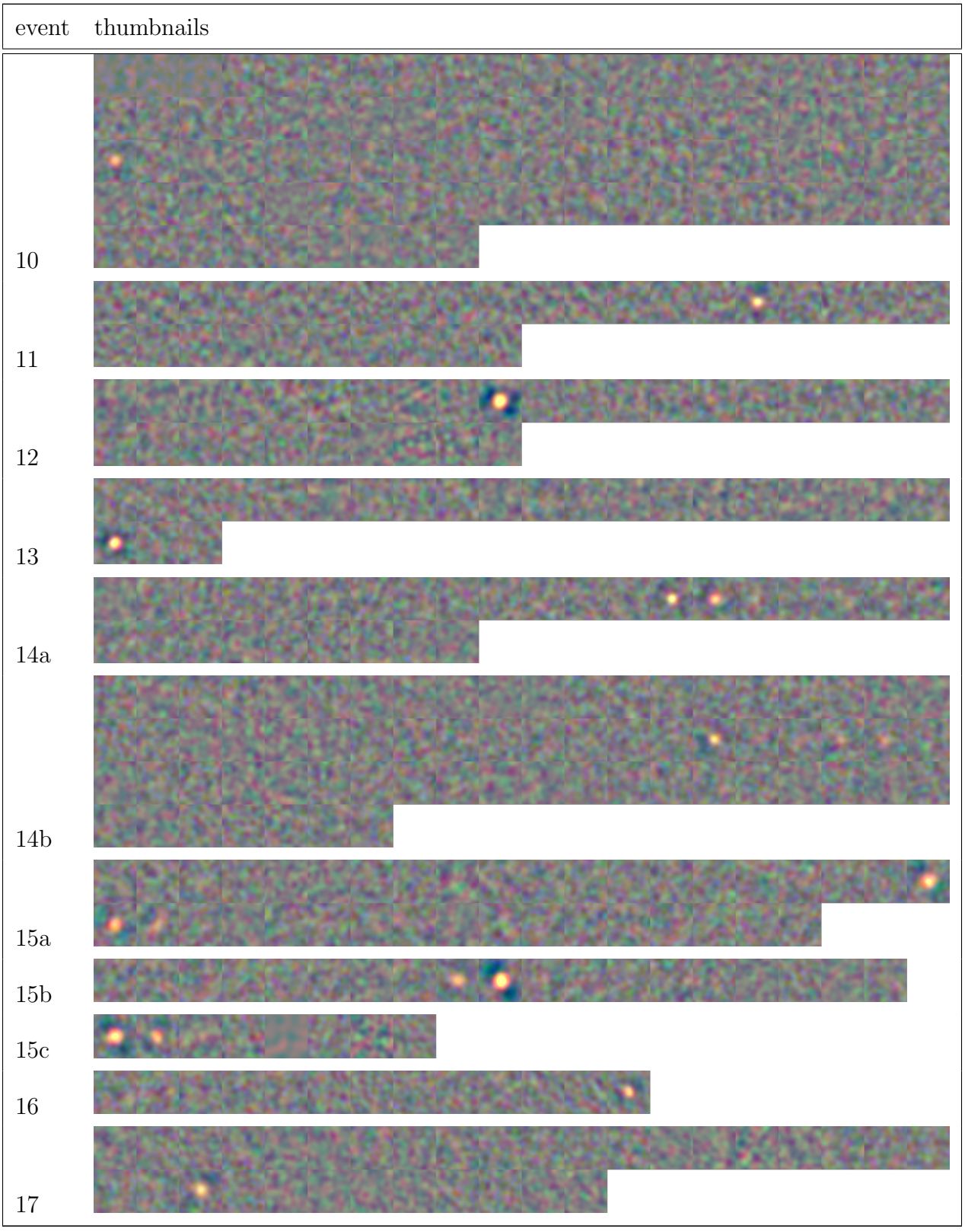

Figure 18: Continued on the next page

Figure 18: Three color, 10 arcminute by 10 arcminute images of candidates from depth-1 maps about one month before and after detection. Red, blue, and green correspond to f090, f150, and f220 respectively. Note the thumbnails are chronological but have inconsistent spacing in time. These plots are included for illustration rather than quantitative analysis.

Name	SIMBAD ID	Type	Mag	Pos Err ()	Sep ()	Chance	Dist (pc)
1	1SWASP J175954.36+104418.9	BYDraV*	10.75	12.65	3.26	8.66e-05	307.78
2a/b	StKM 1−1155	Low-Mass* (M0.0Ve)	10.91	12.10	10.99	2.94e-04	157.92
3	ASAS J203622+1215.3	BYDraV*	9.28	10.56	3.10	2.09e-05	488.40
4	V* TX PsA	Eruptive* (M5IVe)	11.84	12.14	4.01	1.08e-04	20.83
5a/b	V* IM Peg	RSCVnV* (K2III)	5.66	3.59	6.81	8.95e-07	98.37
6a/b	HD 34736	PulsV* (ApSi)	7.79	8.21	18.17	1.46e-04	372.44
7	* 39 Cet	RSCVnV* (G6III:eFe-2)	5.24	21.02	12.21	9.59e-07	74.84
8	HD 191179	SB* (G5)	7.96	9.08	2.62	6.10e-06	219.46
9a/b	HD 182928	RotV* (G8IIIe)	9.37	6.18	2.41	7.28e-06	196.58
10	BD+13 2618	Eruptive* (M0V)	8.91	11.35	2.01	1.56e-06	11.51
11	CD−57 1054	Eruptive* (M0Ve)	9.35	16.24	11.07	1.58e-04	26.87
12	G 9−38B	HighPM* (M7V)	12.49	3.47	3.42	1.54e-04	5.10
13	V* AD Leo	Eruptive* (dM3)	8.21	13.73	7.19	1.20e-05	4.97
14a/b	HD 113714	RSCVnV* (G4V)	9.87	7.17	7.60	5.47e-05	316.38
15a/b/c	HD 22468	RSCVnV* (K2:Vnk)	5.60	6.03	8.71	1.46e-06	29.43
16	UCAC4 508−055499	RSCVnV*	12.43	13.91	8.52	5.22e-04	420.27
17	BD+02 3384	RotV* (G9III)	9.09	30.70	16.81	3.05e-04	395.01
18	2MASS J18151564−4927472	HighPM* (M3)	11.72	7.47	2.90	2.55e-04	61.99
19	HD 347929	RotV* (K0)	9.04	15.87	9.04	1.12e-04	240.74
20	V* EI Eri	RSCVnV* (G3V)	6.95	11.19	17.25	6.31e-05	54.41
21	HD 185510	RSCVnV* (K0III+sdB)	7.81	9.82	7.47	1.62e-05	178.58
22	V* YZ Ret	Nova (sdB?/DA?)	16.26	18.22	1.49	3.08e-04	2644.80
23	V* V2700 Oph	BYDraV*	11.21	7.66	4.27	1.12e-04	312.81
24	V* V1274 Her	BYDraV* (M6V)	12.40	24.77	3.00	2.31e-04	16.42
25	V* BO Mic	BYDraV* (K3V(e))	8.93	17.26	22.27	4.11e-04	51.02
26	2MASX J19495127−3635239	LINER	–	17.98	6.85	–	–
27	V* DV Psc	SB* (K5Ve)	10.21	16.39	7.79	1.10e-04	42.16

Table 13: Transient counterparts from the SIMBAD Database. For repeating events, we take the lower position error to calculate the chance of a random association. For each independent transient position we cite the most likely counterpart from SIMBAD. In the case of binary objects, we cite the object with the lower chance of random association with the transient candidate. The separations are calculated using Gaia positions for all but event 26 where we use the position from SIMBAD. For all events except Event 7 we calculate a density of Gaia stars with the magnitude of the candidate or brighter to determine the chance of a random association (p-value). For Event 7 this is calculated using a 6 degree radius due to a low density of stars with this magnitude or brighter. We also include the spectral type, if known, in the 'type' column.

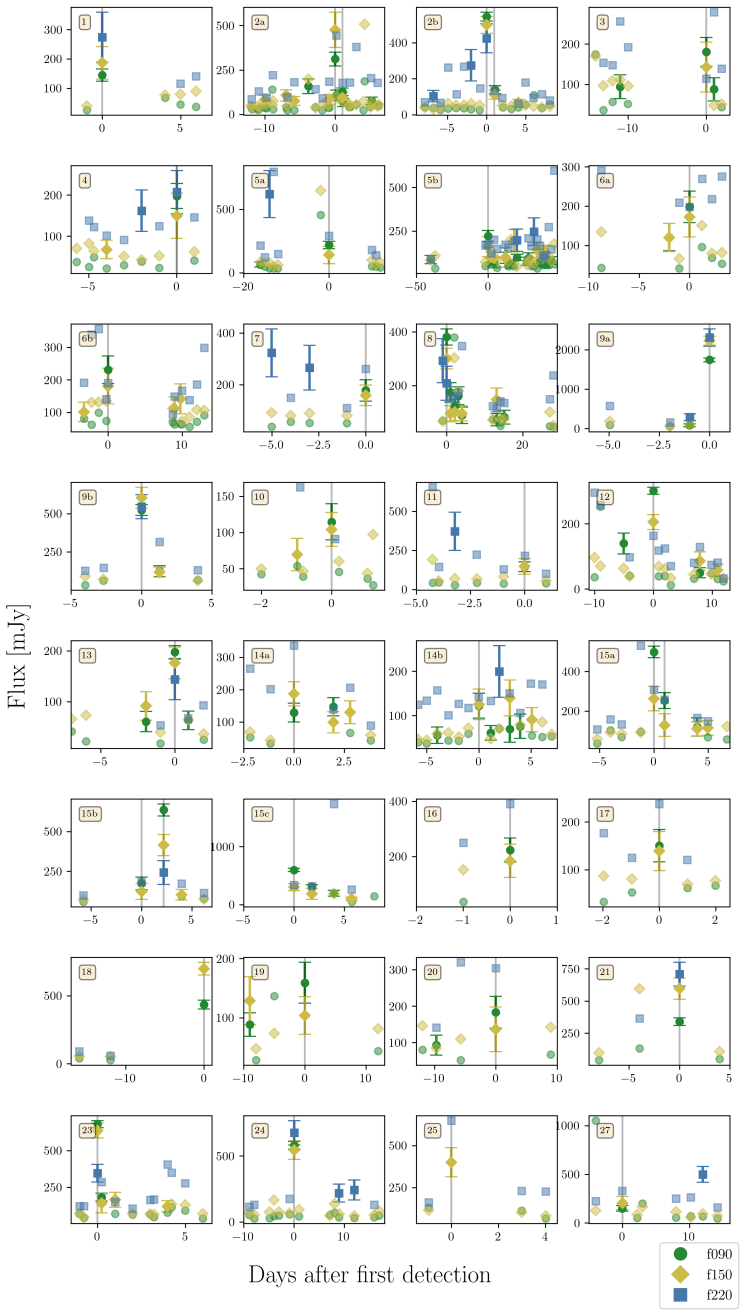

Figure 19: Flux light curves from the depth-1 maps. The flux is measured by detecting a source with a S/N of at least three and within at least two arcminutes of the candidate's position. The data are binned in 0.5 day bins for clarity. Points with errorbars indicate a detection of $SNR > 3$ and points without errorbars show upper flux limits for each frequency. The time of detection from the pipeline is marked by the grey vertical lines. Note the light curves for events 22 and 26 are shown in Figure 21 because they are not associated with stellar flares.

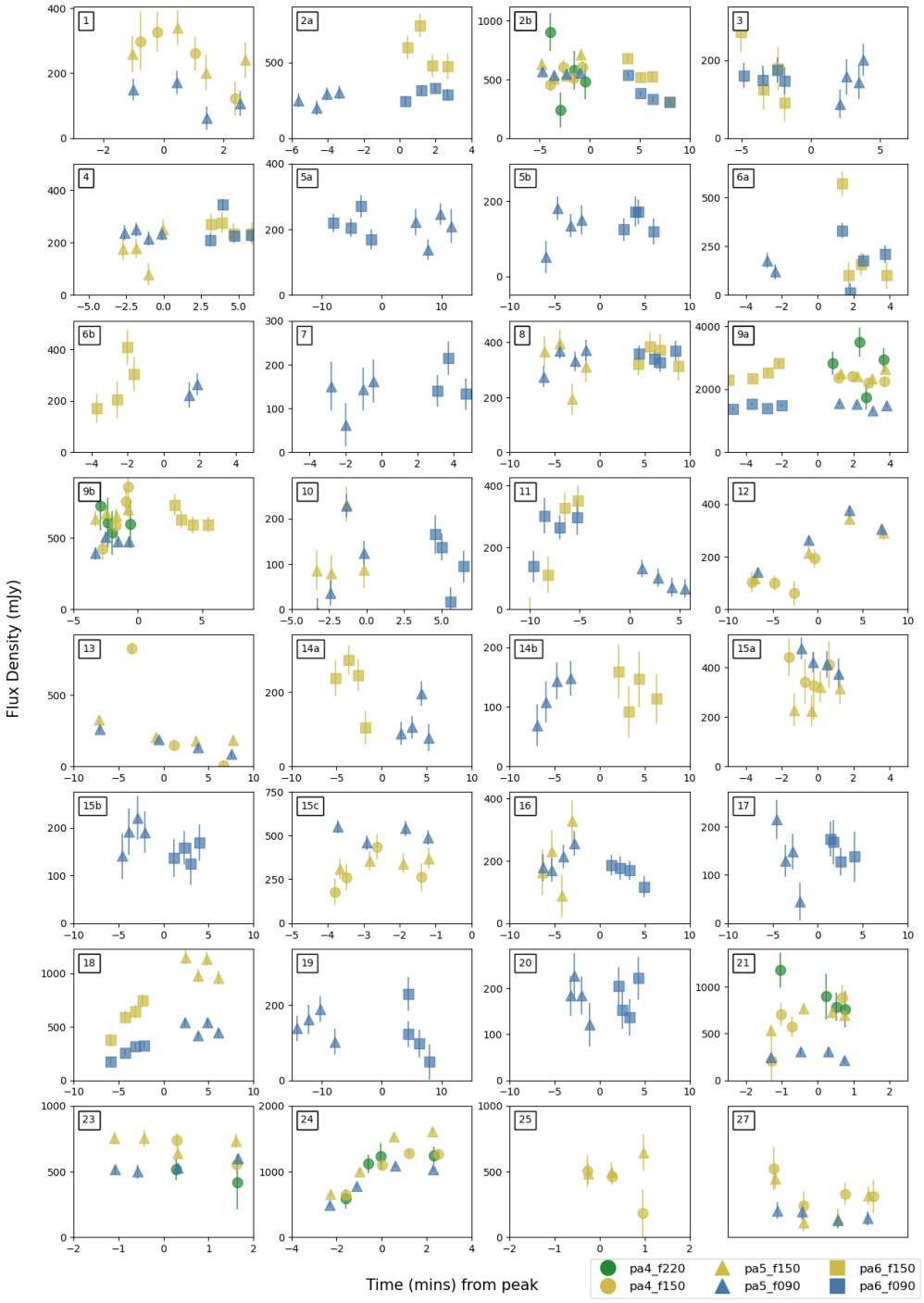

Figure 20: Subarray light curves from forced photometry measurements. Each array is separated into four sections and we evaluate the flux per section as the transient event drift across the whole arrays.

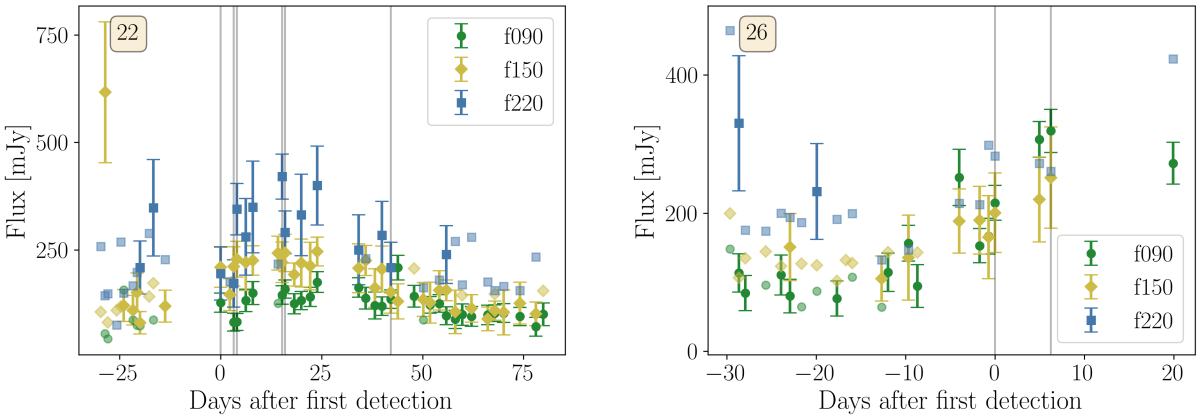

Figure 21: Depth-1 lightcurves for non-stellar-flare events. The x-axis measures the time since the first detection by ACT. The detections from the transient pipeline are marked with grey vertical lines. We present lightcurves from three frequency bands, 90, 150, and 220 GHz shown in blue, yellow, and green respectively. The data are binned into 0.5 day bins for clarity. Points with errorbars indicate a detection of S/N$>$ 3 and points without errorbars show upper flux limits for each frequency. **Left**: Event 22 is coincident with the classical nova YZ Ret. It is detected by ACT about sixty days after initial detection in X-Ray and optical bands [87]. **Right:** Event 26 is associated with the LINER-type AGN 2MASX J19495127-363523. This AGN appears to brighten above baseline variability.

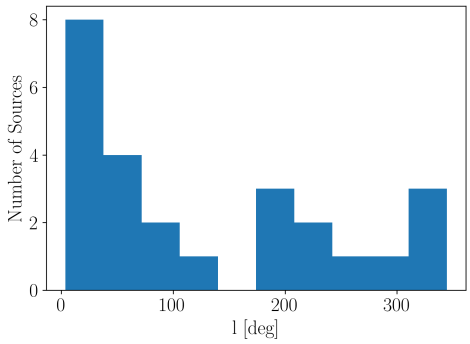

Figure 22: Histogram of the galactic latitude of stellar flares at unique locations. This histogram hints at an over-density close the the galactic plane, however the number of flares is too small to make a broad generalization.

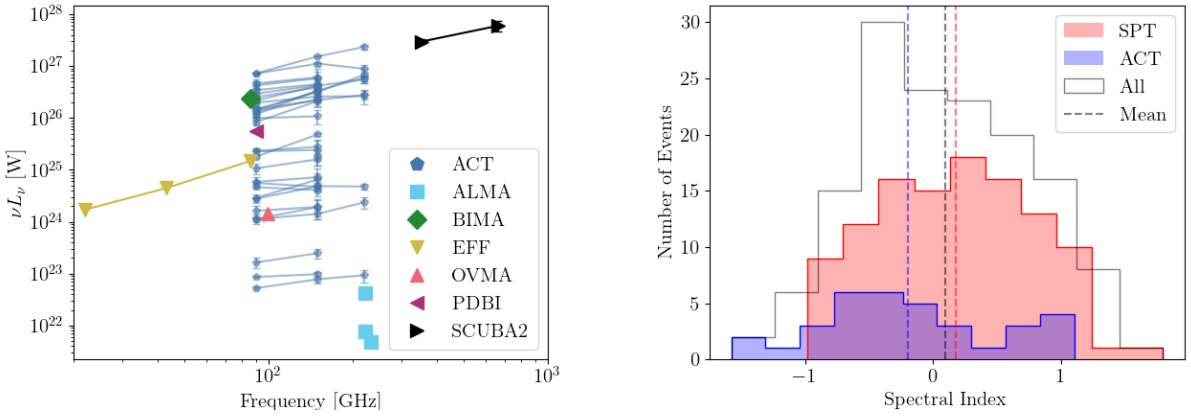

Figure 23: **Left:** Characteristic luminosity in each frequency band for stellar flare events. The luminosity is calculated using the distance to the flare's counterpart listed in Table 13. We include other millimeter flares for comparison from the Atacama Large Millimeter/submillimeter Array (ALMA: [52, 50]), the Owens Valley Millimeter Array (OVMA: [12]), the Berkely-Illinois-Maryland Association (BIMA: [10]), the Nobeyama 45 m telescope (EFF: [92]), the Plateau de Bure Interferometer (PDBI: [57]), and the JCMT Transient Survey (SCUBA2: [53]). **Right:** Histogram of spectral indices for stellar flares from this paper (ACT) and [89] (SPT). We also give the combined distribution. The means of the ACT, SPT, and combined distributions are $\alpha = -0.19, 0.18$, and 0.092 respectively.

4.0 Conclusions

Cosmic microwave background surveys such as the Atacama Cosmology Telescope have unlocked our view into the millimeter transient sky. These experiments are no longer limited to the static universe. In this thesis I present two systematic transient searches of ACT data, uncovering dozens of events including stellar flares, AGN, and an unprecedented classical nova observation. This work serves as a foundation for millimeter transient detection as CMB surveys grow in capability.

This hunt for transients began when three bright events were serendipitously discovered in 3-day maps created to search for Planet 9 [61]. In Chapter 2 I presented a systematic search of these maps [47]. In this search, we uncover 14 stellar flares from magnetically active stars including M-dwarfs, RS CVn variables, and a young stellar object (YSO). This search laid the groundwork for blind transient detection in ACT data by developing methods to filter candidates from relatively noisy maps. This search also detected several signatures from asteroids, illustrating the need to filter out solar system objects in future transient searches.

The 3-day map pipeline is far from perfect. Several chunks of the map are missed by cutting sources with nearby neighbors or with a low pixel hit count. Also, these maps do not detect faster transients whose flux will be washed out in a longer duration map. The largest disadvantage with this pipeline however, is the manual nature of the final cut. Many transients are cut "by eye" and even after all of these filters are applied four ambiguous events remain. These problems are addressed in Chapter 3 where I present an improved systematic transient search of single observation, or "depth-1" maps. These maps are optimized for precise event timing as each pixel corresponds to one observation. The filters themselves are also greatly improved. Rather than cutting out noisy parts of the map, we renormalize the noise to be suited to smaller scales. We also perform a matched filter post source detection on each candidate rather than cutting nearby neighbors. This results in a large reduction of manual cuts which will be important when this pipeline is applied to real-time transient alerts. This pipeline also detects a higher number of transients than the 3-day analysis,

doubling the number of events.

We encounter several types of transients in these analyses but the most common are stellar flares. CMB surveys such as ACT and SPT are building a large database of these types of events. From Figure 23 we realize that although these flares originate from a multitude of systems their mechanisms may be more alike than different. The more events like these we detect, the more statistics we will build to understand stellar flares. In addition to stellar activity, we also encounter a flaring AGN and an unprecedented classical nova observation. As discussed in Chapter 3, this is the most detailed millimeter observation of an active classical nova to date. This finding is a testament to the power of archival datasets and highlights the importance of the continued surveying of the millimeter sky.

We do not find any transient signatures consistent with GRBs. Models predict that over seven years of observations, with an approximately 3-day candence and a map noise level of 17 mJy, ACT will see over ten high energy (meaning a jet Lorentz factor of $\Gamma = 50$) and over two low energy ($\Gamma = 200$) long gamma ray burst reverse shock events with a signal to noise of ten of greater [24]. This prediction assumes all on-axis LGRBs produce observable reverse shock emission. Current targeted observations of LGRBs put an upper limit of RS emission at $\geq 30\%$ of all LGRBs [24]. Therefore, we may not expect to detect any low energy LGRB RS emission with ACT, but conservatively expect to see three high energy events over ACT's entire observation period. These events may be detected but cut from the analysis. A high-sigma detection level of 170 mJy is somewhat optimistic for depth-1 maps (see Table 7). Although such events may be detected in f090, they are less likely to be seen in f150 or f220 and thus may be cut in the crossmatching steps.

Even with these caveats, our non-detection of GRB reverse shock is unexpected. Moreover, targeted searches of GRBs in ACT data also result in non-detections [34]. These results indicate our understanding of GRBs are incomplete because they produce less millimeter emission than models suggest. The most plausible explanation is that a fewer number of GRBs produce observable reverse shock emission than expected.

The work presented here will ultimately lay the groundwork for a real-time transient alert pipeline for SO-LAT. Although ACT is no longer taking data, SO-LAT will begin observing next year. It will have ten times the number of detectors as ACT and a wider field of view,

making it even more optimal for transient searches. We are in the process of using our ACT transient software to develop a fully automatic millimeter transient pipeline for SO-LAT. We will make depth-1 maps of our data after every night of observing and then use our the software pipeline to search for transients. If an event is found, we will begin follow-up observations in radio wavelengths and send an alert to the broader community.

Time domain study is one of the main science goals of CMB-S4, a proposed next generation CMB survey. Located in the Atacama Desert, the observatory will survey the entire southern sky everyday for up to a decade with 500,000 superconducting detectors [1]. The extremely high sensitivity and regular cadence of this instrument make it an ideal transient detector. Simulations of synchrotron transient events in CMB survey data predict CMB-S4 will detect tens of on-axis GRB forward shock emission and over a hundred GRB reverse shock emission events [24]. As CMB telescopes develop in technology so will the detection of millimeter transients. This thesis cracked open a window into the millimeter transient sky, but this is only the beginning.

Bibliography

[1] Kevork Abazajian, Arwa Abdulghafour, Graeme E. Addison, Peter Adshead, Zeeshan Ahmed, Marco Ajello, Daniel Akerib, Steven W. Allen, David Alonso, Marcelo Alvarez, Mustafa A. Amin, Mandana Amiri, Adam Anderson, Behzad Ansarinejad, Melanie Archipley, Kam S. Arnold, Matt Ashby, Han Aung, Carlo Baccigalupi, Carina Baker, Abhishek Bakshi, Debbie Bard, Denis Barkats, Darcy Barron, Peter S. Barry, James G. Bartlett, Paul Barton, Ritoban Basu Thakur, Nicholas Battaglia, Jim Beall, Rachel Bean, Dominic Beck, Sebastian Belkner, Karim Benabed, Amy N. Bender, Bradford A. Benson, Bobby Besuner, Matthieu Bethermin, Sanah Bhimani, Federico Bianchini, Simon Biquard, Ian Birdwell, Colin A. Bischoff, Lindsey Bleem, Paulina Bocaz, James J. Bock, Sebastian Bocquet, Kimberly K. Boddy, J. Richard Bond, Julian Borrill, Francois R. Bouchet, Thejs Brinckmann, Michael L. Brown, Sean Bryan, Victor Buza, Karen Byrum, Erminia Calabrese, Victoria Calafut, Robert Caldwell, John E. Carlstrom, Julien Carron, Thomas Cecil, Anthony Challinor, Victor Chan, Clarence L. Chang, Scott Chapman, Eric Charles, Eric Chauvin, Cheng Cheng, Grace Chesmore, Kolen Cheung, Yuji Chinone, Jens Chluba, Hsiao-Mei Sherry Cho, Steve Choi, Justin Clancy, Susan Clark, Asantha Cooray, Gabriele Coppi, John Corlett, Will Coulton, Thomas M. Crawford, Abigail Crites, Ari Cukierman, Francis-Yan Cyr-Racine, Wei-Ming Dai, Cail Daley, Eli Dart, Gregorg Daues, Tijmen de Haan, Cosmin Deaconu, Jacques Delabrouille, Greg Derylo, Mark Devlin, Eleonora Di Valentino, Marion Dierickx, Brad Dober, Randy Doriese, Shannon Duff, Daniel Dutcher, Cora Dvorkin, Rolando Dünner, Tarraneh Eftekhari, Joseph Eimer, Hamza El Bouhargani, Tucker Elleflot, Nick Emerson, Josquin Errard, Thomas Essinger-Hileman, Giulio Fabbian, Valentina Fanfani, Alessandro Fasano, Chang Feng, Simone Ferraro, Jeffrey P. Filippini, Raphael Flauger, Brenna Flaugher, Aurelien A. Fraisse, Josef Frisch, Andrei Frolov, Nicholas Galitzki, Patricio A. Gallardo, Silvia Galli, Ken Ganga, Martina Gerbino, Christos Giannakopoulos, Murdock Gilchriese, Vera Gluscevic, Neil Goeckner-Wald, David Goldfinger, Daniel Green, Paul Grimes, Daniel Grin, Evan Grohs, Riccardo Gualtieri, Vic Guarino, Jon E. Gudmundsson, Ian Gullett, Sam Guns, Salman Habib, Gunther Haller, Mark Halpern, Nils W. Halverson, Shaul Hanany, Emma Hand, Kathleen Harrington, Masaya Hasegawa, Matthew Hasselfield, Masashi Hazumi, Katrin Heitmann, Shawn Henderson, Brandon Hensley, Ryan Herbst, Carlos Hervias-Caimapo, J. Colin Hill, Richard Hills, Eric Hivon, Renée Hlozek, Anna Ho, Gil Holder, Matt Hollister, William Holzapfel, John Hood, Selim Hotinli, Alec Hryciuk, Johannes Hubmayr, Kevin M. Huffenberger, Howard Hui, Roberto Ibá nez, Ayodeji Ibitoye, Margaret Ikape, Kent Irwin, Cooper Jacobus, Oliver Jeong, Bradley R. Johnson, Doug Johnstone, William C. Jones, John Joseph, Baptiste Jost, Jae Hwan Kang, Ari Kaplan, Kirit S. Karkare, Nobuhiko Katayama, Reijo Keskitalo, Cesiley King, Theodore Kisner, Matthias Klein, Lloyd Knox, Brian J. Koopman, Arthur Kosowsky, John Kovac, Ely D. Kovetz, Alex Krolewski, Donna Kubik, Steve Kuhlmann, Chao-Lin Kuo, Akito Kusaka, Anne Lähteenmäki, Kenny Lau, Charles R. Lawrence, Adrian T. Lee, Louis Legrand, Matthaeus Leitner, Clément

Leloup, Antony Lewis, Dale Li, Eric Linder, Ioannis Liodakis, Jia Liu, Kevin Long, Thibaut Louis, Marilena Loverde, Lindsay Lowry, Chunyu Lu, Phil Lubin, Yin-Zhe Ma, Thomas Maccarone, Mathew S. Madhavacheril, Felipe Maldonado, Adam Mantz, Gabriela Marques, Frederick Matsuda, Philip Mauskopf, Jared May, Heather McCarrick, Ken McCracken, Jeffrey McMahon, P. Daniel Meerburg, Jean-Baptiste Melin, Felipe Menanteau, Joel Meyers, Marius Millea, Vivian Miranda, Don Mitchell, Joseph Mohr, Lorenzo Moncelsi, Maria Elena Monzani, Magdy Moshed, Tony Mroczkowski, Suvodip Mukherjee, Moritz Münchmeyer, Daisuke Nagai, Chandan Nagarajappa, Johanna Nagy, Toshiya Namikawa, Federico Nati, Tyler Natoli, Simran Nerval, Laura Newburgh, Hogan Nguyen, Erik Nichols, Andrina Nicola, Michael D. Niemack, Brian Nord, Tim Norton, Valentine Novosad, Roger O'Brient, Yuuki Omori, Giorgio Orlando, Benjamin Osherson, Rachel Osten, Stephen Padin, Scott Paine, Bruce Partridge, Sanjaykumar Patil, Don Petravick, Matthew Petroff, Elena Pierpaoli, Mauricio Pilleux, Levon Pogosian, Karthik Prabhu, Clement Pryke, Giuseppe Puglisi, Benjamin Racine, Srinivasan Raghunathan, Alexandra Rahlin, Marco Raveri, Ben Reese, Christian L. Reichardt, Mathieu Remazeilles, Arianna Rizzieri, Graca Rocha, Natalie A. Roe, Kaja Rotermund, Anirban Roy, John E. Ruhl, Joe Saba, Noah Sailer, Maria Salatino, Benjamin Saliwanchik, Leonid Sapozhnikov, Mayuri Sathyanarayana Rao, Lauren Saunders, Emmanuel Schaan, Alessandro Schillaci, Benjamin Schmitt, Douglas Scott, Neelima Sehgal, Sarah Shandera, Blake D. Sherwin, Erik Shirokoff, Corwin Shiu, Sara M. Simon, Baibhav Singari, Anze Slosar, David Spergel, Tyler St. Germaine, Suzanne T. Staggs, Antony A. Stark, Glenn D. Starkman, Bryan Steinbach, Radek Stompor, Chris Stoughton, Aritoki Suzuki, Osamu Tajima, Chris Tandoi, Grant P. Teply, Gregg Thayer, Keith Thompson, Ben Thorne, Peter Timbie, Maurizio Tomasi, Cynthia Trendafilova, Matthieu Tristram, Carole Tucker, Gregory Tucker, Caterina Umiltà, Alexander van Engelen, Joshiwa van Marrewijk, Eve M. Vavagiakis, Clara Vergès, Joaquin D. Vieira, Abigail G. Vieregg, Kasey Wagoner, Benjamin Wallisch, Gensheng Wang, Guo-Jian Wang, Scott Watson, Duncan Watts, Chris Weaver, Lukas Wenzl, Ben Westbrook, Martin White, Nathan Whitehorn, Andrew Wiedlea, Paul Williams, Robert Wilson, Harrison Winch, Edward J. Wollack, W. L. Kimmy Wu, Zhilei Xu, Volodymyr G. Yefremenko, Cyndia Yu, David Zegeye, Jeff Zivick, and Andrea Zonca. Snowmass 2021 cmb-s4 white paper, 2022.

[2] Kevork Abazajian, Graeme Addison, Peter Adshead, Zeeshan Ahmed, Steven W. Allen, David Alonso, Marcelo Alvarez, Adam Anderson, Kam S. Arnold, Carlo Baccigalupi, Kathy Bailey, Denis Barkats, Darcy Barron, Peter S. Barry, James G. Bartlett, Ritoban Basu Thakur, Nicholas Battaglia, Eric Baxter, Rachel Bean, Chris Bebek, Amy N. Bender, Bradford A. Benson, Edo Berger, Sanah Bhimani, Colin A. Bischoff, Lindsey Bleem, Sebastian Bocquet, Kimberly Boddy, Matteo Bonato, J. Richard Bond, Julian Borrill, François R. Bouchet, Michael L. Brown, Sean Bryan, Blakesley Burkhart, Victor Buza, Karen Byrum, Erminia Calabrese, Victoria Calafut, Robert Caldwell, John E. Carlstrom, Julien Carron, Thomas Cecil, Anthony Challinor, Clarence L. Chang, Yuji Chinone, Hsiao-Mei Sherry Cho, Asantha Cooray, Thomas M. Crawford, Abigail Crites, Ari Cukierman, Francis-Yan Cyr-Racine, Tijmen de Haan,

Gianfranco de Zotti, Jacques Delabrouille, Marcel Demarteau, Mark Devlin, Eleonora Di Valentino, Matt Dobbs, Shannon Duff, Adriaan Duivenvoorden, Cora Dvorkin, William Edwards, Joseph Eimer, Josquin Errard, Thomas Essinger-Hileman, Giulio Fabbian, Chang Feng, Simone Ferraro, Jeffrey P. Filippini, Raphael Flauger, Brenna Flaugher, Aurelien A. Fraisse, Andrei Frolov, Nicholas Galitzki, Silvia Galli, Ken Ganga, Martina Gerbino, Murdock Gilchriese, Vera Gluscevic, Daniel Green, Daniel Grin, Evan Grohs, Riccardo Gualtieri, Victor Guarino, Jon E. Gudmundsson, Salman Habib, Gunther Haller, Mark Halpern, Nils W. Halverson, Shaul Hanany, Kathleen Harrington, Masaya Hasegawa, Matthew Hasselfield, Masashi Hazumi, Katrin Heitmann, Shawn Henderson, Jason W. Henning, J. Colin Hill, Renée Hlozek, Gil Holder, William Holzapfel, Johannes Hubmayr, Kevin M. Huffenberger, Michael Huffer, Howard Hui, Kent Irwin, Bradley R. Johnson, Doug Johnstone, William C. Jones, Kirit Karkare, Nobuhiko Katayama, James Kerby, Sarah Kernovsky, Reijo Keskitalo, Theodore Kisner, Lloyd Knox, Arthur Kosowsky, John Kovac, Ely D. Kovetz, Steve Kuhlmann, Chao-lin Kuo, Nadine Kurita, Akito Kusaka, Anne Lahteenmaki, Charles R. Lawrence, Adrian T. Lee, Antony Lewis, Dale Li, Eric Linder, Marilena Loverde, Amy Lowitz, Mathew S. Madhavacheril, Adam Mantz, Frederick Matsuda, Philip Mauskopf, Jeff McMahon, Matthew McQuinn, P. Daniel Meerburg, Jean-Baptiste Melin, Joel Meyers, Marius Millea, Joseph Mohr, Lorenzo Moncelsi, Tony Mroczkowski, Suvodip Mukherjee, Moritz Münchmeyer, Daisuke Nagai, Johanna Nagy, Toshiya Namikawa, Federico Nati, Tyler Natoli, Mattia Negrello, Laura Newburgh, Michael D. Niemack, Haruki Nishino, Martin Nordby, Valentine Novosad, Paul O'Connor, Georges Obied, Stephen Padin, Shivam Pandey, Bruce Partridge, Elena Pierpaoli, Levon Pogosian, Clement Pryke, Giuseppe Puglisi, Benjamin Racine, Srinivasan Raghunathan, Alexandra Rahlin, Srini Rajagopalan, Marco Raveri, Mark Reichanadter, Christian L. Reichardt, Mathieu Remazeilles, Graca Rocha, Natalie A. Roe, Anirban Roy, John Ruhl, Maria Salatino, Benjamin Saliwanchik, Emmanuel Schaan, Alessandro Schillaci, Marcel M. Schmittfull, Douglas Scott, Neelima Sehgal, Sarah Shandera, Christopher Sheehy, Blake D. Sherwin, Erik Shirokoff, Sara M. Simon, Anze Slosar, Rachel Somerville, David Spergel, Suzanne T. Staggs, Antony Stark, Radek Stompor, Kyle T. Story, Chris Stoughton, Aritoki Suzuki, Osamu Tajima, Grant P. Teply, Keith Thompson, Peter Timbie, Maurizio Tomasi, Jesse I. Treu, Matthieu Tristram, Gregory Tucker, Caterina Umiltà, Alexander van Engelen, Joaquin D. Vieira, Abigail G. Vieregg, Mark Vogelsberger, Gensheng Wang, Scott Watson, Martin White, Nathan Whitehorn, Edward J. Wollack, W. L. Kimmy Wu, Zhilei Xu, Siavash Yasini, James Yeck, Ki Won Yoon, Edward Young, and Andrea Zonca. Cmb-s4 science case, reference design, and project plan, 2019.

[3] S. Abdollahi, M. Ackermann, M. Ajello, A. Albert, L. Baldini, J. Ballet, G. Barbiellini, D. Bastieri, J. Becerra Gonzalez, R. Bellazzini, E. Bissaldi, R. D. Blandford, E. D. Bloom, R. Bonino, E. Bottacini, J. Bregeon, P. Bruel, R. Buehler, S. Buson, R. A. Cameron, M. Caragiulo, P. A. Caraveo, E. Cavazzuti, C. Cecchi, A. Chekhtman, C. C. Cheung, G. Chiaro, S. Ciprini, J. Conrad, D. Costantin, F. Costanza, S. Cutini, F. D'Ammando, F. de Palma, A. Desai, R. Desiante, S. W. Digel, N. Di Lalla,

M. Di Mauro, L. Di Venere, B. Donaggio, P. S. Drell, C. Favuzzi, S. J. Fegan, E. C. Ferrara, W. B. Focke, A. Franckowiak, Y. Fukazawa, S. Funk, P. Fusco, F. Gargano, D. Gasparrini, N. Giglietto, M. Giomi, F. Giordano, M. Giroletti, T. Glanzman, D. Green, I. A. Grenier, J. E. Grove, L. Guillemot, S. Guiriec, E. Hays, D. Horan, T. Jogler, G. Jóhannesson, A. S. Johnson, D. Kocevski, M. Kuss, G. La Mura, S. Larsson, L. Latronico, J. Li, F. Longo, F. Loparco, M. N. Lovellette, P. Lubrano, J. D. Magill, S. Maldera, A. Manfreda, M. Mayer, M. N. Mazziotta, P. F. Michelson, W. Mitthumsiri, T. Mizuno, M. E. Monzani, A. Morselli, I. V. Moskalenko, M. Negro, E. Nuss, T. Ohsugi, N. Omodei, M. Orienti, E. Orlando, V. S. Paliya, D. Paneque, J. S. Perkins, M. Persic, M. Pesce-Rollins, V. Petrosian, F. Piron, T. A. Porter, G. Principe, S. Rainò, R. Rando, M. Razzano, S. Razzaque, A. Reimer, O. Reimer, C. Sgrò, D. Simone, E. J. Siskind, F. Spada, G. Spandre, P. Spinelli, L. Stawarz, D. J. Suson, M. Takahashi, K. Tanaka, J. B. Thayer, D. J. Thompson, D. F. Torres, E. Torresi, G. Tosti, E. Troja, G. Vianello, and K. S. Wood. The second catalog of flaring gamma-ray sources from thei /fermi all-sky variability analysis. *The Astrophysical Journal*, 846(1):34, aug 2017.

[4] Peter Ade, James Aguirre, Zeeshan Ahmed, Simone Aiola, Aamir Ali, David Alonso, Marcelo A. Alvarez, Kam Arnold, Peter Ashton, Jason Austermann, Humna Awan, Carlo Baccigalupi, Taylor Baildon, Darcy Barron, Nick Battaglia, Richard Battye, Eric Baxter, Andrew Bazarko, James A. Beall, Rachel Bean, Dominic Beck, Shawn Beckman, Benjamin Beringue, Federico Bianchini, Steven Boada, David Boettger, J. Richard Bond, Julian Borrill, Michael L. Brown, Sarah Marie Bruno, Sean Bryan, Erminia Calabrese, Victoria Calafut, Paolo Calisse, Julien Carron, Anthony Challinor, Grace Chesmore, Yuji Chinone, Jens Chluba, Hsiao-Mei Sherry Cho, Steve Choi, Gabriele Coppi, Nicholas F. Cothard, Kevin Coughlin, Devin Crichton, Kevin D. Crowley, Kevin T. Crowley, Ari Cukierman, John M. D'Ewart, Rolando Dünner, Tijmen de Haan, Mark Devlin, Simon Dicker, Joy Didier, Matt Dobbs, Bradley Dober, Cody J. Duell, Shannon Duff, Adri Duivenvoorden, Jo Dunkley, John Dusatko, Josquin Errard, Giulio Fabbian, Stephen Feeney, Simone Ferraro, Pedro Fluxà , Katherine Freese, Josef C. Frisch, Andrei Frolov, George Fuller, Brittany Fuzia, Nicholas Galitzki, Patricio A. Gallardo, Jose Tomas Galvez Ghersi, Jiansong Gao, Eric Gawiser, Martina Gerbino, Vera Gluscevic, Neil Goeckner-Wald, Joseph Golec, Sam Gordon, Megan Gralla, Daniel Green, Arpi Grigorian, John Groh, Chris Groppi, Yilun Guan, Jon E. Gudmundsson, Dongwon Han, Peter Hargrave, Masaya Hasegawa, Matthew Hasselfield, Makoto Hattori, Victor Haynes, Masashi Hazumi, Yizhou He, Erin Healy, Shawn W. Henderson, Carlos Hervias-Caimapo, Charles A. Hill, J. Colin Hill, Gene Hilton, Matt Hilton, Adam D. Hincks, Gary Hinshaw, Renée Hložek, Shirley Ho, Shuay-Pwu Patty Ho, Logan Howe, Zhiqi Huang, Johannes Hubmayr, Kevin Huffenberger, John P. Hughes, Anna Ijjas, Margaret Ikape, Kent Irwin, Andrew H. Jaffe, Bhuvnesh Jain, Oliver Jeong, Daisuke Kaneko, Ethan D. Karpel, Nobuhiko Katayama, Brian Keating, Sarah S. Kernasovskiy, Reijo Keskitalo, Theodore Kisner, Kenji Kiuchi, Jeff Klein, Kenda Knowles, Brian Koopman, Arthur Kosowsky, Nicoletta Krachmalnicoff, Stephen E. Kuenstner, Chao-Lin Kuo,

Akito Kusaka, Jacob Lashner, Adrian Lee, Eunseong Lee, David Leon, Jason S.-Y. Leung, Antony Lewis, Yaqiong Li, Zack Li, Michele Limon, Eric Linder, Carlos Lopez-Caraballo, Thibaut Louis, Lindsay Lowry, Marius Lungu, Mathew Madhavacheril, Daisy Mak, Felipe Maldonado, Hamdi Mani, Ben Mates, Frederick Matsuda, Loïc Maurin, Phil Mauskopf, Andrew May, Nialh McCallum, Chris McKenney, Jeff McMahon, P. Daniel Meerburg, Joel Meyers, Amber Miller, Mark Mirmelstein, Kavilan Moodley, Moritz Munchmeyer, Charles Munson, Sigurd Naess, Federico Nati, Martin Navaroli, Laura Newburgh, Ho Nam Nguyen, Michael Niemack, Haruki Nishino, John Orlowski-Scherer, Lyman Page, Bruce Partridge, Julien Peloton, Francesca Perrotta, Lucio Piccirillo, Giampaolo Pisano, Davide Poletti, Roberto Puddu, Giuseppe Puglisi, Chris Raum, Christian L. Reichardt, Mathieu Remazeilles, Yoel Rephaeli, Dominik Riechers, Felipe Rojas, Anirban Roy, Sharon Sadeh, Yuki Sakurai, Maria Salatino, Mayuri Sathyanarayana Rao, Emmanuel Schaan, Marcel Schmittfull, Neelima Sehgal, Joseph Seibert, Uros Seljak, Blake Sherwin, Meir Shimon, Carlos Sierra, Jonathan Sievers, Precious Sikhosana, Maximiliano Silva-Feaver, Sara M. Simon, Adrian Sinclair, Praween Siritanasak, Kendrick Smith, Stephen R. Smith, David Spergel, Suzanne T. Staggs, George Stein, Jason R. Stevens, Radek Stompor, Aritoki Suzuki, Osamu Tajima, Satoru Takakura, Grant Teply, Daniel B. Thomas, Ben Thorne, Robert Thornton, Hy Trac, Calvin Tsai, Carole Tucker, Joel Ullom, Sunny Vagnozzi, Alexander van Engelen, Jeff Van Lanen, Daniel D. Van Winkle, Eve M. Vavagiakis, Clara Vergès, Michael Vissers, Kasey Wagoner, Samantha Walker, Jon Ward, Ben Westbrook, Nathan Whitehorn, Jason Williams, Joel Williams, Edward J. Wollack, Zhilei Xu, Byeonghee Yu, Cyndia Yu, Fernando Zago, Hezi Zhang, and Ningfeng Zhu and. The simons observatory: science goals and forecasts. *Journal of Cosmology and Astroparticle Physics*, 2019(02):056–056, feb 2019.

[5] Simone Aiola, Erminia Calabrese, Loïc Maurin, Sigurd Naess, Benjamin L. Schmitt, Maximilian H. Abitbol, Graeme E. Addison, Peter A. R. Ade, David Alonso, Mandana Amiri, Stefania Amodeo, Elio Angile, Jason E. Austermann, Taylor Baildon, Nick Battaglia, James A. Beall, Rachel Bean, Daniel T. Becker, J Richard Bond, Sarah Marie Bruno, Victoria Calafut, Luis E. Campusano, Felipe Carrero, Grace E. Chesmore, Hsiao mei Cho, Steve K. Choi, Susan E. Clark, Nicholas F. Cothard, Devin Crichton, Kevin T. Crowley, Omar Darwish, Rahul Datta, Edward V. Denison, Mark J. Devlin, Cody J. Duell, Shannon M. Duff, Adriaan J. Duivenvoorden, Jo Dunkley, Rolando Dünner, Thomas Essinger-Hileman, Max Fankhanel, Simone Ferraro, Anna E. Fox, Brittany Fuzia, Patricio A. Gallardo, Vera Gluscevic, Joseph E. Golec, Emily Grace, Megan Gralla, Yilun Guan, Kirsten Hall, Mark Halpern, Dongwon Han, Peter Hargrave, Matthew Hasselfield, Jakob M. Helton, Shawn Henderson, Brandon Hensley, J. Colin Hill, Gene C. Hilton, Matt Hilton, Adam D. Hincks, Renée Hložek, Shuay-Pwu Patty Ho, Johannes Hubmayr, Kevin M. Huffenberger, John P. Hughes, Leopoldo Infante, Kent Irwin, Rebecca Jackson, Jeff Klein, Kenda Knowles, Brian Koopman, Arthur Kosowsky, Vincent Lakey, Dale Li, Yaqiong Li, Zack Li, Martine Lokken, Thibaut Louis, Marius Lungu, Amanda MacInnis, Mathew Madhavacheril, Felipe Maldonado, Maya Mallaby-Kay, Danica Marsden, Jeff McMahon,

Felipe Menanteau, Kavilan Moodley, Tim Morton, Toshiya Namikawa, Federico Nati, Laura Newburgh, John P. Nibarger, Andrina Nicola, Michael D. Niemack, Michael R. Nolta, John Orlowski-Sherer, Lyman A. Page, Christine G. Pappas, Bruce Partridge, Phumlani Phakathi, Giampaolo Pisano, Heather Prince, Roberto Puddu, Frank J. Qu, Jesus Rivera, Naomi Robertson, Felipe Rojas, Maria Salatino, Emmanuel Schaan, Alessandro Schillaci, Neelima Sehgal, Blake D. Sherwin, Carlos Sierra, Jon Sievers, Cristobal Sifon, Precious Sikhosana, Sara Simon, David N. Spergel, Suzanne T. Staggs, Jason Stevens, Emilie Storer, Dhaneshwar D. Sunder, Eric R. Switzer, Ben Thorne, Robert Thornton, Hy Trac, Jesse Treu, Carole Tucker, Leila R. Vale, Alexander Van Engelen, Jeff Van Lanen, Eve M. Vavagiakis, Kasey Wagoner, Yuhan Wang, Jonathan T. Ward, Edward J. Wollack, Zhilei Xu, Fernando Zago, and Ningfeng Zhu. The atacama cosmology telescope: Dr4 maps and cosmological parameters. *Journal of Cosmology and Astroparticle Physics*, 2020(12):047, dec 2020.

[6] A. J. Beasley and T. S. Bastian. VLBA Imaging of UX Ari. In J. A. Zensus, G. B. Taylor, and J. M. Wrobel, editors, *IAU Colloq. 164: Radio Emission from Galactic and Extragalactic Compact Sources*, volume 144 of *Astronomical Society of the Pacific Conference Series*, page 321, January 1998.

[7] Edo Berger. Short-duration gamma-ray bursts. *Annual Review of Astronomy and Astrophysics*, 52(1):43–105, Aug 2014.

[8] T. Boch and P. Fernique. Aladin Lite: Embed your Sky in the Browser. In N. Manset and P. Forshay, editors, *Astronomical Data Analysis Software and Systems XXIII*, volume 485 of *Astronomical Society of the Pacific Conference Series*, page 277, May 2014.

[9] John J. Bochanski, Suzanne L. Hawley, Kevin R. Covey, Andrew A. West, I. Neill Reid, David A. Golimowski, and Željko Ivezić. The Luminosity and Mass Functions of Low-mass Stars in the Galactic Disk. II. The Field. , 139(6):2679–2699, June 2010.

[10] Geoffrey C. Bower, Richard L. Plambeck, Alberto Bolatto, Nate McCrady, James R. Graham, Imke de Pater, Michael C. Liu, and Frederick K. Baganoff. A giant outburst at millimeter wavelengths in the orion nebula. *The Astrophysical Journal*, 598(2):1140–1150, dec 2003.

[11] Joe S. Bright, Lauren Rhodes, Wael Farah, Rob Fender, Alexander J. van der Horst, James K. Leung, David R. Williams, Gemma E. Anderson, Pikky Atri, David R. DeBoer, and et al. Precise measurements of self-absorbed rising reverse shock emission from gamma-ray burst 221009a. *Nature Astronomy*, 7(8):986–995, Jun 2023.

[12] Joanna M. Brown and Alexander Brown. A Large Millimeter Flare on the RS CVn Binary σ Geminorum. , 638(1):L37–L40, February 2006.

[13] J. E. Carlstrom, P. A. R. Ade, K. A. Aird, B. A. Benson, L. E. Bleem, S. Busetti, C. L. Chang, E. Chauvin, H.-M. Cho, T. M. Crawford, A. T. Crites, M. A. Dobbs, N. W. Halverson, S. Heimsath, W. L. Holzapfel, J. D. Hrubes, M. Joy, R. Keisler, T. M. Lanting, A. T. Lee, E. M. Leitch, J. Leong, W. Lu, M. Lueker, D. Luong-Van, J. J. McMahon, J. Mehl, S. S. Meyer, J. J. Mohr, T. E. Montroy, S. Padin, T. Plagge, C. Pryke, J. E. Ruhl, K. K. Schaffer, D. Schwan, E. Shirokoff, H. G. Spieler, Z. Staniszewski, A. A. Stark, C. Tucker, K. Vanderlinde, J. D. Vieira, and R. Williamson. The 10 meter south pole telescope. *Publications of the Astronomical Society of the Pacific*, 123(903):568, apr 2011.

[14] CCAT-Prime Collaboration, Manuel Aravena, Jason E. Austermann, Kaustuv Basu, Nicholas Battaglia, Benjamin Beringue, Frank Bertoldi, Frank Bigiel, J. Richard Bond, Patrick C. Breysse, Colton Broughton, Ricardo Bustos, Scott C. Chapman, Maude Charmetant, Steve K. Choi, Dongwoo T. Chung, Susan E. Clark, Nicholas F. Cothard, Abigail T. Crites, Ankur Dev, Kaela Douglas, Cody J. Duell, Rolando Dünner, Haruki Ebina, Jens Erler, Michel Fich, Laura M. Fissel, Simon Foreman, R. G. Freundt, Patricio A. Gallardo, Jiansong Gao, Pablo García, Riccardo Giovanelli, Joseph E. Golec, Christopher E. Groppi, Martha P. Haynes, Douglas Henke, Brandon Hensley, Terry Herter, Ronan Higgins, Renée Hložek, Anthony Huber, Zachary Huber, Johannes Hubmayr, Rebecca Jackson, Douglas Johnstone, Christos Karoumpis, Laura C. Keating, Eiichiro Komatsu, Yaqiong Li, Benjamin Magnelli, Brenda C. Matthews, Philip D. Mauskopf, Jeffrey J. McMahon, P. Daniel Meerburg, Joel Meyers, Vyoma Muralidhara, Norman W. Murray, Michael D. Niemack, Thomas Nikola, Yoko Okada, Roberto Puddu, Dominik A. Riechers, Erik Rosolowsky, Kayla Rossi, Kaja Rotermund, Anirban Roy, Sarah I. Sadavoy, Reinhold Schaaf, Peter Schilke, Douglas Scott, Robert Simon, Adrian K. Sinclair, Gregory R. Sivakoff, Gordon J. Stacey, Amelia M. Stutz, Juergen Stutzki, Mehrnoosh Tahani, Karun Thanjavur, Ralf A. Timmermann, Joel N. Ullom, Alexander van Engelen, Eve M. Vavagiakis, Michael R. Vissers, Jordan D. Wheeler, Simon D. M. White, Yijie Zhu, and Bugao Zou. CCAT-prime Collaboration: Science Goals and Forecasts with Prime-Cam on the Fred Young Submillimeter Telescope. , 264(1):7, January 2023.

[15] Poonam Chandra. Gamma-Ray Bursts: A Radio Perspective. *Advances in Astronomy*, 2016:296781, January 2016.

[16] Roger A. Chevalier and Claes Fransson. Thermal and Non-thermal Emission from Circumstellar Interaction. In Athem W. Alsabti and Paul Murdin, editors, *Handbook of Supernovae*, page 875. 2017.

[17] CHIME/FRB Collaboration, B. C. Andersen, K. M. Bandura, M. Bhardwaj, A. Bij, M. M. Boyce, P. J. Boyle, C. Brar, T. Cassanelli, P. Chawla, T. Chen, J. F. Cliche, A. Cook, D. Cubranic, A. P. Curtin, N. T. Denman, M. Dobbs, F. Q. Dong, M. Fandino, E. Fonseca, B. M. Gaensler, U. Giri, D. C. Good, M. Halpern, A. S. Hill, G. F. Hinshaw, C. Höfer, A. Josephy, J. W. Kania, V. M. Kaspi, T. L. Landecker, C. Leung, D. Z. Li, H. H. Lin, K. W. Masui, R. McKinven, J. Mena-Parra, M. Merryfield, B. W. Meyers, D. Michilli, N. Milutinovic, A. Mirhosseini, M. Münchmeyer, A. Naidu, L. B. Newburgh, C. Ng, C. Patel, U. L. Pen, T. Pinsonneault-Marotte, Z. Pleunis, B. M. Quine, M. Rafiei-Ravandi, M. Rahman, S. M. Ransom, A. Renard, P. Sanghavi, P. Scholz, J. R. Shaw, K. Shin, S. R. Siegel, S. Singh, R. J. Smegal, K. M. Smith, I. H. Stairs, C. M. Tan, S. P. Tendulkar, I. Tretyakov, K. Vanderlinde, H. Wang, D. Wulf, and A. V. Zwaniga. A bright millisecond-duration radio burst from a Galactic magnetar. , 587(7832):54–58, November 2020.

[18] S. K. Choi, J. Austermann, J. A. Beall, K. T. Crowley, R. Datta, S. M. Duff, P. A. Gallardo, S. P. Ho, J. Hubmayr, B. J. Koopman, Y. Li, F. Nati, M. D. Niemack, L. A. Page, M. Salatino, S. M. Simon, S. T. Staggs, J. Stevens, J. Ullom, and E. J. Wollack. Characterization of the mid-frequency arrays for advanced ACTPol. *Journal of Low Temperature Physics*, 193(3-4):267–275, jun 2018.

[19] Laura Chomiuk, Brian D. Metzger, and Ken J. Shen. New insights into classical novae. *Annual Review of Astronomy and Astrophysics*, 59(Volume 59, 2021):391–444, 2021.

[20] James J. Condon and Scott M. Ransom. *Essential Radio Astronomy.* Princeton University Press, sch - school edition edition, 2016.

[21] Marcos P. Diaz, Zulema Abraham, Valério A. R. M. Ribeiro, Pedro P. B. Beaklini, and Larissa Takeda. The structure of a recent nova shell as observed by ALMA. , 480(1):L54–L57, October 2018.

[22] G. A. Dulk. Radio emission from the sun and stars. , 23:169–224, January 1985.

[23] Rolando Dünner, Matthew Hasselfield, Tobias A. Marriage, Jon Sievers, Viviana Acquaviva, Graeme E. Addison, Peter A. R. Ade, Paula Aguirre, Mandana Amiri, John William Appel, L. Felipe Barrientos, Elia S. Battistelli, J. Richard Bond, Ben Brown, Bryce Burger, Erminia Calabrese, Jay Chervenak, Sudeep Das, Mark J. Devlin, Simon R. Dicker, W. Bertrand Doriese, Joanna Dunkley, Thomas Essinger-Hileman, Ryan P. Fisher, Megan B. Gralla, Joseph W. Fowler, Amir Hajian, Mark Halpern, Carlos Hernández-Monteagudo, Gene C. Hilton, Matt Hilton, Adam D. Hincks, Renée Hlozek, Kevin M. Huffenberger, David H. Hughes, John P. Hughes, Leopoldo Infante, Kent D. Irwin, Jean Baptiste Juin, Madhuri Kaul, Jeff Klein, Arthur

Kosowsky, Judy M. Lau, Michele Limon, Yen-Ting Lin, Thibaut Louis, Robert H. Lupton, Danica Marsden, Krista Martocci, Phil Mauskopf, Felipe Menanteau, Kavilan Moodley, Harvey Moseley, Calvin B. Netterfield, Michael D. Niemack, Michael R. Nolta, Lyman A. Page, Lucas Parker, Bruce Partridge, Hernan Quintana, Beth Reid, Neelima Sehgal, Blake D. Sherwin, David N. Spergel, Suzanne T. Staggs, Daniel S. Swetz, Eric R. Switzer, Robert Thornton, Hy Trac, Carole Tucker, Ryan Warne, Grant Wilson, Ed Wollack, and Yue Zhao. THE ATACAMA COSMOLOGY TELESCOPE: DATA CHARACTERIZATION AND MAPMAKING. *The Astrophysical Journal*, 762(1):10, dec 2012.

[24] T. Eftekhari, E. Berger, B. D. Metzger, T. Laskar, V. A. Villar, K. D. Alexander, G. P. Holder, J. D. Vieira, N. Whitehorn, and P. K. G. Williams. Extragalactic millimeter transients in the era of next-generation CMB surveys. *The Astrophysical Journal*, 935(1):16, aug 2022.

[25] J. W. Fowler, M. D. Niemack, S. R. Dicker, A. M. Aboobaker, P. A. R. Ade, E. S. Battistelli, M. J. Devlin, R. P. Fisher, M. Halpern, P. C. Hargrave, A. D. Hincks, M. Kaul, J. Klein, J. M. Lau, M. Limon, T. A. Marriage, P. D. Mauskopf, L. Page, S. T. Staggs, D. S. Swetz, E. R. Switzer, R. J. Thornton, and C. E. Tucker. Optical design of the atacama cosmology telescope and the millimeter bolometric array camera. *Appl. Opt.*, 46(17):3444–3454, Jun 2007.

[26] Gaia Collaboration, T. Prusti, J. H. J. de Bruijne, A. G. A. Brown, A. Vallenari, C. Babusiaux, C. A. L. Bailer-Jones, U. Bastian, M. Biermann, D. W. Evans, L. Eyer, F. Jansen, C. Jordi, S. A. Klioner, U. Lammers, L. Lindegren, X. Luri, F. Mignard, D. J. Milligan, C. Panem, V. Poinsignon, D. Pourbaix, S. Randich, G. Sarri, P. Sartoretti, H. I. Siddiqui, C. Soubiran, V. Valette, F. van Leeuwen, N. A. Walton, C. Aerts, F. Arenou, M. Cropper, R. Drimmel, E. Høg, D. Katz, M. G. Lattanzi, W. O'Mullane, E. K. Grebel, A. D. Holland, C. Huc, X. Passot, L. Bramante, C. Cacciari, J. Castañeda, L. Chaoul, N. Cheek, F. De Angeli, C. Fabricius, R. Guerra, J. Hernández, A. Jean-Antoine-Piccolo, E. Masana, R. Messineo, N. Mowlavi, K. Nienartowicz, D. Ordóñez-Blanco, P. Panuzzo, J. Portell, P. J. Richards, M. Riello, G. M. Seabroke, P. Tanga, F. Thévenin, J. Torra, S. G. Els, G. Gracia-Abril, G. Comoretto, M. Garcia-Reinaldos, T. Lock, E. Mercier, M. Altmann, R. Andrae, T. L. Astraatmadja, I. Bellas-Velidis, K. Benson, J. Berthier, R. Blomme, G. Busso, B. Carry, A. Cellino, G. Clementini, S. Cowell, O. Creevey, J. Cuypers, M. Davidson, J. De Ridder, A. de Torres, L. Delchambre, A. Dell'Oro, C. Ducourant, Y. Frémat, M. García-Torres, E. Gosset, J. L. Halbwachs, N. C. Hambly, D. L. Harrison, M. Hauser, D. Hestroffer, S. T. Hodgkin, H. E. Huckle, A. Hutton, G. Jasniewicz, S. Jordan, M. Kontizas, A. J. Korn, A. C. Lanzafame, M. Manteiga, A. Moitinho, K. Muinonen, J. Osinde, E. Pancino, T. Pauwels, J. M. Petit, A. Recio-Blanco, A. C. Robin, L. M. Sarro, C. Siopis, M. Smith, K. W. Smith, A. Sozzetti, W. Thuillot, W. van Reeven, Y. Viala, U. Abbas, A. Abreu Aramburu, S. Accart, J. J. Aguado, P. M. Allan, W. Al-

lasia, G. Altavilla, M. A. Álvarez, J. Alves, R. I. Anderson, A. H. Andrei, E. Anglada Varela, E. Antiche, T. Antoja, S. Antón, B. Arcay, A. Atzei, L. Ayache, N. Bach, S. G. Baker, L. Balaguer-Núñez, C. Barache, C. Barata, A. Barbier, F. Barblan, M. Baroni, D. Barrado y Navascués, M. Barros, M. A. Barstow, U. Becciani, M. Bellazzini, G. Bellei, A. Bello García, V. Belokurov, P. Bendjoya, A. Berihuete, L. Bianchi, O. Bienaymé, F. Billebaud, N. Blagorodnova, S. Blanco-Cuaresma, T. Boch, A. Bombrun, R. Borrachero, S. Bouquillon, G. Bourda, H. Bouy, A. Bragaglia, M. A. Breddels, N. Brouillet, T. Brüsemeister, B. Bucciarelli, F. Budnik, P. Burgess, R. Burgon, A. Burlacu, D. Busonero, R. Buzzi, E. Caffau, J. Cambras, H. Campbell, R. Cancelliere, T. Cantat-Gaudin, T. Carlucci, J. M. Carrasco, M. Castellani, P. Charlot, J. Charnas, P. Charvet, F. Chassat, A. Chiavassa, M. Clotet, G. Cocozza, R. S. Collins, P. Collins, G. Costigan, F. Crifo, N. J. G. Cross, M. Crosta, C. Crowley, C. Dafonte, Y. Damerdji, A. Dapergolas, P. David, M. David, P. De Cat, F. de Felice, P. de Laverny, F. De Luise, R. De March, D. de Martino, R. de Souza, J. Debosscher, E. del Pozo, M. Delbo, A. Delgado, H. E. Delgado, F. di Marco, P. Di Matteo, S. Diakite, E. Distefano, C. Dolding, S. Dos Anjos, P. Drazinos, J. Durán, Y. Dzigan, E. Ecale, B. Edvardsson, H. Enke, M. Erdmann, D. Escolar, M. Espina, N. W. Evans, G. Eynard Bontemps, C. Fabre, M. Fabrizio, S. Faigler, A. J. Falcão, M. Farràs Casas, F. Faye, L. Federici, G. Fedorets, J. Fernández-Hernández, P. Fernique, A. Fienga, F. Figueras, F. Filippi, K. Findeisen, A. Fonti, M. Fouesneau, E. Fraile, M. Fraser, J. Fuchs, R. Furnell, M. Gai, S. Galleti, L. Galluccio, D. Garabato, F. García-Sedano, P. Garé, A. Garofalo, N. Garralda, P. Gavras, J. Gerssen, R. Geyer, G. Gilmore, S. Girona, G. Giuffrida, M. Gomes, A. González-Marcos, J. González-Núñez, J. J. González-Vidal, M. Granvik, A. Guerrier, P. Guillout, J. Guiraud, A. Gúrpide, R. Gutiérrez-Sánchez, L. P. Guy, R. Haigron, D. Hatzidimitriou, M. Haywood, U. Heiter, A. Helmi, D. Hobbs, W. Hofmann, B. Holl, G. Holland, J. A. S. Hunt, A. Hypki, V. Icardi, M. Irwin, G. Jevardat de Fombelle, P. Jofré, P. G. Jonker, A. Jorissen, F. Julbe, A. Karampelas, A. Kochoska, R. Kohley, K. Kolenberg, E. Kontizas, S. E. Koposov, G. Kordopatis, P. Koubsky, A. Kowalczyk, A. Krone-Martins, M. Kudryashova, I. Kull, R. K. Bachchan, F. Lacoste-Seris, A. F. Lanza, J. B. Lavigne, C. Le Poncin-Lafitte, Y. Lebreton, T. Lebzelter, S. Leccia, N. Leclerc, I. Lecoeur-Taibi, V. Lemaitre, H. Lenhardt, F. Leroux, S. Liao, E. Licata, H. E. P. Lindstrøm, T. A. Lister, E. Livanou, A. Lobel, W. Löffler, M. López, A. Lopez-Lozano, D. Lorenz, T. Loureiro, I. MacDonald, T. Magalhães Fernandes, S. Managau, R. G. Mann, G. Mantelet, O. Marchal, J. M. Marchant, M. Marconi, J. Marie, S. Marinoni, P. M. Marrese, G. Marschalkó, D. J. Marshall, J. M. Martín-Fleitas, M. Martino, N. Mary, G. Matijevič, T. Mazeh, P. J. McMillan, S. Messina, A. Mestre, D. Michalik, N. R. Millar, B. M. H. Miranda, D. Molina, R. Molinaro, M. Molinaro, L. Molnár, M. Moniez, P. Montegriffo, D. Monteiro, R. Mor, A. Mora, R. Morbidelli, T. Morel, S. Morgenthaler, T. Morley, D. Morris, A. F. Mulone, T. Muraveva, I. Musella, J. Narbonne, G. Nelemans, L. Nicastro, L. Noval, C. Ordénovic, J. Ordieres-Meré, P. Osborne, C. Pagani, I. Pagano, F. Pailler, H. Palacin, L. Palaversa, P. Parsons, T. Paulsen, M. Pecoraro, R. Pedrosa, H. Pentikäinen, J. Pereira, B. Pichon, A. M. Piersimoni, F. X. Pineau, E. Plachy, G. Plum, E. Poujoulet, A. Prša, L. Pulone, S. Ragaini, S. Rago, N. Rambaux, M. Ramos-Lerate, P. Ranalli, G. Rauw, A. Read, S. Regibo, F. Renk, C. Reylé, R. A. Ribeiro, L. Ri-

moldini, V. Ripepi, A. Riva, G. Rixon, M. Roelens, M. Romero-Gómez, N. Rowell, F. Royer, A. Rudolph, L. Ruiz-Dern, G. Sadowski, T. Sagristà Sellés, J. Sahlmann, J. Salgado, E. Salguero, M. Sarasso, H. Savietto, A. Schnorhk, M. Schultheis, E. Sciacca, M. Segol, J. C. Segovia, D. Segransan, E. Serpell, I. C. Shih, R. Smareglia, R. L. Smart, C. Smith, E. Solano, F. Solitro, R. Sordo, S. Soria Nieto, J. Souchay, A. Spagna, F. Spoto, U. Stampa, I. A. Steele, H. Steidelmüller, C. A. Stephenson, H. Stoev, F. F. Suess, M. Süveges, J. Surdej, L. Szabados, E. Szegedi-Elek, D. Tapiador, F. Taris, G. Tauran, M. B. Taylor, R. Teixeira, D. Terrett, B. Tingley, S. C. Trager, C. Turon, A. Ulla, E. Utrilla, G. Valentini, A. van Elteren, E. Van Hemelryck, M. van Leeuwen, M. Varadi, A. Vecchiato, J. Veljanoski, T. Via, D. Vicente, S. Vogt, H. Voss, V. Votruba, S. Voutsinas, G. Walmsley, M. Weiler, K. Weingrill, D. Werner, T. Wevers, G. Whitehead, Ł. Wyrzykowski, A. Yoldas, M. Žerjal, S. Zucker, C. Zurbach, T. Zwitter, A. Alecu, M. Allen, C. Allende Prieto, A. Amorim, G. Anglada-Escudé, V. Arsenijevic, S. Azaz, P. Balm, M. Beck, H. H. Bernstein, L. Bigot, A. Bijaoui, C. Blasco, M. Bonfigli, G. Bono, S. Boudreault, A. Bressan, S. Brown, P. M. Brunet, P. Bunclark, R. Buonanno, A. G. Butkevich, C. Carret, C. Carrion, L. Chemin, F. Chéreau, L. Corcione, E. Darmigny, K. S. de Boer, P. de Teodoro, P. T. de Zeeuw, C. Delle Luche, C. D. Domingues, P. Dubath, F. Fodor, B. Frézouls, A. Fries, D. Fustes, D. Fyfe, E. Gallardo, J. Gallegos, D. Gardiol, M. Gebran, A. Gomboc, A. Gómez, E. Grux, A. Gueguen, A. Heyrovsky, J. Hoar, G. Iannicola, Y. Isasi Parache, A. M. Janotto, E. Joliet, A. Jonckheere, R. Keil, D. W. Kim, P. Klagyivik, J. Klar, J. Knude, O. Kochukhov, I. Kolka, J. Kos, A. Kutka, V. Lainey, D. LeBouquin, C. Liu, D. Loreggia, V. V. Makarov, M. G. Marseille, C. Martayan, O. Martinez-Rubi, B. Massart, F. Meynadier, S. Mignot, U. Munari, A. T. Nguyen, T. Nordlander, P. Ocvirk, K. S. O'Flaherty, A. Olias Sanz, P. Ortiz, J. Osorio, D. Oszkiewicz, A. Ouzounis, M. Palmer, P. Park, E. Pasquato, C. Peltzer, J. Peralta, F. Péturaud, T. Pieniluoma, E. Pigozzi, J. Poels, G. Prat, T. Prod'homme, F. Raison, J. M. Rebordao, D. Risquez, B. Rocca-Volmerange, S. Rosen, M. I. Ruiz-Fuertes, F. Russo, S. Sembay, I. Serraller Vizcaino, A. Short, A. Siebert, H. Silva, D. Sinachopoulos, E. Slezak, M. Soffel, D. Sosnowska, V. Straižys, M. ter Linden, D. Terrell, S. Theil, C. Tiede, L. Troisi, P. Tsalmantza, D. Tur, M. Vaccari, F. Vachier, P. Valles, W. Van Hamme, L. Veltz, J. Virtanen, J. M. Wallut, R. Wichmann, M. I. Wilkinson, H. Ziaeepour, and S. Zschocke. The Gaia mission. , 595:A1, November 2016.

[27] Gaia Collaboration, A. Vallenari, A. G. A. Brown, T. Prusti, J. H. J. de Bruijne, F. Arenou, C. Babusiaux, M. Biermann, O. L. Creevey, C. Ducourant, D. W. Evans, L. Eyer, R. Guerra, A. Hutton, C. Jordi, S. A. Klioner, U. L. Lammers, L. Lindegren, X. Luri, F. Mignard, C. Panem, D. Pourbaix, S. Randich, P. Sartoretti, C. Soubiran, P. Tanga, N. A. Walton, C. A. L. Bailer-Jones, U. Bastian, R. Drimmel, F. Jansen, D. Katz, M. G. Lattanzi, F. van Leeuwen, J. Bakker, C. Cacciari, J. Castañeda, F. De Angeli, C. Fabricius, M. Fouesneau, Y. Frémat, L. Galluccio, A. Guerrier, U. Heiter, E. Masana, R. Messineo, N. Mowlavi, C. Nicolas, K. Nienartowicz, F. Pailler, P. Panuzzo, F. Riclet, W. Roux, G. M. Seabroke, R. Sordo, F. Thévenin,

G. Gracia-Abril, J. Portell, D. Teyssier, M. Altmann, R. Andrae, M. Audard, I. Bellas-Velidis, K. Benson, J. Berthier, R. Blomme, P. W. Burgess, D. Busonero, G. Busso, H. Cánovas, B. Carry, A. Cellino, N. Cheek, G. Clementini, Y. Damerdji, M. Davidson, P. de Teodoro, M. Nuñez Campos, L. Delchambre, A. Dell'Oro, P. Esquej, J. Fernández-Hernández, E. Fraile, D. Garabato, P. García-Lario, E. Gosset, R. Haigron, J. L. Halbwachs, N. C. Hambly, D. L. Harrison, J. Hernández, D. Hestroffer, S. T. Hodgkin, B. Holl, K. Janßen, G. Jevardat de Fombelle, S. Jordan, A. Krone-Martins, A. C. Lanzafame, W. Löffler, O. Marchal, P. M. Marrese, A. Moitinho, K. Muinonen, P. Osborne, E. Pancino, T. Pauwels, A. Recio-Blanco, C. Reylé, M. Riello, L. Rimoldini, T. Roegiers, J. Rybizki, L. M. Sarro, C. Siopis, M. Smith, A. Sozzetti, E. Utrilla, M. van Leeuwen, U. Abbas, P. Ábrahám, A. Abreu Aramburu, C. Aerts, J. J. Aguado, M. Ajaj, F. Aldea-Montero, G. Altavilla, M. A. Álvarez, J. Alves, F. Anders, R. I. Anderson, E. Anglada Varela, T. Antoja, D. Baines, S. G. Baker, L. Balaguer-Núñez, E. Balbinot, Z. Balog, C. Barache, D. Barbato, M. Barros, M. A. Barstow, S. Bartolomé, J. L. Bassilana, N. Bauchet, U. Becciani, M. Bellazzini, A. Berihuete, M. Bernet, S. Bertone, L. Bianchi, A. Binnenfeld, S. Blanco-Cuaresma, A. Blazere, T. Boch, A. Bombrun, D. Bossini, S. Bouquillon, A. Bragaglia, L. Bramante, E. Breedt, A. Bressan, N. Brouillet, E. Brugaletta, B. Bucciarelli, A. Burlacu, A. G. Butkevich, R. Buzzi, E. Caffau, R. Cancelliere, T. Cantat-Gaudin, R. Carballo, T. Carlucci, M. I. Carnerero, J. M. Carrasco, L. Casamiquela, M. Castellani, A. Castro-Ginard, L. Chaoul, P. Charlot, L. Chemin, V. Chiaramida, A. Chiavassa, N. Chornay, G. Comoretto, G. Contursi, W. J. Cooper, T. Cornez, S. Cowell, F. Crifo, M. Cropper, M. Crosta, C. Crowley, C. Dafonte, A. Dapergolas, M. David, P. David, P. de Laverny, F. De Luise, R. De March, J. De Ridder, R. de Souza, A. de Torres, E. F. del Peloso, E. del Pozo, M. Delbo, A. Delgado, J. B. Delisle, C. Demouchy, T. E. Dharmawardena, P. Di Matteo, S. Diakite, C. Diener, E. Distefano, C. Dolding, B. Edvardsson, H. Enke, C. Fabre, M. Fabrizio, S. Faigler, G. Fedorets, P. Fernique, A. Fienga, F. Figueras, Y. Fournier, C. Fouron, F. Fragkoudi, M. Gai, A. Garcia-Gutierrez, M. Garcia-Reinaldos, M. García-Torres, A. Garofalo, A. Gavel, P. Gavras, E. Gerlach, R. Geyer, P. Giacobbe, G. Gilmore, S. Girona, G. Giuffrida, R. Gomel, A. Gomez, J. González-Núñez, I. González-Santamaría, J. J. González-Vidal, M. Granvik, P. Guillout, J. Guiraud, R. Gutiérrez-Sánchez, L. P. Guy, D. Hatzidimitriou, M. Hauser, M. Haywood, A. Helmer, A. Helmi, M. H. Sarmiento, S. L. Hidalgo, T. Hilger, N. Hładczuk, D. Hobbs, G. Holland, H. E. Huckle, K. Jardine, G. Jasniewicz, A. Jean-Antoine Piccolo, Ó. Jiménez-Arranz, A. Jorissen, J. Juaristi Campillo, F. Julbe, L. Karbevska, P. Kervella, S. Khanna, M. Kontizas, G. Kordopatis, A. J. Korn, Á. Kóspál, Z. Kostrzewa-Rutkowska, K. Kruszyńska, M. Kun, P. Laizeau, S. Lambert, A. F. Lanza, Y. Lasne, J. F. Le Campion, Y. Lebreton, T. Lebzelter, S. Leccia, N. Leclerc, I. Lecoeur-Taibi, S. Liao, E. L. Licata, H. E. P. Lindstrøm, T. A. Lister, E. Livanou, A. Lobel, A. Lorca, C. Loup, P. Madrero Pardo, A. Magdaleno Romeo, S. Managau, R. G. Mann, M. Manteiga, J. M. Marchant, M. Marconi, J. Marcos, M. M. S. Marcos Santos, D. Marín Pina, S. Marinoni, F. Marocco, D. J. Marshall, L. Martin Polo, J. M. Martín-Fleitas, G. Marton, N. Mary, A. Masip, D. Massari, A. Mastrobuono-Battisti, T. Mazeh, P. J. McMillan, S. Messina, D. Michalik, N. R. Millar, A. Mints, D. Molina, R. Molinaro, L. Molnár, G. Monari,

M. Monguió, P. Montegriffo, A. Montero, R. Mor, A. Mora, R. Morbidelli, T. Morel, D. Morris, T. Muraveva, C. P. Murphy, I. Musella, Z. Nagy, L. Noval, F. Ocaña, A. Ogden, C. Ordenovic, J. O. Osinde, C. Pagani, I. Pagano, L. Palaversa, P. A. Palicio, L. Pallas-Quintela, A. Panahi, S. Payne-Wardenaar, X. Peñalosa Esteller, A. Penttilä, B. Pichon, A. M. Piersimoni, F. X. Pineau, E. Plachy, G. Plum, E. Poggio, A. Prša, L. Pulone, E. Racero, S. Ragaini, M. Rainer, C. M. Raiteri, N. Rambaux, P. Ramos, M. Ramos-Lerate, P. Re Fiorentin, S. Regibo, P. J. Richards, C. Rios Diaz, V. Ripepi, A. Riva, H. W. Rix, G. Rixon, N. Robichon, A. C. Robin, C. Robin, M. Roelens, H. R. O. Rogues, L. Rohrbasser, M. Romero-Gómez, N. Rowell, F. Royer, D. Ruz Mieres, K. A. Rybicki, G. Sadowski, A. Sáez Núñez, A. Sagristà Sellés, J. Sahlmann, E. Salguero, N. Samaras, V. Sanchez Gimenez, N. Sanna, R. Santoveña, M. Sarasso, M. Schultheis, E. Sciacca, M. Segol, J. C. Segovia, D. Ségransan, D. Semeux, S. Shahaf, H. I. Siddiqui, A. Siebert, L. Siltala, A. Silvelo, E. Slezak, I. Slezak, R. L. Smart, O. N. Snaith, E. Solano, F. Solitro, D. Souami, J. Souchay, A. Spagna, L. Spina, F. Spoto, I. A. Steele, H. Steidelmüller, C. A. Stephenson, M. Süveges, J. Surdej, L. Szabados, E. Szegedi-Elek, F. Taris, M. B. Taylor, R. Teixeira, L. Tolomei, N. Tonello, F. Torra, J. Torra, G. Torralba Elipe, M. Trabucchi, A. T. Tsounis, C. Turon, A. Ulla, N. Unger, M. V. Vaillant, E. van Dillen, W. van Reeven, O. Vanel, A. Vecchiato, Y. Viala, D. Vicente, S. Voutsinas, M. Weiler, T. Wevers, Ł. Wyrzykowski, A. Yoldas, P. Yvard, H. Zhao, J. Zorec, S. Zucker, and T. Zwitter. Gaia Data Release 3. Summary of the content and survey properties. , 674:A1, June 2023.

[28] J. S. Gallagher and S. Starrfield. Theory and observations of classical novae. , 16:171–214, January 1978.

[29] A. Ginsburg, B. M. Sipőcz, C. E. Brasseur, P. S. Cowperthwaite, M. W. Craig, C. Deil, J. Guillochon, G. Guzman, S. Liedtke, P. Lian Lim, K. E. Lockhart, M. Mommert, B. M. Morris, H. Norman, M. Parikh, M. V. Persson, T. P. Robitaille, J.-C. Segovia, L. P. Singer, E. J. Tollerud, M. de Val-Borro, I. Valtchanov, J. Woillez, The Astroquery collaboration, and a subset of the astropy collaboration. astroquery: An Astronomical Web-querying Package in Python. , 157:98, March 2019.

[30] S. Guns, A. Foster, C. Daley, A. Rahlin, N. Whitehorn, P. A. R. Ade, Z. Ahmed, E. Anderes, A. J. Anderson, M. Archipley, and et al. Detection of galactic and extragalactic millimeter-wavelength transient sources with spt-3g. *The Astrophysical Journal*, 916(2):98, Aug 2021.

[31] Izumi Hachisu and Mariko Kato. A Multiwavelength Light-curve Analysis of the Classical Nova YZ Ret: An Extension of the Universal Decline Law to the Nebular Phase. , 953(1):78, August 2023.

[32] Douglas S. Hall. The rs cvn binaries and binaries with similar properties. *International Astronomical Union Colloquium*, 29:287–348, 1976.

[33] S. W. Henderson, R. Allison, J. Austermann, T. Baildon, N. Battaglia, J. A. Beall, D. Becker, F. De Bernardis, J. R. Bond, E. Calabrese, S. K. Choi, K. P. Coughlin, K. T. Crowley, R. Datta, M. J. Devlin, S. M. Duff, J. Dunkley, R. Dünner, A. van Engelen, P. A. Gallardo, E. Grace, M. Hasselfield, F. Hills, G. C. Hilton, A. D. Hincks, R. Hloẑek, S. P. Ho, J. Hubmayr, K. Huffenberger, J. P. Hughes, K. D. Irwin, B. J. Koopman, A. B. Kosowsky, D. Li, J. McMahon, C. Munson, F. Nati, L. Newburgh, M. D. Niemack, P. Niraula, L. A. Page, C. G. Pappas, M. Salatino, A. Schillaci, B. L. Schmitt, N. Sehgal, B. D. Sherwin, J. L. Sievers, S. M. Simon, D. N. Spergel, S. T. Staggs, J. R. Stevens, R. Thornton, J. Van Lanen, E. M. Vavagiakis, J. T. Ward, and E. J. Wollack. Advanced ACTPol Cryogenic Detector Arrays and Readout. *Journal of Low Temperature Physics*, 184(3-4):772–779, August 2016.

[34] Carlos Hervías-Caimapo, Sigurd Naess, Adam D. Hincks, Erminia Calabrese, Mark J. Devlin, Jo Dunkley, Rolando Dünner, Patricio A. Gallardo, Matt Hilton, Anna Y. Q. Ho, Kevin M. Huffenberger, Xiaoyi Ma, Mathew S. Madhavacheril, Michael D. Niemack, John Orlowski-Scherer, Lyman A. Page, Bruce Partridge, Roberto Puddu, Maria Salatino, Cristóbal Sifón, Suzanne T. Staggs, Cristian Vargas, Eve M. Vavagiakis, and Edward J. Wollack. The Atacama cosmology telescope: flux upper limits from a targeted search for extragalactic transients. , 529(3):3020–3034, April 2024.

[35] R. M. Hjellming and D. M. Gibson. Nonthermal microwave phenomena in other stars. In M. R. Kundu and T. E. Gergely, editors, *Radio Physics of the Sun*, volume 86, pages 209–220, January 1980.

[36] Anna Y. Q. Ho, E. Sterl Phinney, Vikram Ravi, S. R. Kulkarni, Glen Petitpas, Bjorn Emonts, V. Bhalerao, Ray Blundell, S. Bradley Cenko, Dougal Dobie, Ryan Howie, Nikita Kamraj, Mansi M. Kasliwal, Tara Murphy, Daniel A. Perley, T. K. Sridharan, and Ilsang Yoon. AT2018cow: A Luminous Millimeter Transient. , 871(1):73, January 2019.

[37] Shuay-Pwu Patty Ho, Jason Austermann, James A. Beall, Steve K. Choi, Nicholas F. Cothard, Kevin T. Crowley, Rahul Datta, Mark J. Devlin, Shannon M. Duff, Patricio A. Gallardo, Matthew Hasselfield, Shawn W. Henderson, Gene Hilton, Johannes Hubmayr, Brian J. Koopman, Yaqiong Li, Jeffrey McMahon, Michael D. Niemack, Maria Salatino, Sara M. Simon, Suzanne T. Staggs, Jonathan T. Ward, Joel N. Ullom, Eve M. Vavagiakis, and Edward J. Wollack. Highly uniform 150 mm diameter multichroic polarimeter array deployed for CMB detection. In Wayne S. Holland and Jonas Zmuidzinas, editors, *Millimeter, Submillimeter, and Far-Infrared Detectors and*

Instrumentation for Astronomy VIII, volume 9914, page 991418. International Society for Optics and Photonics, SPIE, 2017.

[38] R. J. Ivison, D. H. Hughes, H. M. Lloyd, M. K. Bang, and M. F. Bode. Millimetre and submillimetre continuum observations of Nova Cygni 1992: a new test of mass ejection models. *Monthly Notices of the Royal Astronomical Society*, 263(1):L43–L46, 07 1993.

[39] P. Kahabka and E. P. J. van den Heuvel. Luminous supersoft x-ray sources. *Annual Review of Astronomy and Astrophysics*, 35(Volume 35, 1997):69–100, 1997.

[40] Chryssa Kouveliotou, Charles A. Meegan, Gerald J. Fishman, Narayana P. Bhat, Michael S. Briggs, Thomas M. Koshut, William S. Paciesas, and Geoffrey N. Pendleton. Identification of Two Classes of Gamma-Ray Bursts. , 413:L101, August 1993.

[41] Adam F. Kowalski. Stellar flares. *Living Reviews in Solar Physics*, 21(1), Apr 2024.

[42] M. Kuerster and J. H. M. M. Schmitt. Forty days in the life of CF Tucanae (=HD 5303). The longest stellar X-ray flare observed with ROSAT. , 311:211–229, July 1996.

[43] Nario Kuno, Naoko Sato, Hiroyuki Nakanishi, Aya Yamauchi, Naomasa Nakai, and Nobuyuki Kawai. Radio observations of the afterglow of GRB 030329. *Publications of the Astronomical Society of Japan*, 56(2):L1–L4, apr 2004.

[44] Ole König, Jörn Wilms, Riccardo Arcodia, Thomas Dauser, Konrad Dennerl, Victor Doroshenko, Frank Haberl, Steven Hämmerich, Christian Kirsch, Ingo Kreykenbohm, and et al. X-ray detection of a nova in the fireball phase. *Nature*, 605(7909):248–250, May 2022.

[45] Tanmoy Laskar, Kate D. Alexander, Ramandeep Gill, Jonathan Granot, Edo Berger, C. G. Mundell, Rodolfo Barniol Duran, J. Bolmer, Paul Duffell, Hendrik van Eerten, Wen fai Fong, Shiho Kobayashi, Raffaella Margutti, and Patricia Schady. ALMA detection of a linearly polarized reverse shock in GRB 190114c. *The Astrophysical Journal*, 878(1):L26, jun 2019.

[46] C. J. Law, B. M. Gaensler, B. D. Metzger, E. O. Ofek, and L. Sironi. Discovery of the luminous, decades-long, extragalactic radio transient first j141918.9+394036. *The Astrophysical Journal Letters*, 866(2), Oct 2018.

[47] Yaqiong Li, Emily Biermann, Sigurd Naess, Simone Aiola, Rui An, Nicholas Battaglia, Tanay Bhandarkar, Erminia Calabrese, Steve K. Choi, Kevin T. Crowley, and et al. The atacama cosmology telescope: Systematic transient search of 3 day maps. *The Astrophysical Journal*, 956(1):36, 2023.

[48] D. R. Lorimer, M. Bailes, M. A. McLaughlin, D. J. Narkevic, and F. Crawford. A Bright Millisecond Radio Burst of Extragalactic Origin. *Science*, 318(5851):777, November 2007.

[49] Orlando Luongo and Marco Muccino. A roadmap to gamma-ray bursts: New developments and applications to cosmology. *Galaxies*, 9(4), 2021.

[50] A. Meredith MacGregor, Rachel A. Osten, and A. Meredith Hughes. Properties of m dwarf flares at millimeter wavelengths. *The Astrophysical Journal*, 891(1):80, 2020.

[51] Meredith A. MacGregor, Alycia J. Weinberger, R. O. Parke Loyd, Evgenya Shkolnik, Thomas Barclay, Ward S. Howard, Andrew Zic, Rachel A. Osten, Steven R. Cranmer, Adam F. Kowalski, Emil Lenc, Allison Youngblood, Anna Estes, David J. Wilner, Jan Forbrich, Anna Hughes, Nicholas M. Law, Tara Murphy, Aaron Boley, and Jaymie Matthews. Discovery of an Extremely Short Duration Flare from Proxima Centauri Using Millimeter through Far-ultraviolet Observations. , 911(2):L25, April 2021.

[52] Meredith A. MacGregor, Alycia J. Weinberger, David J. Wilner, Adam F. Kowalski, and Steven R. Cranmer. Detection of a millimeter flare from proxima centauri. *The Astrophysical Journal*, 855(1), 2018.

[53] Steve Mairs, Bhavana Lalchand, Geoffrey C. Bower, Jan Forbrich, Graham S. Bell, Gregory J. Herczeg, Doug Johnstone, Wen-Ping Chen, Jeong-Eun Lee, and Alvaro Hacar. The JCMT transient survey: An extraordinary submillimeter flare in the t tauri binary system JW 566. *The Astrophysical Journal*, 871(1):72, jan 2019.

[54] B. Marcote, K. Nimmo, O. S. Salafia, Z. Paragi, J. W. Hessels, E. Petroff, and R. Karuppusamy. Resolving the decades-long transient first j141918.9+394036: An orphan long gamma-ray burst or a young magnetar nebula? *The Astrophysical Journal Letters*, 876(1), May 2019.

[55] R. Margutti, B. D. Metzger, R. Chornock, I. Vurm, N. Roth, B. W. Grefenstette, V. Savchenko, R. Cartier, J. F. Steiner, G. Terreran, B. Margalit, G. Migliori, D. Milisavljevic, K. D. Alexander, M. Bietenholz, P. K. Blanchard, E. Bozzo, D. Brethauer, I. V. Chilingarian, D. L. Coppejans, L. Ducci, C. Ferrigno, W. Fong, D. Götz, C. Guidorzi, A. Hajela, K. Hurley, E. Kuulkers, P. Laurent, S. Mereghetti, M. Nicholl,

D. Patnaude, P. Ubertini, J. Banovetz, N. Bartel, E. Berger, E. R. Coughlin, T. Eftekhari, D. D. Frederiks, A. V. Kozlova, T. Laskar, D. S. Svinkin, M. R. Drout, A. MacFadyen, and K. Paterson. An Embedded X-Ray Source Shines through the Aspherical AT 2018cow: Revealing the Inner Workings of the Most Luminous Fast-evolving Optical Transients. , 872(1):18, February 2019.

[56] Frank J. Masci, Russ R. Laher, Ben Rusholme, David L. Shupe, Steven Groom, Jason Surace, Edward Jackson, Serge Monkewitz, Ron Beck, David Flynn, Scott Terek, Walter Landry, Eugean Hacopians, Vandana Desai, Justin Howell, Tim Brooke, David Imel, Stefanie Wachter, Quan-Zhi Ye, Hsing-Wen Lin, S. Bradley Cenko, Virginia Cunningham, Umaa Rebbapragada, Brian Bue, Adam A. Miller, Ashish Mahabal, Eric C. Bellm, Maria T. Patterson, Mario Jurić, V. Zach Golkhou, Eran O. Ofek, Richard Walters, Matthew Graham, Mansi M. Kasliwal, Richard G. Dekany, Thomas Kupfer, Kevin Burdge, Christopher B. Cannella, Tom Barlow, Angela Van Sistine, Matteo Giomi, Christoffer Fremling, Nadejda Blagorodnova, David Levitan, Reed Riddle, Roger M. Smith, George Helou, Thomas A. Prince, and Shrinivas R. Kulkarni. The zwicky transient facility: Data processing, products, and archive. *Publications of the Astronomical Society of the Pacific*, 131(995):018003, dec 2018.

[57] M. Massi, J. Forbrich, K. M. Menten, G. Torricelli-Ciamponi, J. Neidhöfer, S. Leurini, and F. Bertoldi. Synchrotron emission from the t tauri binary system v773 tauri a. *Astronomy & Astrophysics*, 453(3):959–964, jun 2006.

[58] Thomas Matheson, Carl Stubens, Nicholas Wolf, Chien-Hsiu Lee, Gautham Narayan, Abhijit Saha, Adam Scott, Monika Soraisam, Adam S. Bolton, Benjamin Hauger, David R. Silva, John Kececioglu, Carlos Scheidegger, Richard Snodgrass, Patrick D. Aleo, Eric Evans-Jacquez, Navdeep Singh, Zhe Wang, Shuo Yang, and Zhenge Zhao. The antares astronomical time-domain event broker. *The Astronomical Journal*, 161(3):107, feb 2021.

[59] Z. Mouradian, M. J. Martres, and I. Soru-Escaut. The emerging magnetic flux and the elementary eruptive phenomenon. , 87(2):309–328, September 1983.

[60] Isabel Márquez, Josefa Masegosa, Omaira González-Martin, Lorena Hernández-Garcia, Mirjana Pović, Hagai Netzer, Sara Cazzoli, and Ascensión del Olmo. The agn nature of liner nuclear sources. *Frontiers in Astronomy and Space Sciences*, 4, 2017.

[61] Sigurd Naess, Simone Aiola, Nick Battaglia, Richard J. Bond, Erminia Calabrese, Steve K. Choi, Nicholas F. Cothard, Mark Halpern, J. Colin Hill, Brian J. Koopman, and et al. The atacama cosmology telescope: A search for planet 9. *The Astrophysical Journal*, 923(2):224, Dec 2021.

[62] Sigurd Naess, Nick Battaglia, J. Richard Bond, Erminia Calabrese, Steve K. Choi, Nicholas F. Cothard, Mark Devlin, Cody J. Duell, Adriaan J. Duivenvoorden, Jo Dunkley, and et al. The atacama cosmology telescope: Detection of millimeter-wave transient sources. *The Astrophysical Journal*, 915(1):14, Jun 2021.

[63] Cherry Ng. A brief review on fast radio bursts, 2023.

[64] R. W. Noyes, L. W. Hartmann, S. L. Baliunas, D. K. Duncan, and A. H. Vaughan. Rotation, convection, and magnetic activity in lower main-sequence stars. , 279:763–777, April 1984.

[65] F. Ochsenbein, P. Bauer, and J. Marcout. The VizieR database of astronomical catalogues. *Astronomy and Astrophysics Supplement Series*, 143(1):23–32, apr 2000.

[66] John Orlowski-Scherer, Ricco C. Venterea, Nicholas Battaglia, Sigurd Naess, Tanay Bhandarkar, Emily Biermann, Erminia Calabrese, Mark Devlin, Jo Dunkley, Carlos Hervías-Caimapo, Patricio A. Gallardo, Matt Hilton, Adam D. Hincks, Kenda Knowles, Yaqiong Li, Jeffrey J. McMahon, Michael D. Niemack, Lyman A. Page, Bruce Partridge, Maria Salatino, Jonathan Sievers, Cristóbal Sifón, Suzanne Staggs, Alexander van Engelen, Cristian Vargas, Eve M. Vavagiakis, and Edward J. Wollack. The Atacama Cosmology Telescope: Millimeter Observations of a Population of Asteroids or: ACTeroids. , 964(2):138, April 2024.

[67] A. G. Pacholczyk. *Radio astrophysics. Nonthermal processes in galactic and extragalactic sources*. 1970.

[68] A. Panaitescu and P. Mészáros. Dynamical evolution, light curves, and spectra of spherical and collimated gamma-ray burst remnants. *The Astrophysical Journal*, 526(2):707, dec 1999.

[69] Stephen C. Parshley, Michael Niemack, Richard Hills, Simon R. Dicker, Rolando Dünner, Jens Erler, Patricio A. Gallardo, Jon E. Gudmundsson, Terry Herter, Brian J. Koopman, Michele Limon, Frederick T. Matsuda, Philip Mauskopf, Dominik A. Riechers, Gordon J. Stacey, and Eve M. Vavagiakis. The optical design of the six-meter ccat-prime and simons observatory telescopes. In Heather K. Marshall and Jason Spyromilio, editors, *Ground-Based and Airborne Telescopes VII*, Proceedings of SPIE - The International Society for Optical Engineering. SPIE, 2018. Funding Information: Acknowledgements: CCAT-prime funding has been provided by Cornell University, the Fred M. Young Jr. Charitable Fund, the German Research Foundation (DFG) through grant number INST 216/733-1 FUGG, the Univ. of Cologne, the Univ. of Bonn, and the Canadian Atacama Telescope Consortium. Part of this

work was supported by a grant from the Simons Foundation (Award 457687, B.K.). MDN acknowledges support from NSF award AST-1454881. RD thanks CONICYT for grants PIA Anillo ACT-1417 and QUIMAL 160009. Publisher Copyright: © 2018 SPIE.; Ground-Based and Airborne Telescopes VII 2018 ; Conference date: 10-06-2018 Through 15-06-2018.

[70] Cecilia Payne-Gaposchkin and C. C. Kiess. The Galactic Novae. *Physics Today*, 11(1):29–29, 01 1958.

[71] Daniel A Perley, Paolo A Mazzali, Lin Yan, S Bradley Cenko, Suvi Gezari, Kirsty Taggart, Nadia Blagorodnova, Christoffer Fremling, Brenna Mockler, Avinash Singh, Nozomu Tominaga, Masaomi Tanaka, Alan M Watson, Tomás Ahumada, G C Anupama, Chris Ashall, Rosa L Becerra, David Bersier, Varun Bhalerao, Joshua S Bloom, Nathaniel R Butler, Chris Copperwheat, Michael W Coughlin, Kishalay De, Andrew J Drake, Dmitry A Duev, Sara Frederick, J Jesús González, Ariel Goobar, Marianne Heida, Anna Y Q Ho, John Horst, Tiara Hung, Ryosuke Itoh, Jacob E Jencson, Mansi M Kasliwal, Nobuyuki Kawai, Tanazza Khanam, Shrinivas R Kulkarni, Brajesh Kumar, Harsh Kumar, Alexander S Kutyrev, William H Lee, Keiichi Maeda, Ashish Mahabal, Katsuhiro L Murata, James D Neill, Chow-Choong Ngeow, Bryan Penprase, Elena Pian, Robert Quimby, Enrico Ramirez-Ruiz, Michael G Richer, Carlos G Román-Zúñiga, D K Sahu, Shubham Srivastav, Quentin Socia, Jesper Sollerman, Yutaro Tachibana, Francesco Taddia, Samaporn Tinyanont, Eleonora Troja, Charlotte Ward, Jerrick Wee, and Po-Chieh Yu. The fast, luminous ultraviolet transient AT2018cow: extreme supernova, or disruption of a star by an intermediate-mass black hole? *Monthly Notices of the Royal Astronomical Society*, 484(1):1031–1049, 12 2018.

[72] Emily Petroff, J. Hessels, and D. Lorimer. Fast radio bursts at the dawn of the 2020s. *The Astronomy and Astrophysics Review*, 30, 03 2022.

[73] Tsvi Piran. The physics of gamma-ray bursts. *Rev. Mod. Phys.*, 76:1143–1210, Jan 2005.

[74] N. Pizzolato, A. Maggio, G. Micela, S. Sciortino, and P. Ventura. The stellar activity-rotation relationship revisited: Dependence of saturated and non-saturated X-ray emission regimes on stellar mass for late-type dwarfs. , 397:147–157, January 2003.

[75] S. J. Prentice, K. Maguire, S. J. Smartt, M. R. Magee, P. Schady, S. Sim, T.-W. Chen, P. Clark, C. Colin, M. Fulton, O. McBrien, D. O'Neill, K. W. Smith, C. Ashall, K. C. Chambers, L. Denneau, H. A. Flewelling, A. Heinze, T. W.-S. Holoien, M. E. Huber, C. S. Kochanek, P. A. Mazzali, J. L. Prieto, A. Rest, B. J. Shappee, B. Stalder, K. Z. Stanek, M. D. Stritzinger, T. A. Thompson, and J. L. Tonry. The cow: Discovery of

a luminous, hot, and rapidly evolving transient. *The Astrophysical Journal Letters*, 865(1):L3, sep 2018.

[76] V. Ravi et al. The magnetic field and turbulence of the cosmic web measured using a brilliant fast radio burst. *Science*, 354:1249, 2016.

[77] L. E. Rivera Sandoval, T. J. Maccarone, A. Corsi, P. J. Brown, D. Pooley, and J. C. Wheeler. X-ray Swift observations of SN 2018cow. , 480(1):L146–L150, October 2018.

[78] A Rowlinson, J Meijn, J Bright, A J van der Horst, S Chastain, S Fijma, R Fender, I Heywood, R A M J Wijers, P A Woudt, A Andersson, G R Sivakoff, E Tremou, and L N Driessen. Search and identification of transient and variable radio sources using MeerKAT observations: a case study on the MAXI J1820+070 field. *Monthly Notices of the Royal Astronomical Society*, 517(2):2894–2911, 09 2022.

[79] George B. Rybicki and Alan P. Lightman. *Radiative Processes in Astrophysics*. 1986.

[80] Salter, D. M., Kóspál, Á., Getman, K. V., Hogerheijde, M. R., van Kempen, T. A., Carpenter, J. M., Blake, G. A., and Wilner, D. Recurring millimeter flares as evidence for star-star magnetic reconnection events in the dq tauri pms binary system*. *AA*, 521:A32, 2010.

[81] N. N. Samus', E. V. Kazarovets, O. V. Durlevich, N. N. Kireeva, and E. N. Pastukhova. General catalogue of variable stars: Version gcvs 5.1. *Astronomy Reports*, 61(1):80–88, Jan 2017.

[82] Re'em Sari, Tsvi Piran, and J. P. Halpern. Jets in gamma-ray bursts. *The Astrophysical Journal*, 519(1):L17, may 1999.

[83] Re'em Sari, Tsvi Piran, and Ramesh Narayan. Spectra and light curves of gamma-ray burst afterglows. *The Astrophysical Journal*, 497(1):L17, mar 1998.

[84] Aomawa L. Shields, Sarah Ballard, and John Asher Johnson. The habitability of planets orbiting M-dwarf stars. , 663:1, December 2016.

[85] SO Collaboration. The simons observatory: Enhanced science goals and forecasts for the large aperture telescope, in prep. 2024.

[86] Kirill Sokolovsky, Elias Aydi, Laura Chomiuk, Adam Kawash, Jay Strader, Koji Mukai, Kwan-Lok Li, Stella Kafka, Marina Orio, Kim Page, and Andy Beardmore. Super-soft X-ray emission of Nova Reticuli 2020. *The Astronomer's Telegram*, 14043:1, September 2020.

[87] Kirill V Sokolovsky, Kwan-Lok Li, Raimundo Lopes de Oliveira, Jan-Uwe Ness, Koji Mukai, Laura Chomiuk, Elias Aydi, Elad Steinberg, Indrek Vurm, Brian D Metzger, Aliya-Nur Babul, Adam Kawash, Justin D Linford, Thomas Nelson, Kim L Page, Michael P Rupen, Jennifer L Sokoloski, Jay Strader, and David Kilkenny. The first nova eruption in a novalike variable: YZRet as seen in X-rays and -rays. *Monthly Notices of the Royal Astronomical Society*, 514(2):2239–2258, 05 2022.

[88] S. Starrfield, C. Iliadis, and W. R. Hix. The thermonuclear runaway and the classical nova outburst. *Publications of the Astronomical Society of the Pacific*, 128(963):051001, apr 2016.

[89] C. Tandoi, S. Guns, A. Foster, P. A. R. Ade, A. J. Anderson, B. Ansarinejad, M. Archipley, L. Balkenhol, K. Benabed, A. N. Bender, B. A. Benson, F. Bianchini, L. E. Bleem, F. R. Bouchet, L. Bryant, E. Camphuis, J. E. Carlstrom, T. W. Cecil, C. L. Chang, P. Chaubal, P. M. Chichura, T. L. Chou, A. Coerver, T. M. Crawford, A. Cukierman, C. Daley, T. de Haan, K. R. Dibert, M. A. Dobbs, A. Doussot, D. Dutcher, W. Everett, C. Feng, K. R. Ferguson, K. Fichman, S. Galli, A. E. Gambrel, R. W. Gardner, F. Ge, N. Goeckner-Wald, R. Gualtieri, F. Guidi, N. W. Halverson, E. Hivon, G. P. Holder, W. L. Holzapfel, J. C. Hood, N. Huang, F. Kéruzoré, L. Knox, M. Korman, K. Kornoelje, C. L. Kuo, A. T. Lee, K. Levy, A. E. Lowitz, C. Lu, A. Maniyar, F. Menanteau, M. Millea, J. Montgomery, Y. Moon, Y. Nakato, T. Natoli, G. I. Noble, V. Novosad, Y. Omori, S. Padin, Z. Pan, P. Paschos, K. A. Phadke, K. Prabhu, Z. Qu, W. Quan, M. Rahimi, A. Rahlin, C. L. Reichardt, C. Reuter, M. Rouble, J. E. Ruhl, E. Schiappucci, G. Smecher, J. A. Sobrin, A. A. Stark, J. Stephen, A. Suzuki, K. L. Thompson, B. Thorne, C. Trendafilova, C. Tucker, C. Umilta, J. D. Vieira, Y. Wan, G. Wang, N. Whitehorn, W. L. K. Wu, V. Yefremenko, M. R. Young, and J. A. Zebrowski. Flaring stars in a non-targeted mm-wave survey with spt-3g, 2024.

[90] D. Thornton, B. Stappers, M. Bailes, B. Barsdell, S. Bates, N. D. R. Bhat, M. Burgay, S. Burke-Spolaor, D. J. Champion, P. Coster, N. D'Amico, A. Jameson, S. Johnston, M. Keith, M. Kramer, L. Levin, S. Milia, C. Ng, A. Possenti, and W. van Straten. A Population of Fast Radio Bursts at Cosmological Distances. *Science*, 341(6141):53–56, July 2013.

[91] R. J. Thornton, P. A. R. Ade, S. Aiola, F. E. Angilè, M. Amiri, J. A. Beall, D. T. Becker, H-M. Cho, S. K. Choi, P. Corlies, K. P. Coughlin, R. Datta, M. J. Devlin,

S. R. Dicker, R. Dünner, J. W. Fowler, A. E. Fox, P. A. Gallardo, J. Gao, E. Grace, M. Halpern, M. Hasselfield, S. W. Henderson, G. C. Hilton, A. D. Hincks, S. P. Ho, J. Hubmayr, K. D. Irwin, J. Klein, B. Koopman, Dale Li, T. Louis, M. Lungu, L. Maurin, J. McMahon, C. D. Munson, S. Naess, F. Nati, L. Newburgh, J. Nibarger, M. D. Niemack, P. Niraula, M. R. Nolta, L. A. Page, C. G. Pappas, A. Schillaci, B. L. Schmitt, N. Sehgal, J. L. Sievers, S. M. Simon, S. T. Staggs, C. Tucker, M. Uehara, J. van Lanen, J. T. Ward, and E. J. Wollack. THE ATACAMA COSMOLOGY TELESCOPE: THE POLARIZATION-SENSITIVE ACTPol INSTRUMENT. *The Astrophysical Journal Supplement Series*, 227(2):21, dec 2016.

[92] T. Umemoto, M. Saito, K. Nakanishi, N. Kuno, and M. Tsuboi. Detection of a Radio Flare at Millimeter-Wavelengths from the X-ray T Tauri Star V773 Tau. In Y. Hagiwara, E. Fomalont, M. Tsuboi, and M. Yasuhiro, editors, *Approaching Micro-Arcsecond Resolution with VSOP-2: Astrophysics and Technologies*, volume 402 of *Astronomical Society of the Pacific Conference Series*, page 400, August 2009.

[93] O. Vilhu. The nature of magnetic activity in lower main sequence stars. , 133:117–126, April 1984.

[94] Osmi Vilhu and Frederick M Walter. Chromospheric-coronal activity at saturated levels. *Astrophysical Journal, Part 1 (ISSN 0004-637X), vol. 321, Oct. 15, 1987, p. 958-966. Research supported by the Fulbright Foundation.*, 321:958–966, 1987.

[95] Elizabeth O. Waagen. Nova in Reticulum: MGAB-V207 = N Ret 2020. *AAVSO Alert Notice*, 711:1, July 2020.

[96] M. Wenger, F. Ochsenbein, D. Egret, P. Dubois, F. Bonnarel, S. Borde, F. Genova, G. Jasniewicz, S. Laloë, S. Lesteven, and R. Monier. The SIMBAD astronomical database. The CDS reference database for astronomical objects. , 143:9–22, April 2000.

[97] N. Whitehorn, T. Natoli, P. A. R. Ade, J. E. Austermann, J. A. Beall, A. N. Bender, B. A. Benson, L. E. Bleem, J. E. Carlstrom, C. L. Chang, and et al. Millimeter transient point sources in the sptpol 100 square degree survey. *The Astrophysical Journal*, 830(2):143, Oct 2016.

[98] S.E. Woosley and J.S. Bloom. The supernova–gamma-ray burst connection. *Annual Review of Astronomy and Astrophysics*, 44(1):507–556, Sep 2006.

[99] E. L. Wright, G. Hinshaw, and C. L. Bennett. Producing megapixel cosmic microwave background maps from differential radiometer data. *The Astrophysical Journal*, 458(2):L53, feb 1996.

[100] Nicholas J. Wright, Jeremy J. Drake, Eric E. Mamajek, and Gregory W. Henry. The stellar-activity–rotation relationship and the evolution of stellar dynamos. *The Astrophysical Journal*, 743(1):48, nov 2011.

[101] Huiqin Yang, Jifeng Liu, Qing Gao, Xuan Fang, Jincheng Guo, Yong Zhang, Yonghui Hou, Yuefei Wang, and Zihuang Cao. The flaring activity of m dwarfs in the kepler field. *The Astrophysical Journal*, 849(1):36, 2017.

[102] Yuhan Yao, Wenbin Lu, Fiona Harrison, S. R. Kulkarni, Suvi Gezari, Muryel Guolo, S. Bradley Cenko, and Anna Y. Q. Ho. The On-axis Jetted Tidal Disruption Event AT2022cmc: X-Ray Observations and Broadband Spectral Modeling. , 965(1):39, April 2024.

[103] Qiang Yuan, Q. Daniel Wang, Wei-Hua Lei, He Gao, and Bing Zhang. Catching jetted tidal disruption events early in millimetre. *Monthly Notices of the Royal Astronomical Society*, 461(3):3375–3384, jul 2016.

[104] M. Zeilik, D. S. Hall, P. A. Feldman, and F. Walter. The Strange RS Canum Venaticorum Binary Stars. , 57:132, February 1979.

[105] Ningfeng Zhu, Tanay Bhandarkar, Gabriele Coppi, Anna M. Kofman, John L. Orlowski-Scherer, Zhilei Xu, Shunsuke Adachi, Peter Ade, Simone Aiola, Jason Austermann, and et al. The simons observatory large aperture telescope receiver. *The Astrophysical Journal Supplement Series*, 256(1):23, Sep 2021.